GUILHERME F. MURMEL LIALI

DOA ESTIMATION PERFORMANCE OF UCAS WITH REDUCED NUMBER OF SENSORS USING PHASE-MODE TRANSFORMATION AND SMALL SAMPLE SUPPORT

RIO DE JANEIRO
2022

GUILHERME F. MURMEL LIALI

DOA ESTIMATION PERFORMANCE OF UCAS WITH REDUCED NUMBER OF SENSORS USING PHASE-MODE TRANSFORMATION AND SMALL SAMPLE SUPPORT

Dissertação apresentada ao Programa de Pós-graduação em Engenharia de Defesa do Instituto Militar de Engenharia, como requisito parcial para a obtenção do título de Mestre em Ciências em Engenharia de Defesa.

Orientador(es):   José A. Apolinário Jr., D.Sc.
                  Marcello L. R. de Campos, Ph.D.

Rio de Janeiro

2022

GUILHERME F. MURMEL LIALI

DoA Estimation Performance of UCAs with Reduced Number of Sensors using Phase-Mode Transformation and Small Sample Support

Dissertação apresentada ao Programa de Pós-graduação em Engenharia de Defesa do Instituto Militar de Engenharia, como requisito parcial para a obtenção do título de Mestre em Ciências em Engenharia de Defesa.

Orientador(es): José A. Apolinário Jr. e Marcello L. R. de Campos.

Aprovada em 17 de Agosto de 2022, pela seguinte banca examinadora:

_____
Prof. **José A. Apolinário Jr.** - D.Sc., do IME - Presidente

_____
Prof. **Marcello L.R. de Campos** - Ph.D., da UFRJ

_____
Prof. **Paulo F.F. Rosa** - D.Sc., do IME

_____
Prof. **Renato P. Vio** - D.Sc., do IEAPM

Rio de Janeiro

2022

To my beloved wife. Heaven is a better place now.

ACKNOWLEDGEMENTS

"A hero is no braver than an ordinary man, but he is brave five minutes longer."

(Ralph Waldo Emerson)

ABSTRACT

Uniform Circular Arrays (UCA) are an attractive and widespread geometry of planar arrays. They are capable of 2-D DoA estimation with isotropic azimuth properties, unlike most planar arrays. In this manner, beams can be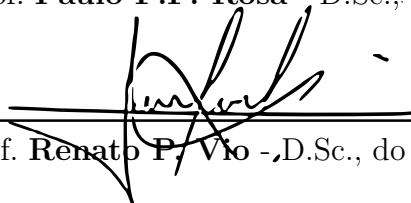 electronically rotated along the circular geometry without sensible changes in beam shape, likewise retaining the same precision in DoA estimation. In linear and planar arrays, beams become progressively wider as they rotate further of the array's boresight. Among many successful applications, are the main sonar arrays for the majority of submarines and surface vessel classes with anti-submarine capabilities worldwide.

However, applying several array processing techniques developed specifically for Uniform Linear Arrays (ULA) is impossible, due to the particular form of Array Manifold Vectors (or Steering Vectors) that UCAs possess. The Vandermonde structure of a ULA Array Manifold allows the use of techniques such as Spatial Smoothing, Forward-Backward (FB) Averaging, and, particularly, the Root-MUSIC algorithm for DoA estimation.

To circumvent this limitation, a beamspace transformation based on Phase Mode excitation, through the expansion of the model of a plane wave impinging in the UCA in an infinite series of Bessel functions of the first kind, can be employed. This expansion can be interpreted as a Discrete-Time Fourier Transform (DTFT) of the discrete-time signal of a far-field source plane hitting a continuous circular aperture. A spatially-sampled version of this DTFT can be obtained from the output signal of the M-sensor UCA. So, the sensor output vector can be interpreted as a Discrete Fourier Transform (DFT) of the spatially sampled plane wave signal. With this beamspace technique, the azimuth-dependant portion of the Array Manifold will have a Vandermonde structure, where the Root-MUSIC algorithm can be employed. This beamspace Array Manifold Vector has a Hermitian structure.

The planar geometry of the UCA results in zenithal non-isotropic behavior that affects the accuracy of azimuth and zenith estimations. This behavior translates into the tendency of the absolute zenith error to increase with increasing source zenithal angle while the absolute azimuth error decreases with increasing source zenithal angle. This behavior suggests a compromise between error metrics concerning source zenith and a practical angular region where both DoA estimations have acceptable accuracy.

Beamspace Root-MUSIC algorithm deals with the azimuth-only, Vandermonde-structured portion of the beamspace array manifold. The zenith angle for each source is considered previously estimated or the array and the sources are considered in the same plane (zenith $\theta = 90°$), and the 2-D DoA estimation is not explicitly explored. We employ a simple two-step process for 2-D DoA. First, the azimuth DoA is estimated via Root-MUSIC, assuming $\theta = 90°$. Second, we perform D 1-D Spectral MUSIC searches through the zenith angle parameter $\theta \in [0, \pi/2]$. This scheme benefits from the aspects of beamspace Root-MUSIC and associated techniques and resolves 2-D DoA with significantly reduced computational effort compared with 2-D Spectral MUSIC.

The number of phase modes (entries of the beamspace array manifold) capable of exciting a circular array with considerable intensity depends on spatial sampling. It must afford an accurate description of the receiving characteristics of the array in beamspace, otherwise resulting in biased DoA estimations.

Root-MUSIC can be paired with reduced sample support for the DoA solution as a less demanding and faster algorithm. In this case, reasonable estimates of the covariance matrix

are unattainable.

Nevertheless, several techniques can emulate the effects of the temporal averaging present in a large number of snapshots. The conditioning of the sample covariance matrix to a known ideal Toeplitz structure can mitigate the undesired effects.

LIST OF FIGURES

LIST OF ABBREVIATIONS AND ACRONYMS

A/D	Analog-to-Digital
AWGN	Additive White Gaussian Noise
BF	Beamforming
CHA	Cylindrical Hydrophone Array
DoA	Direction of Arrival
DFT	Discrete Fourier Transform
DTFT	Discrete-Time Fourier Transform
ESPRIT	Estimation of Signal Parameters by Rotational Invariance Techniques
FAS	Flank Array Sonar
IHA	Intercept Hydrophone Array
Int	Interferer signal
MFA	Medium Frequency Active
MUSIC	Multiple Signal Classification
PRS	Passive Ranging Sonar
SINR	Signal-to-Interference-plus-Noise Ratio
SIR	Signal-to-Noise Ratio
SoI	Signal of Interest
SSS	Small Sample Support
SVP	Sound Velocity Profile
TMA	Target Motion Analysis
UCA	Uniform Circular Array
ULA	Uniform Linear Array

LIST OF SYMBOLS

$\in$	In
N	Phase mode number (beamspace)
n	Phase mode index (beamspace)
M	Sensor number (element space)
m	Sensor index (element space)
γ	Angular position (continuous circular aperture)
ϕ	Azimuth angle
θ	Zenith angle
λ	Wavelength
d	Source index
D	Number ofof sources
R	Radius
K	Number of snapshots
k	Discrete-time index
J	Bessel function of the first kind
μ	Leakage minimization factor
Y	Wavenumber

CONTENTS

1 INTRODUCTION

This chapter brings the perspective of sonar operation and aspects of the underwater acoustic environment to give a background closer to the real world. We introduce the basics of sonar operations and the main topics to be considered about acoustic signals of interest and the underwater environment.

Several factors influence the design and operation of sonars in submarines, including dimensions, geometry, operating frequency of sonar arrays, acoustic environment, and the signals present in this environment that we intend to detect and estimate parameters. We also present a few details of the specific problem of array signal processing with small sample support in submarine sonar arrays.

1.1 Main Array Geometries

Sensor arrays have diversified applications that play an important role in determining a particular spatial disposition of their sensor elements (aperture, or physical dimensions of an array). Regarding the aperture, arrays can be classified as linear, planar, or volumetric TREES, 2007.

Linear arrays have elements spanning along a single dimension. The Uniform Linear Array (ULA) is the most widespread geometry and spearheaded a large portion of array signal processing. This simple geometry allows non-isotropic processing only in 1-D and presents ambiguities in these solutions resulting in an unambiguous non-isotropic coverage of only 180°.

Planar arrays span along two dimensions, extending the behavior of linear arrays. Capable of 2-D spacial filtering and DoA. A particular type of planar array with interesting isotropic properties and the scope of this work is the Uniform Circular Array (UCA). This type consists of several sensors arranged uniformly along a circle. The circular aperture has an advantage when compared with other planar arrays: a 360° isotropic coverage around the plane of the aperture SWINDLEHURST; KAILATH, 1993 (accuracy of DoA estimation and shape of beams are practically constants along the entire circular aperture).

Volumetric arrays have complex geometries and signal models but have the unique property of unambiguous solutions along the angular coverage. Of particular importance for sonar applications are the geometries that can provide isotropic unambiguous coverage: Uniform Cylindrical Arrays and Spherical Arrays. A more recent addition to the volumetric array is the conformal geometry, where sensor elements are distributed around a 3-D arbitrary surface that improves angular coverage and accuracy and reduces physical

dimensions at the cost of greater complexity due to the non-uniformity of the geometry.

1.2 Rudiments of Submarine Sonar Operation

The underwater acoustic environment can be extremely complex in terms of sound wave propagation and background noise. Such complexity is exacerbated by geographic regions of "shallow waters or brown waters". The term roughly defines the maritime environment where the propagation of signals of interest is altered by the interaction with the boundaries (surface and bottom). This interaction and, consequently, the definition of "shallow water" depends on the frequency content of the signal of interest, as well as on the Sound Velocity Profile (SVP) WAITE, 2002. In such regions, the phenomenon of propagation with multiple reflections (multipath) presents great challenges in signal processing as they result in several distinct correlated sources for the sensor array. Moreover, in such environments, the reverberation of background noise results in intensely noisy zones.

In order to relate the various factors that permeate the operation of sonar in submarines, this work divides them into the following subsections:

1.2.1 Sound propagation in the underwater environment

The Sound Velocity Profile is the primary expression of sound propagation characteristics in sonar operation. The SVP is a measure of sound propagation velocity versus depth. This can be obtained either by direct measurement (measuring time of emission and reflection in an acoustic sensor) or by indirect means, where salinity, temperature, and density are measured and serve as inputs for obtaining the speed of sound. The SVP serves as input data for sonar range prediction (also given the characteristics of the source whose detection range is to be estimated) and raytracing algorithms, where the 2-D expected vertical path of sound propagation direction underwater, contributes to situational awareness regarding the acoustic environment, identifying shadow zones (low density of sound waves), listening zones (high density of rays), and layer depths and sound ducts (depths where the gradient of the SVP change sign) MARAGE; MORI, 2013.

In Fig. 1, (a) SVP with positive gradient - Higher density of sound waves near the surface and lower density in deep water. Sound propagates in a curved upwards trajectory. (b) SVP with negative gradient - Higher density of sound waves in deep water and lower density near the surface. Sound propagates in a curved downward trajectory. (c) Layer Depth - Inverting the gradient produces a "shadow zone", with low sound wave density around the layer depth. (d) Duct - Gradient inversion allows successive refractions around the duct depth, trapping sound waves within the duct and enabling large propagation distances due to reduced propagation losses caused by refraction-only propagation.
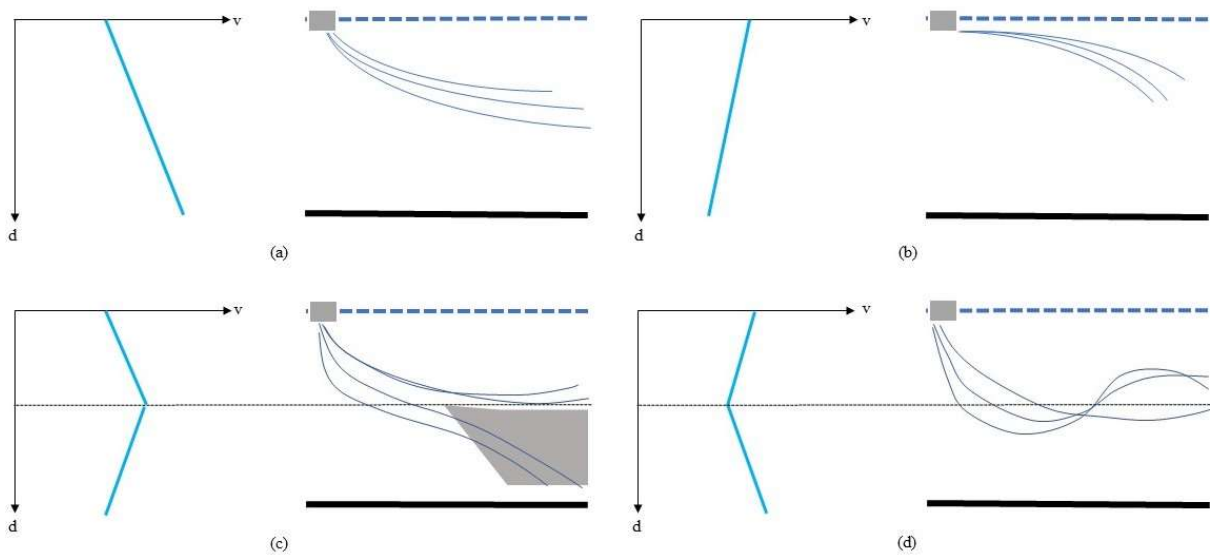
Figure 1 – SVP and respective simplified ray-trace, illustrating sound propagation scenarios of interest.

1.2.2 Aspects of Submarine Operation

Submarines have very specific demands for the operation of their sensors, notably acoustic sensors. The information provided is part of a broader process of Target Motion Analysis (TMA), with the determination of several parameters (bearing, distance, heading and speed, and, in some cases, elevation). However, the estimation of all parameters of a signal of interest (SoI), apart from very rare exceptions in the doctrine of each Navy, is carried out through totally passive means. For this reason, the operation of all sonar types is geared towards DoA estimation. This estimation serves as a basis for the TMA process to estimate all the other parameters, including refining the distances obtained by dedicated active sonar, if available. With those particularities in mind, we conclude that the accuracy of DoA estimation is of paramount importance and great complexity. The difficulties in the underwater environment are associated with frequencies, the directivity of the sources of interest, and their movement.

Detection almost exclusively by passive means is just one aspect of a precept that defines the submarine platform: its discretion. Discretion is understood as the ability to avoid or hinder the detection of the submarine by any means: acoustic, electromagnetic, infrared, and visual. This limitation greatly restricts the performance of passive sensors dependent on the conditions of sources, interference, noise, and the correct and efficient exploitation of these conditions. Furthermore, accurate measurements that exploit echolocation or bistatic and multistatic schemes are prohibitive WAITE, 2002. In these processes, complex solutions and large amounts of input data are required, in addition to accurate modeling of a sensor array and input signals to overcome challenges such as low

SINR (Signal-to-interference plus noise-ratio) situations, correlated/coherent sources, and situations with a reduced amount of signal samples (Small Sample Support).

Despite the operational limitations imposed on the use of sensors, it is possible to accurately estimate all target parameters starting with only accurate DoA estimates. Target Motion Analysis mainly processes successive DoAs through algorithms (based, for example, on Kalman filters and maximum likelihood estimation, among others) that process predicted and actual measurements. Refining these predictions to obtain acceptable solutions that will compose the tactical picture (a continuous process of refining situational awareness) or as input data for launching and guiding weapons.

1.2.3   Acoustic Signals of Interest for Submarines

Among several challenging characteristics of SoIs that complicate detection and DoA estimation, such as low SINR, correlation/coherence of several sources, and frequencies outside the operating range of the sensors, two of them should be highlighted for their intimate relationship with the scope of this work: angular position concerning the plane of the array and persistence of the source.

In practice, the SoIs for a submarine will be very close to the plane of the sensor array. This is evident by the disparity in the dimensions parallel to the plane of the arrangement (Detection and DoA estimation of an SoI several kilometers away) and perpendicular (depth of submarines is restricted to a few hundred meters). Thus, in most cases, 2-D DoA estimation will result in elevation angles very close to the horizontal plane. Adding to the fact that, operationally speaking, the elevation information, in most cases, is not as important as the azimuth, we conclude that 2-D DoA estimation will be of interest only to certain particular situations, e.g., the detection of other submarines, which occurs at short distances and with expressive vertical separation.

Another characteristic of SoIs that is reflected in a particularly important challenge is transient behavior. It is understood as transient a signal of short duration and rapid attenuation. Consequently, a small set of spatial samples (snapshots) of the transient signal will be available. This small sample support demands additional array signal processing methods, in order to eliminate noise components still present (which, with an expressive number of samples, would become negligible) or to better conditioning of input data. The fast response capability in DoA, however, is not only useful for transient sources. Tracking (successive DoAs) of mobile sources and active sonar emissions (short-lived and rapidly fading) also relies on methods with reduced sample support.
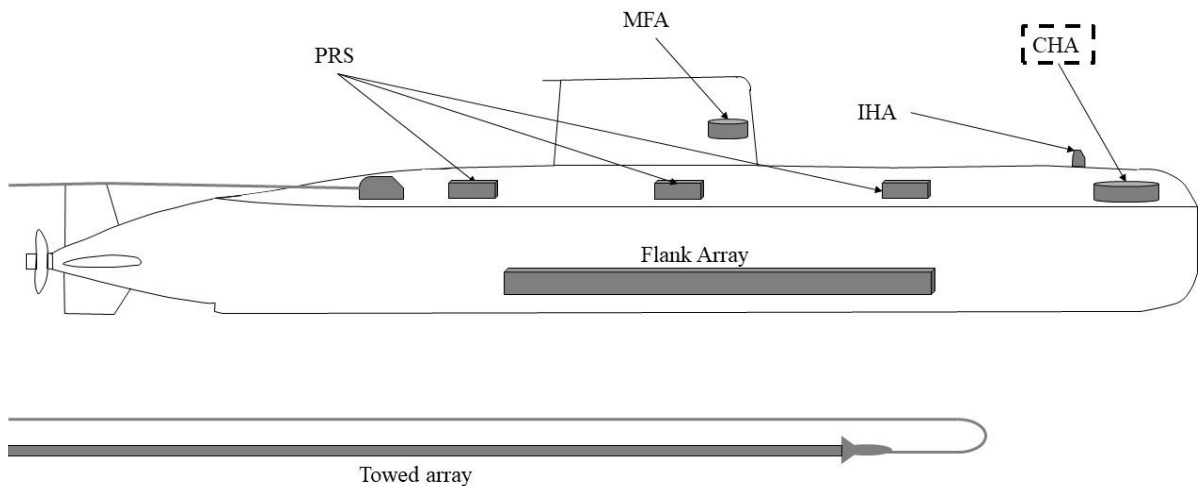
Figure 2 – Simplified set of acoustic sensor arrays (hydrophones and projectors) of a conventional submarine.

1.2.4   Submarine Sonar Arrays

A modern submarine has several sonar arrays and processing methods in order to be able to operate in different conditions: different frequency bands, angular coverage, and parameter estimation accuracy. The most common types of arrays, present on most modern submarines, are listed, but not limited to, as

- Cylindrical Hydrophone Array (CHA) - Main component of the sonar system, capable of performing panoramic surveillance (360°) and analysis in wideband (usually in the range of 1 to 12 kHz) and in narrowband. Mainly detecting cavitation noises and higher frequencies of acoustic signature. In larger nuclear submarines, optimized to operate against other submarines, the cylindrical arrangement is replaced by a volumetric array (spherical or conformal). This type of array, substantially larger and more complex, allows, among other advantages, high isotropic resolution both in azimuth and in elevation and no DoA ambiguity;

- Flank Array Sonar (FAS) - Uniform Linear Array (ULA) type sonar that allows, albeit in a limited way due to physical dimensions, to explore the low-frequency acoustic signatures, since it operates at lower frequencies (usually from 0.2 to 2.5 kHz). Small in size compared to towed arrays, it can be installed on relatively small conventional submarines;

- Passive Ranging Sonar (PRS) - Two distinct sets (one on each side) of three planar arrays, mainly used for distance estimation by passive methods, operating in the same frequency band as the CHA;

- Medium Frequency Active Sonar (MFA) - Cylindrical array used for detection and, mainly, distance estimation by active means (emission of several waveforms and detection of the return signal by the CHA) or as a somewhat downgraded backup for the CHA;

- Intercept Hydrophone Array (IHA) - Cylindrical array, used for early warning and analysis of active sonar emissions from surface ships, submarines, helicopter dipping sonars, sound buoys, and torpedoes. Operating at higher frequencies, consistent with the emissions it intends to detect, in the range of 12 to 100 kHz; and

- Towed Array - Large ULA capable of detecting very low frequencies. Thus, it is able to explore the entire range referring to the acoustic signature. It also has a large detection range. However, its operation is more delicate and limits the maneuverability of the vessel. Its use is less widespread than other types of submarine sonar.

1.3   Requirements for a Uniform Circular Array in Submarines

After brief comments on the main particularities and restrictions in the operation of sonars in submarines, it is evident that a sonar system must have several design requirements. Based on this, we can propose the following requirements regarding the estimation and presentation of DoA information:

- DoA with azimuth parameter scan - It is interesting for the operator that the signal processing of the circular array is presented along the entire angular parameter space (pseudo-spectrum of the entire discrete span of the 360° aperture). In this way, additional information of tactical nature can be extracted, in addition to greater situational awareness. Thus, it is desirable that the system has an algorithm that provides not only closed-form solutions, despite the high computational cost of angular parameter scan.

- Processing and displaying DoA estimation in 2-D in closed-form - In some particular situations, such as DoA tracking from transient or fast-moving sources, the need for fast responses, the computational cost of angular parameter scans, and, to some extent, the loss of the tactical value of this type of presentation makes it desirable that the system can also produce solutions in closed form (solution as a numerical value). It would also be desirable that, while the azimuth information is presented through a 360° scan, the elevation information, when necessary, is presented in a closed form, as an angular scan in elevation would make little sense.

- DoA with reduced sample support (transient SoIs) - Recent developments in array signal processing for sonars application focus on this particular signal characteristic.

This is because short-duration signals are the best means of detecting and tracking other submarines. Transient signals make up most of the typically reduced acoustic signatures of submarines.

- High resolution in azimuth DoA to improve target motion analysis processes - Due to the detection and estimation of all target parameters being performed (almost exclusively) passively and these estimations being heavily based on DoAs, its accuracy is clearly of paramount importance.

1.4 Motivation

Sonar operation by submarines is permeated by unique characteristics imposed by various requirements and limitations. The underwater acoustic environment is complex, exacerbated by almost exclusively passive operation of acoustic sensors. In particular, fast solutions in DoA estimation are desirable, mainly due to the presence of transient sources, which represent practically the entirety of the acoustic signature of another submarine, as well as fast-moving sources, a constant in the use of sonar in submarines. In both cases, the amount of input data from the array sensors is very small, making processing difficult, and the transitory nature of these sources urges a quick DoA solution. Circular/cylindrical arrays are the centerpieces of sonar systems on any submarine.

In line with these circumstances, this work motivated us to explore DoA estimation for transient sources in a signal and noise environment close to that encountered by a submarine in operation. To this end, we will seek to simulate signals that are based on recordings of underwater sources of interest that reflect characteristics of the acoustic environment of a submarine. From this, we use recent array signal processing techniques to improve the DoA estimation of circular/cylindrical arrays under conditions of a reduced number of samples (representing transient or fast-moving sources) and, through comparison with widely spread methods, we expect to see a performance gain under the simulated conditions.

1.5 Contributions

The main objectives of this work are the compilation of a comprehensive set of formulations for UCA beamspace transform, unifying the works of several previous authors. With phase mode-based beamspace transform as a springboard, we proceed to deal with the problem of 2-D DoA it beamspace UCA, assessing the effects of our 2-step uncoupled 2-D DoA approach, employing two distinct versions of MUSIC algorithm (beamspace Root-MUSIC for azimuth and element-space Spectral MUSIC for zenith) and the combined effects of the zenith-dependent, non-isotropic UCA beampattern.

Regarding our main topic, the limited quantity of input data, we evaluate the effects of reduced spatial and temporal data, spatial aliasing, and subspace leakage, in UCA 2-D DoA and the capabilities of mitigation techniques, Incorporated Phase Modes and Leakage Minimization, to promote improvements in estimations. Finally, we manage to obtain numerical results to evaluate these techniques both in single multivariate and joint multivariate simulations, as well as in a simulated underwater environment, with real-life signal and multipath propagation. This resulted in the article "DoA Estimation Performance of UCAs with Reduced Number of Sensors using Phase-Mode Transformation and Small Sample Support", in the twelfth IEEE Sensor Array and Multichannel Signal Processing (SAM) Workshop in Trondheim, Norway MURMEL et al., 2022.

2 BASIC CONCEPTS OF ARRAY SIGNAL PROCESSING AND DIRECTION OF ARRIVAL ESTIMATION

In this chapter, we review the fundamentals of array signal processing, beamforming and DoA estimation, and the most important classical methods. Next, focusing on DoA estimation, we address the subspace-based approaches, specifically the MUSIC algorithm and one of its polynomial rooting variations, the Root-MUSIC algorithm.

Sensor array signal processing can be understood as the processing of temporal and spatial data, based on known characteristics of the spatial arrangement of sensors KRIM; VIBERG, 1996 and statistical properties of the signal. Its first developments date back to the 1940s when it was first used in spatial filtering or beamforming. For a long time, its development focused on Uniform Linear Arrays and a number of planar geometries. Uniform Circular Arrays had limited development from the 1940s onward, without major developments in the next 20 years. However, during the 1960s, the work of several authors revolutionized the application of this type of arrangement when developing the beamspace transformation based on Phase Modes. This approach made it possible to map the UCA into a bemspace, ULA-like array manifold vector. Moreover, allowed the application of techniques that were previously exclusive to linear geometry HICKMAN; NEFF; TILLMAN, 1961.

2.1 Sensor Arrays and Signal Models

Next, we present concepts related to signal processing in arrays: the direction-finding (DoA estimation) of the input signal and the enhancement of the SoI in a specific direction (Beamforming). Although these two main applications share many concepts, including being interdependent, since the DoA estimation provides information on the direction of the signal of interest that will be enhanced or attenuated by the beamformer, they differ conceptually and in scope.

Next, we discuss the signal model received by an array of sensors. Considering that a signal of interest $s(t)$ has a central frequency f_0 and a frequency band $\triangle f$, such that the relationship $\triangle f/f_0$ is very small, we assume such a signal to be Narrowband (NB).

A real-valued signal $x(t)$ has positive and negative frequency components. A complex-valued version of the signal with only positive frequency components (analytic signal) can be obtained, where the real and imaginary parts are related by the Hilbert transform OPPENHEIM; SCHAFER, 2009.

We can represent a NB analytic signal by $x(t) = s(t)e^{j\Omega_0 t}, \Omega_0 = 2\pi f_0$ as a modulated

$s(t)$ by a carrier frequency f_0. The signal $s(t)$ contains the information being transmitted and has frequency components much lower than the center frequency f_0. A time-delayed version of a narrowband, analytic signal like $x(t - \triangle t)$ can be obtained by multiplying $x(t)$ by a complex exponential $e^{-j\Omega_0 \triangle t}$

$$x(t)e^{-j\Omega_0\triangle t} = s(t)e^{j\Omega_0 t}e^{-j\Omega_0\triangle t} = s(t)e^{j\Omega_0(t-\triangle t)} \approx x(t - \triangle t) \tag{2.1}$$

if we assume $s(t) \approx s(t - \triangle t)$, which is valid for $\triangle f / f_0$ much smaller than 1, that is, $s(t)$ does not vary too much within $\triangle t$.

Thus, multiplication by the complex exponential $e^{-j\Omega_0 \triangle t}$ corresponds to a time delay $\triangle t$ of the analytic and narrowband signal $x(t) = s(t)e^{j\Omega_0 t}$. In this way, the signals arriving from different sensors can be aligned if we know their mutual phase shifts or, equivalently, their arrival direction (the angle formed by the wavefront and the imaginary line that crosses the sensors), the speed of propagation of a far-field plane wave (assuming the source at a distance such that the wavefront arrives practically flat to the array of sensors) and the positions of the sensors.

According to this hypothesis, we can assume a relationship between the phase delays of the signal received by each sensor in the array and the 2-D azimuth and zenith DoA (ϕ_d, θ_d), respectively, of that signal with respect to some frame of reference in the array geometry TREES, 2007. After sampling and preprocessing to transform these SoIs into NB and analytical, K snapshots are obtained, which will serve as the input signal of the array, which can then be modeled for each of the D sources as follow.

$$\mathbf{x}(k) = \begin{bmatrix} x_1(k) & x_2(k) & \dots & x_M(k) \end{bmatrix}^{\mathrm{T}}, \tag{2.2}$$

where $x_m(k)$, $m \in \{1, 2 \dots, M\}$, is given by $x_m(k) = s(k)e^{j\omega_o k}e^{-j\Omega_o \Delta t_m}$, according to the analytic NB hypothesis. We can express Δt_m in terms of ϕ and θ angles of arrival. Thus, for $D = 1$ we can express $\mathbf{x}(k)$ in the form:

$$\mathbf{x}(k) = \mathbf{a}(\phi, \theta)s(k)e^{j\omega_o k} + \mathbf{n}(k), \tag{2.3}$$

where $\mathbf{n}(k)$ is the $(M \times 1)$ noise vector, modeled as uncorrelated with SoI, and $\mathbf{a}(\phi, \theta)$ is the Array Manifold Vector of a given SOI, also called Steering Vector, of dimensions $(M \times 1)$. It contains DoA information of the SoI in the successive phase delays of its inputs, in the form:

$$\mathbf{a}(\phi) = \begin{bmatrix} e^{-j\Omega_o \Delta t_1(\phi,\theta)}, & e^{-j\Omega_o \Delta t_2(\phi,\theta)}, & \dots, & e^{-j\Omega_o \Delta t_m(\phi,\theta)} \end{bmatrix}^{\mathrm{T}}, \tag{2.4}$$

where the form of $\mathbf{a}(\phi)$ depends on the geometry of the sensor array. For D sources, the signal model would be

$$\mathbf{x}(k) = \mathbf{A}(\phi)\mathbf{s}(k) + \mathbf{n}(k), \tag{2.5}$$

where $\mathbf{A}(\phi)$ is a matrix $(M \times D)$, whose columns are the array manifold vectors from each of the D sources, also called the array manifold matrix. $\mathbf{s}(k)$ is the $(D \times 1)$ signal vector, i.e., $s(k) = [s_1(k), \dots, s_D(k)]$.

2.2   Direction of Arrival and Beamforming

Successive phase shifts in the output signals from each sensor in a set of snapshots $\mathbf{x}(k)$ express the information of Direction of Arrival in the form of the array manifold vectors $\mathbf{a}(\phi_d, \theta_d)$, one for each D sources detected by the sensor array.

Beamforming (BF) is the attribution of complex-valued gains for each sensor of the array in order to enhance reception in a determined direction while attenuating in other directions KRIM; VIBERG, 1996. BF weight vector coefficients can be fixed, like the classical Bartlett or Delay-&-Sum (D&S) algorithm and its derivations, or as statistical beamformers, where statistical properties of the input signal are used DINIZ; SILVA; NETTO, 2010. Statistical BF is performed by minimizing a cost function of the spatial filter $\mathbf{w}$, subjected to the distortionless response constraint, $\mathbf{w}^\mathrm{H}\mathbf{a}(\phi, \theta) = 1$, such as the Minimum Power Distortionless Response (MPDR) or the Minimum Variance Distortionless Response (MVDR) or Capon BF.

A BF with fixed coefficients needs a certain quantity of snapshots in order to obtain a consistent sample covariance matrix. To overcome this necessity, adaptive BF arises as a solution, where recursive algorithms process each snapshot and thoroughly update the coefficients of $\mathbf{w}(k)$ in each k iteration, approaching the optimal MPDR solution based on error metrics. Additional constraints can be imposed within a Linearly Constrained Adaptive Filter (LCAF).

2.3   Classical DoA Algorithms

BF methods can be employed in DoA estimation by expressing the vector $\mathbf{w}(k)$ as a function of the candidate array manifold vector $\mathbf{a}(\phi, \theta)$ and the candidate 2-D DoA (ϕ, θ). The DoA is estimated by constructing the sample covariance matrix from a number of snapshots of the incoming signal and computing the BF spectrum for a set of discrete candidates DoAs and evaluating the angular parameters ϕ and θ for the peak values. In this way, the array gain KRISHNAVENI; KESAVAMURTHY; APARNA, 2013 in the estimated directions of interest is enhanced and unwanted signals from other sources are attenuated.

2.4   Subspace-Based Methods for DoA Estimation

Subspace-based methods are also based on a statistical model of the incoming signal. This approach serves as the basis for several array signal processing algorithms. It consists of the eigenanalysis of the covariance matrix of the input signal and, as dictated by the signal model, the decomposition into two orthogonal subspaces: signal and noise subspaces. Projecting the array manifold onto the noise subspace and selecting maximum or minimum values parameters through angular parameters search with candidate array manifolds results in the MUSIC pseudo-spectrum.

The parameter of interest (DoA) is contained in the maximum eigenvalues in the signal subspace. The solutions involve angular parameter search (MUSIC - MUltiple SIgnal Classification) SCHMIDT, 1986, polynomial rooting (Root-MUSIC) ZOLTOWSKI; KAUTZ; SILVERSTEIN, 1993 and estimations in closed form, exploring the rotational invariance between subarrays of an initial sensor array with a vector of known displacement ROY; KAILATH, 1989 (ESPRIT - Estimation of Signal Parameters by Rotational Invariance Techniques).

2.4.1   MUSIC and Root-MUSIC Algorithms

According to the 2-D signal model in Eq. (2.5) and the hypothesis of orthogonality between signal and noise, we can write the covariance matrix of the input signal $\mathbf{R}_x = \mathrm{E}[\mathbf{x}(k)\mathbf{x}^{\mathrm{H}}(k)]$ as:

$$\mathbf{R}_x = \mathbf{A}(\phi,\theta)\mathbf{R}_s\mathbf{A}(\phi,\theta)^{\mathrm{T}} + \sigma^2\mathbf{I}, \tag{2.6}$$

where $\mathbf{R}_s = \mathrm{E}[\mathbf{s}(k)\mathbf{s}^{\mathrm{H}}(k)]$ is the signal covariance matrix. By eigendecomposition of $\mathbf{R}_x$ and sorting the eigenvalues and corresponding eigenvectors, we can obtain two subspaces: the signal subspace, formed by the D eigenvectors corresponding to the most significant eigenvalues; and the noise subspace, formed by the $(M - D)$ eigenvectors referring to the noise eigenvalues of marginal magnitudes. Projecting the array manifolds into the noise subspace results in the MUSIC pseudo-spectrum.

The DoA solution of the MUSIC algorithm consists of scanning the discretized space of the angular parameters ϕ and θ, projected onto the noise subspace, looking for maximum/minimum values of the MUSIC pseudo-spectrum $P_{MUSIC}(\phi,\theta)$ SCHMIDT, 1986 .

$$P_{MUSIC}(\phi,\theta) = \frac{1}{\mathbf{a}(\phi,\theta)^{\mathrm{H}}\mathbf{E}_N\mathbf{E}_N^{\mathrm{H}}\mathbf{a}(\phi,\theta)} \tag{2.7}$$

where $\mathbf{E}_N$ is the $(M \times M - D)$ noise subspace of $\mathbf{R}_x$, corresponding to the $(M - D)$ noise eigenvectors.

Exploring the orthogonality between the subspaces contained in the signal model hypothesis, the minimum values of this projection in the signal subspace will correspond to the maximum values in the signal subspace. The values of ϕ and θ corresponding to these noise subspace minima/signal subspace maxima will correspond to the DoAs of the D sources to be resolved.

A version of this algorithm, ROOT-MUSIC BARABELL, 1983, which replaces the search for minima and maxima in a pseudo spectrum with the resolution of the roots of the polynomial of the denominator of the pseudo spectrum and the resolution of the D roots (referring to D SOIs) closest to the unit radius circle. This algorithm will be further explored in Section 3.3 .

3 ELEMENT-SPACE AND BEAMSPACE UNIFORM CIRCULAR ARRAY SIGNAL MODEL

In this chapter, we derive the Phase-Modes beamspace transformation, allowing the use of the Root-MUSIC algorithm with a UCA and the techniques for mitigating the effects of Small Sample Support and reduced quantity of sensors, to be presented in Chapter 4.

We start this derivation with an example of a DoA estimation system employing a UCA, as depicted in Fig. 3. Although we represent only six sensors in this UCA, the formulation that follows is valid for a generic case of M sensors. The diagram in Fig. 3 would be more useful to an audio system as the A/D converter is placed immediately after the sensor. In an RF DoA estimation system, the front-end would include a down-converter such that the signal would be digitized in a much lower frequency, generating, for instance, a complex bandbase digital signal. In this system, the modulated signal of
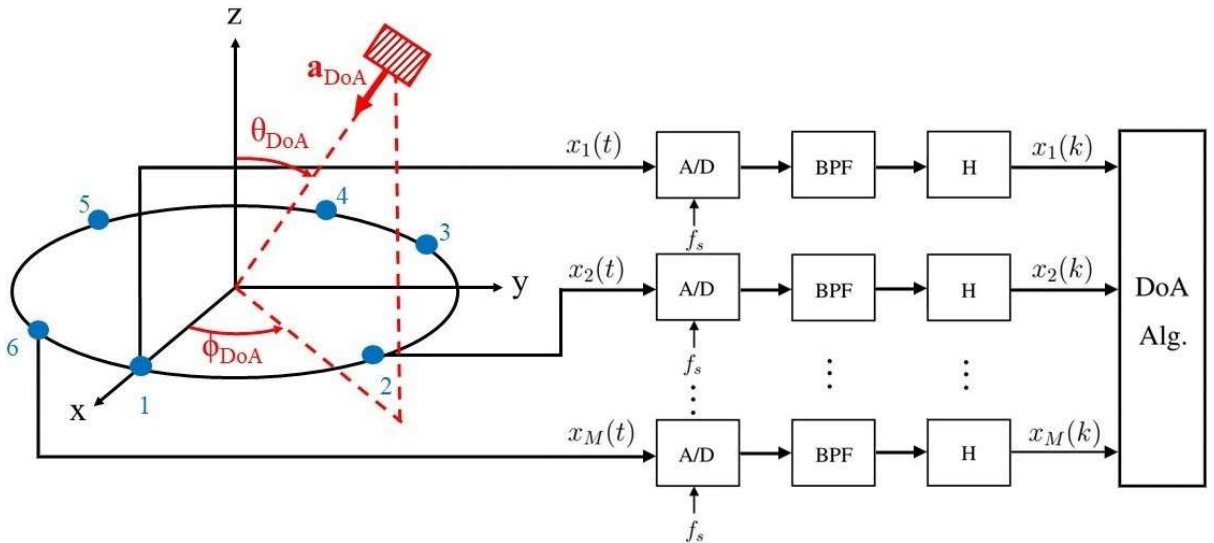
Figure 3 – An example of an acoustic DoA estimation system with a UCA. The m-th signal is processed by a bandpass filter (block PBF) and made analytical by means of Hilbert transform (block H).

each sensor, assumed narrowband (NB) with a central frequency f_o, according to Eq. (2.1), is synchronously digitized, band-pass filtered, and fed to a Hilbert Transform box (H box in the figure), resulting in an analytic NB signal.

3.1 Element-Space UCA Signal model

In this section, we start the discussion of a UCA signal model with the snapshot vector given as

$$\mathbf{x}(k) = \begin{bmatrix} x_1(k) \\ x_2(k) \\ \vdots \\ x_M(k) \end{bmatrix}. \tag{3.1}$$

The signal from the m-th sensor $x_m(t)$, assuming we have only one incoming signal, the Signal of Interest (SoI), hitting the array from azimuth $\phi_{\mathrm{DoA}} = \phi_1$ and zenith $\theta_{\mathrm{DoA}} = \theta_1$, as in Fig. 3, after the A/D converter, could be represented by

$$x_m(k) = s(k)e^{j\omega_o k}e^{-j\Omega_o \Delta t_m}, \tag{3.2}$$

where $\Omega_o = 2\pi f_o$, $\omega_o = \frac{\Omega_o}{f_s}$, f_s being the sampling frequency, and Δt_m corresponds to the delay (regarding a given reference, such as the position of a sensor) observed in the m-th sensor. We have also assumed that the maximum frequency of the signal being modulated, $s(t)$, is much lower than the operating frequency f_o. From Fig. 3, we can represent the unit vector in the propagation direction of the wavefront as $\mathbf{a}_1 = -\left[\sin(\theta_1)\cos(\phi_1) \quad \sin(\theta_1)\sin(\phi_1) \quad \cos(\theta_1)\right]^{\mathrm{T}}$, such that, considering the position vector for each m-th sensor as

$$\mathbf{p}_m = R\left[\cos((m-1)\frac{2\pi}{M}) \quad \sin((m-1)\frac{2\pi}{M}) \quad 0\right]^{\mathrm{T}}, \tag{3.3}$$

with $m \in [1, 2, \cdots, M]$, we can write, taking the center of the UCA as the reference, the delay Δt_m as TREES, 2007

$$\Delta t_m = \frac{\mathbf{p}_m^{\mathrm{T}}\mathbf{a}_1}{c}, \tag{3.4}$$

c being the propagation speed of the wavefront. From Eqs. (3.2) and (3.4), we can write

$$x_m(k) = s(k)e^{j\omega_o k}e^{j\frac{2\pi R}{\lambda}\sin(\theta_1)\left[\cos(\phi_1)\cos(\frac{2\pi(m-1)}{M})+\sin(\phi_1)\sin(\frac{2\pi(m-1)}{M})\right]}, \tag{3.5}$$

which, after some straightforward geometric manipulation, yields the expression for each entry of the UCA array manifold vector as

$$x_m(k) = s(k)e^{j\omega_o k}e^{j\frac{2\pi R}{\lambda}\sin(\theta_1)\cos(\phi_1-\frac{2\pi(m-1)}{M})}. \tag{3.6}$$

Therefore, considering the simple case of a single wavefront hitting the elements of

the UCA and no background noise, the snapshot in Eq. (3.1) could be written as

$$
\mathbf{x}(k) = s(k)e^{j\omega_o k} \underbrace{\begin{bmatrix} e^{j\frac{2\pi R}{\lambda}\sin(\theta_1)\cos(\phi_1)} \\ e^{j\frac{2\pi R}{\lambda}\sin(\theta_1)\cos(\phi_1-\frac{2\pi}{M})} \\ \vdots \\ e^{j\frac{2\pi R}{\lambda}\sin(\theta_1)\cos(\phi_1-\frac{2\pi(M-1)}{M})} \end{bmatrix}}_{\mathbf{a}(\phi_1,\theta_1)}, \tag{3.7}
$$

where $\mathbf{a}(\phi_1, \theta_1)$ is the UCA 2-D array manifold vector. Now considering D emitters and uncorrelated background noise, we may express the snapshot as follows

$$
\mathbf{x}(k) = \mathbf{A}\mathbf{s}(k) + \mathbf{n}(k), \tag{3.8}
$$

where $\mathbf{A} = \begin{bmatrix} \mathbf{a}(\phi_1, \theta_1) & \cdots & \mathbf{a}(\phi_D, \theta_D) \end{bmatrix}$ is the $M \times D$ *array manifold matrix* with columns being D *array manifold vectors*, $\mathbf{s}(k)$ is the $D \times 1$ signal vector in the center of the array, given as (assuming, for simplicity, synchronized carriers)

$$
\mathbf{s}(k) = e^{j\omega_o k} \begin{bmatrix} s_1(k) \\ \vdots \\ s_D(k) \end{bmatrix}, \tag{3.9}
$$

and $\mathbf{n}(k) = \begin{bmatrix} n_1(k) & \cdots & n_M(k) \end{bmatrix}^{\mathrm{T}}$ is the $M \times 1$ uncorrelated background noise vector, with noise samples from each sensor. The d-th array manifold vectors are expressed as

$$
\mathbf{a}(\phi_d, \theta_d) = \begin{bmatrix} e^{j\frac{2\pi R}{\lambda}\sin(\theta_d)\cos(\phi_d)} \\ e^{j\frac{2\pi R}{\lambda}\sin(\theta_d)\cos(\phi_d-\frac{2\pi}{M})} \\ \vdots \\ e^{j\frac{2\pi R}{\lambda}\sin(\theta_d)\cos(\phi_1-\frac{2\pi(M-1)}{M})} \end{bmatrix}. \tag{3.10}
$$

With the previous model, it is easy to obtain the element-space covariance matrix $\mathbf{R}_x = \mathrm{E}[\mathbf{x}(k)\mathbf{x}^{\mathrm{H}}(k)]$ as

$$
\mathbf{R}_x = \mathbf{A}\mathbf{R}_s\mathbf{A}^{\mathrm{H}} + \sigma^2\mathbf{I}_M, \tag{3.11}
$$

where $\mathbf{R}_s = \mathrm{E}[\mathbf{s}(k)\mathbf{s}^{\mathrm{H}}(k)]$ is the covariance matrix of the signal input in the center of the array and $\mathbf{R}_n = \mathrm{E}[\mathbf{n}(k)\mathbf{n}^{\mathrm{H}}(k)] = \sigma^2\mathbf{I}_M$ is the covariance matrix of the presumed additive white Gaussian (AWG) noise process.

3.2   Phase Modes-based Beamspace UCA Signal Model

In this section, we follow the beamspace transformation proposed in HICKMAN; NEFF; TILLMAN, 1961; LONGSTAFF; CHOW; DAVIES, 1967 to change the structure of the UCA manifold using the concept of phase mode excitation.

The objective of such transformation is to map the element space array manifold into an alternative beamspace form. The beamspace signal model should have a different expression, more suitable for a particular objective while retaining precision in describing the receiving characteristics of the array. Simplification in the signal model expression in beamspace and dimensional reduction in beamspace mapping are both also desirable. Finally, the objective of the transformation is to alter the signal model to a suitable form to employ the Root-MUSIC algorithm for azimuth DoA estimation without a grid search. This suitable form is the center-Hermitian Vandermonde structure such as

$$\mathbf{a}(\phi) = [e^{-iv(\phi)}, e^{(-i+1)v(\phi)}, \dots, 1, \dots e^{(i-1)v(\phi)}, e^{iv(\phi)}]^{\mathrm{T}}, \tag{3.12}$$

with $i \in \mathbb{N}$.

The beamspace technique employs Fourier analysis of the excitation function of an array (excitation function, in the case of an exclusively passive array, being the output signal of each sensor excited by the impinging wavefront). The decomposition of the discrete excitation function in a finite number of harmonics via Discrete Fourier Transform (DFT) allows the transformation of the $M \times 1$ element-space array manifold $\mathbf{a}(\phi_d, \theta_d)$ into a $(2N + 1) \times 1$ beamspace array manifold with an advantageous Vandermonde structure for the azimuth parameter.

As shown in the previous section, the steering vector corresponding to a wavefront hitting the UCA with azimuth ϕ, considering a given zenith angle θ, may be expressed as

$$\mathbf{a}(\phi) = \begin{bmatrix} e^{\mathrm{j}Y\bar{R}\cos(\phi)} \\ e^{\mathrm{j}Y\bar{R}\cos(\phi - \frac{2\pi}{M})} \\ \vdots \\ e^{\mathrm{j}Y\bar{R}\cos(\phi - \frac{2\pi(M-1)}{M})} \end{bmatrix}, \tag{3.13}$$

with $Y = 2\pi/\lambda$ being the wavenumber and $\bar{R} = R\sin\theta$. The previous expression is not convenient for determining the incoming azimuth using, for instance, with the ROOT-MUSIC algorithm. To overcome this limitation and avoid a two-dimension grid search SCHMIDT, 1986; ZOLTOWSKI; KAUTZ; SILVERSTEIN, 1993; AKIYAMA; YAMAOKA; HAMADA, 1999, phase mode excitation theory-based beamspace transform can be employed. The beamspace transform is based on the spectral analysis of the output signal of each sensor of the array. We start the formulation by presenting the mathematical basis of this method, the Jacobi-Anger expansion ABRAMOWITZ; STEGUN, 1964. This expansion is the Fourier series representation of a complex exponential in the form

$$\mathrm{e}^{u\cos(\phi)} = \sum_{n=-\infty}^{\infty} \mathrm{j}^n J_n(u)\mathrm{e}^{\mathrm{j}n\phi}, \tag{3.14}$$

where $J_n(\bullet)$ being the Bessel function of the first kind and order n. Eq. (3.14) already suggests a manner to transform the array manifold into a Vandermonde structure, as

required for applying the Root-MUSIC algorithm. Before dealing directly with a sampled circular aperture (a UCA), we first consider a continuous circular aperture (akin to a UCA with an infinite number of sensors), with γ being the angular position of sensors $\in [0, 2\pi]$. Any output signal will be periodic with period 2π MATHEWS; ZOLTOWSKI, 1994 and can be expanded by a Fourier series

$$s_\gamma(k) = \sum_{n=-\infty}^{\infty} c_n \mathrm{e}^{\mathrm{j}n\gamma} \mathrm{e}^{\mathrm{j}\left[Y\bar{R}\cos(\phi-\gamma)\right]}. \tag{3.15}$$

A phase mode is then defined as $w_n(\gamma) = c_n \mathrm{e}^{\mathrm{j}n\gamma} \mathrm{e}^{\mathrm{j}\left[Y\bar{R}\cos(\phi-\gamma)\right]}$. The output signal $s_n(k)$ referring to the excitation of the continuous aperture by the n-th phase-mode $w_n(\gamma)$ is given by

$$s_n(k) = \frac{1}{2\pi} \int_0^{2\pi} w_n(\gamma)\, \mathrm{e}^{\mathrm{j}\left[Y\bar{R}\cos(\phi-\gamma)\right]} d\gamma. \tag{3.16}$$

By applying the Anger equation and the equivalence with Bessel functions of the first kind ABRAMOWITZ; STEGUN, 1964, we conclude that

$$s_n(k) = \mathrm{j}^n J_n\left(Y\bar{R}\right) \mathrm{e}^{\mathrm{j}n\phi}. \tag{3.17}$$

Now, we consider the sample circular aperture of a UCA with M sensors. Applying the Jacobi-Anger expansion to the output signal of the m-th sensor and inspecting Eq. (3.6), we finally have an expression for each sensor output as

$$\bar{x}_m(k) = s(k) \sum_{n=-\infty}^{\infty} \mathrm{j}^n J_n\left(Y\bar{R}\right) \mathrm{e}^{\mathrm{j}n\phi} \mathrm{e}^{-\mathrm{j}\left(\frac{2\pi n(m-1)}{M}\right)}. \tag{3.18}$$

Eq. (3.18) already suggests that the output signal of the sampled circular aperture is very similar to a DTFT of the output signal of a continuous circular aperture in Eq. (3.17)

In the beamspace transform, we extend the spectral analysis to the sampled aperture via DFT, aiming at the centre-Hermitian structure. Taking the N-point DFT of the signal model of Eq. (3.6), the output signal of each sensor can be written as

$$\bar{x}_n(k) = s(k)\frac{1}{\sqrt{M}} \sum_{m=0}^{M-1} c_n \mathrm{e}^{\mathrm{j}\frac{2\pi nm}{M}}. \tag{3.19}$$

Now, applying the Jacobi-Anger expansion in Eq. (3.19) yields the n-th phase mode as

$$\bar{x}_n(k) = s(k)\frac{1}{\sqrt{M}} \sum_{q=-\infty}^{\infty} \sum_{m=0}^{M-1} \mathrm{j}^q J_q\left(Y\bar{R}\right) \mathrm{e}^{\left(\mathrm{j}q\phi\right)} \mathrm{e}^{\left(\frac{-\mathrm{j}2\pi qm}{M}\right)} \mathrm{e}^{\left(\frac{\mathrm{j}2\pi nm}{M}\right)}. \tag{3.20}$$

In the following formulations, we apply several simplifications to Eq. (3.20). The first of them is through analyzing the inner summation WAX; SHEINVALD, 1994

$$\sum_{m=0}^{M-1} e^{-j2\pi qm/M} e^{j2\pi nm/M} = \begin{cases} M, & \text{if } q=n+lM, \, l \text{ being an integer,} \\ 0, & \text{otherwise.} \end{cases} \quad (3.21)$$

Substituting Eq. (3.21) in Eq. (3.20), we can simplify the inner summation and retain only the outer summation in the form of a Fourier series and Jacobi-Anger expansion as Eq. (3.18)

$$
\begin{aligned}
\bar{x}_n(k) =& s(k)\sqrt{M} \sum_{l=-\infty}^{\infty} j^{n \pm lM} J_{n \pm lM}\left(Y\bar{R}\right) e^{(j(n \pm lM)\phi)} \\
=& s(k)\sqrt{M} \left[j^n J_n\left(Y\bar{R}\right) e^{(jn\phi)} \right. \\
& \sum_{l=1}^{\infty} \left(j^{n+lM} J_{n+lM}\left(Y\bar{R}\right) e^{(j(n+lM)\phi)} \right. \\
& \left. \left. + j^{n-lM} J_{n-lM}\left(Y\bar{R}\right) e^{(j(n-lM)\phi)} \right) \right].
\end{aligned}
\quad (3.22)
$$

The complex coefficients of the Fourier series of Eq. (3.18) are given by the Bessel functions of the first kind. Due to the behavior of these functions in relation to their arguments, we show that only a limited number of harmonics (phase modes) with significant amplitudes can be excited by the circular aperture of the UCA HONG; TEWFIK, 1991; GOOSSENS; ROGIER; WERBROUCK, 2008. Note that the zenithal angle $\theta \in [0, \pi/2]$, and that the arguments of the Bessel functions $\in [0, 2\pi R/\lambda]$. The Bessel functions where the order exceeds their argument yield small amplitudes and, in this manner, we conclude that the highest order phase-mode N with significant amplitude will be the largest integer smaller than the maximum argument $2\pi R/\lambda$.

As shown in Fig. 4, when the order of the function exceeds the argument, the amplitude is small for that argument. In this example, with $R = \lambda$, $Y\bar{R} = 2\pi$, is the maximum argument, when $\sin\theta = 1$ (SoI and UCA in the same plane). Therefore, regarding this example, the highest order phase mode excitation by the UCA will be $N = 6$.

Further simplifications can be made by taking advantage of the behavior of the Bessel functions of the first kind depicted in Fig. 4. Making the number of sensor M much larger than $YR = 2\pi R/\lambda$ (the maximum argument for the Bessel functions) in Eq. (3.22), every phase mode in the form $\sqrt{M} j^{q \pm lM} J_{q \pm lM}\left(Y\bar{R}\right) e^{(j(q \pm lM)\phi)}$, for $l \geq 2$, has negligible amplitudes and can be omitted. In this manner, only the modes with $l = 0$ e $l = 1$ are significant.

$$
\begin{aligned}
\bar{x}_n(k) =& s(k)\sqrt{M} \left[j^n J_n\left(Y\bar{R}\right) e^{(jn\phi)} \right. \\
& + j^{n+M} J_{n+M}\left(Y\bar{R}\right) e^{(j(n+M)\phi)} \\
& \left. + j^{n-M} J_{n-M}\left(Y\bar{R}\right) e^{(j(n-M)\phi)} \right]
\end{aligned}
\quad (3.23)
$$

Here, we make two assumptions: if we assume that the number of sensor M is much larger than the number of phase modes n, the second portion of Eq. (3.23),
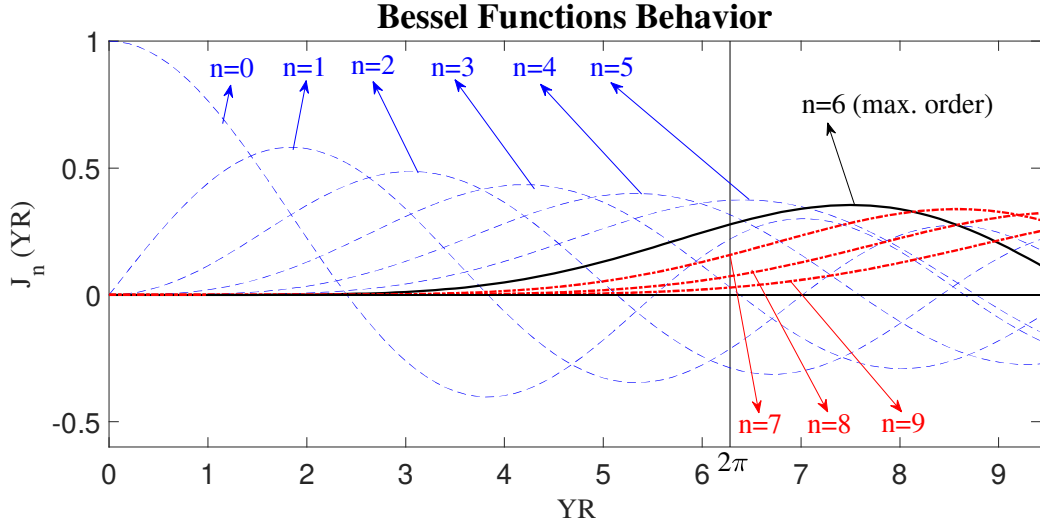
Figure 4 – Behavior of the Bessel functions and dependence on the zenith parameter θ. The blue dashed curves are Bessel functions os the first kind of order 0 to 5, which the order n is smaller than the maximum argument 2π. The black curve is the Bessel function of highest order less than the maximum argument. The red dotted curves are Bessel functions which the order n is larger than the maximum argument.

$j^{n\pm M} J_{n\pm M}\left(Y\bar{R}\right) e^{(j(n\pm M)\phi)} \approx 0$, and, consequently, $\bar{x}_n(k) \approx s(k)\sqrt{M}[j^n J_n(Y\bar{R})e^{(jn\phi)}]$. On the other hand, if we assume that the number of phase modes n is large enough, $j^n J_n(Y\bar{R})e^{(jn\phi)} \approx 0$ and $\bar{x}_n(k) \approx s(k)\sqrt{M}[j^{n\pm M} J_{n\pm M}(Y\bar{R})e^{(j(n\pm M)\phi)}]$ HONG; TEWFIK, 1991; GOOSSENS; ROGIER; WERBROUCK, 2008. Finally, we have a good approximation for the expression of each entry $\bar{x}_n(k)$ of the output signal vector in beamspace $\bar{\mathbf{x}}(k)$ as a complex amplitude multiplying a single Bessel function of the first kind and a complex exponential.

$$\bar{x}_n(k) = s(k)\sqrt{M}j^n J_n\left(Y\bar{R}\right) e^{jn\phi}, -\left\lfloor \frac{M-1}{2} \right\rfloor \leq n \leq \left\lfloor \frac{M-1}{2} \right\rfloor, \qquad (3.24)$$

where $\lfloor (M-1)/2 \rfloor$ denotes the largest integer smaller or equal to $(M-1)/2$.

With $n \in [-N, \ldots, -1, 0, 1, \ldots, N]$, Eq. (3.24) not only defines the form of the entries of vector $\bar{\mathbf{x}}(k)$ but its dimension by defining the number n of phase modes involved in the beamspace transformation, where $N = \lfloor (M-1)/2 \rfloor$. Through this formulation, we manage to transform the $M \times 1$ element space output signal vector $\mathbf{x}(k)$ into the $(2N+1 \times 1)$ beamspace counterpart $\bar{\mathbf{x}}(k)$, with $2N+1 \leq M$.

Determining the number of phase modes, however, deserves further consideration. From the very formulation and simplifications of the phase modes-based beamformer, we have two different criteria. Based on the approach of HONG; TEWFIK, 1991, aiming for no dimensional reduction (odd number M of sensors) or one-dimensional reduction (M even) in the dimensions of the beamspace array manifold in comparison with the
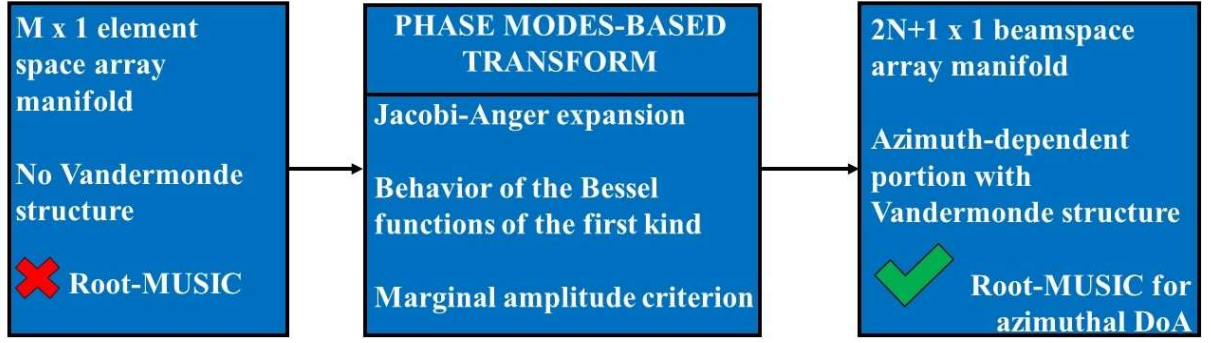
Figure 5 – Phase modes-based beamspace transform diagram.

element-space one, the criterion is $\lfloor (M-1)/2 \rfloor$ (for M odd, $2N+1 = M$ and for M even, $2N+1 = M-1$). On the other hand, the behavior of Bessel functions of the first kind and the consequent simplification of Eq. (3.23) states that $M >> 2\pi R/\lambda$. A satisfactory merging of these two criteria can be N being the minimum between $\lfloor (M-1)/2 \rfloor$ and $2\pi R/\lambda$ HICKMAN; NEFF; TILLMAN, 1961.

A closer look in Eq. (3.22) eludes an additional marginal amplitude criterion. Each phase mode $x_n(k)$ is theoretically expressed by an infinite summation of Bessel functions. The choice of n, the number of phase modes, that maps the array in beamspace should be such that each $\bar{x}_n(k)$ is defined by a single term $\mathrm{j}^n J_n \left(Y\bar{R} \right) \mathrm{e}^{(\mathrm{j}n\phi)}$; and all additional terms $\mathrm{j}^{n+lM} J_{n+lM} \left(Y\bar{R} \right) \mathrm{e}^{(\mathrm{j}(n+lM)\phi)}$ should have negligible amplitude contributions WAX; SHEINVALD, 1994. In other words, n should be such that the dominant term in Eq. (3.22) corresponds to $l = 0$. By taking the immediate additional terms (making $l = \pm 1$), a suitable encompassing criterion will be

$$\frac{2\pi R}{\lambda} < n \leq \left\lfloor \frac{(M-1)}{2} \right\rfloor, \frac{|J_{n\pm M}(Y\bar{R})|}{|J_n(Y\bar{R})|} < \epsilon, \tag{3.25}$$

for an arbitrary ϵ.

The implementation of such transformation is represented in Algorithm 1. The beamspace transformation matrix $\mathbf{W}$, which may be expressed as an $M \times (2N+1)$ spatial DFT sub-matrix, where each column represents the n-th excitation mode vector $\mathbf{w}_n$, is defined as

$$\mathbf{w}_n = \frac{1}{\sqrt{M}} \begin{bmatrix} 1 & \mathrm{e}^{-\mathrm{j}2\pi \frac{n}{M}} & \cdots & \mathrm{e}^{-\mathrm{j}2\pi \frac{n(M-1)}{M}} \end{bmatrix}^{\mathrm{T}}. \tag{3.26}$$

The inner product of $\mathbf{w}_n$ and the array manifold vector $\mathbf{a}(\phi)$ is written as

$$\mathbf{w}_n^{\mathrm{H}} \mathbf{a}(\phi) = \frac{1}{\sqrt{M}} \sum_{m=0}^{M-1} \mathrm{e}^{\mathrm{j}2\pi \frac{mn}{M}} \mathrm{e}^{\mathrm{j}Y\bar{R}\cos(\phi - \frac{2\pi m}{M})}. \tag{3.27}$$

Employing the Jacobi-Anger expansion in Eq. (3.27), it then can be approximated as

$$\mathbf{w}_n^H \mathbf{a}(\phi) \approx \sqrt{M} \mathrm{j}^n J_n\left(Y\bar{R}\right) \mathrm{e}^{\mathrm{j}n\phi}, \tag{3.28}$$

with n from $-N$ to N, N being the minimum between $\lfloor (M-1)/2 \rfloor$ and $2\pi R/\lambda$. Given N, we form the $M \times (2N+1)$ matrix $\mathbf{W}$ given as

$$\mathbf{W} = \begin{bmatrix} \mathbf{w}_{-N} & \cdots & \mathbf{w}_{-1} & \mathbf{w}_0 & \mathbf{w}_1 & \mathbf{w}_N \end{bmatrix}. \tag{3.29}$$

A good approximation in Eq.(3.28) would result in

$$\bar{\mathbf{a}}(\phi) = \mathbf{W}^H \mathbf{a}(\phi) \approx \mathbf{J}\mathbf{v}(\mathrm{e}^{\mathrm{j}\phi}) = \sqrt{M} \begin{bmatrix} \mathrm{j}^{-N} J_{-N}(Y\bar{R}) e^{-\mathrm{j}N\phi} \\ \vdots \\ \mathrm{j}^{-1} J_{-1}(Y\bar{R}) e^{-\mathrm{j}\phi} \\ J_0(K\bar{R}) \\ \mathrm{j}^1 J_1(Y\bar{R}) e^{\mathrm{j}\phi} \\ \vdots \\ \mathrm{j}^N J_N(Y\bar{R}) e^{\mathrm{j}N\phi} \end{bmatrix}, \tag{3.30}$$

where $\mathbf{J}$ is a diagonal matrix whose elements are $\sqrt{M}\mathrm{j}^n J_n(K\bar{R})$, n varying from $-N$ to N, and vector $\mathbf{v}(\phi)$ correspons to

$$\mathbf{v} = \begin{bmatrix} z^{-N} \\ \vdots \\ z^{-1} \\ 1 \\ z \\ \vdots \\ z^N \end{bmatrix}, \tag{3.31}$$

with $z = \mathrm{e}^{\mathrm{j}\phi}$.

With the beamspace transformation of Eq. (3.27) and the approximations of Eq. (3.28), we can write the signal model of the $(2N+1) \times 1$ beamspace array manifold as

$$\bar{\mathbf{x}}(k) = \mathbf{W}^H \mathbf{x}(k) = \mathbf{W}^H \mathbf{A}(\phi)\mathbf{s}(k) + \mathbf{W}^H \mathbf{n}(k) = \bar{\mathbf{A}}(\phi)\mathbf{s}(k) + \bar{\mathbf{n}}(k), \tag{3.32}$$

where $\bar{\mathbf{A}}(\phi)$ is the beamspace array manifold for the azimuth parameter and $\bar{\mathbf{n}}(k)$ is the beamspace noise vector, addressed in Appendix B.

Recalling Eq. (3.11), the expression for the beamspace covariance matrix $\mathbf{R}_{\bar{x}} = \mathrm{E}[\bar{\mathbf{x}}(k)\bar{\mathbf{x}}^H(k)]$ becomes

$$\mathbf{R}_{\bar{x}} = \mathbf{W}^H \mathbf{R}_x \mathbf{W} = \mathbf{W}^H \mathbf{A}(\phi)\mathbf{R}_s \mathbf{A}^H(\phi)\mathbf{W} + \mathbf{R}_{\bar{n}}, \tag{3.33}$$

where $\mathbf{R}_{\bar{n}} = \mathrm{E}[\bar{\mathbf{n}}(k)\bar{\mathbf{n}}^H(k)] = \mathbf{W}^H \mathbf{R}_n \mathbf{W}$ is the beamspace noise covariance matrix.

3.3 ROOT-MUSIC Solution

Recalling the element-space spectrum of the MUSIC algorithm, the directions of arrival of D sources are obtained by choosing the D maximum peaks:

$$P(\phi) = \frac{1}{\mathbf{a}^{\mathrm{H}}(\phi)\mathbf{E}_{\mathrm{N}}\mathbf{E}_{\mathrm{N}}^{\mathrm{H}}\mathbf{a}(\phi)}, \tag{3.34}$$

where $\mathbf{E}_N$ corresponds to the noise eigenvectors of the element-space covariance matrix $\mathbf{R}_x$, according to Algorithm 2. When using the beamspace transformation matrix $\mathbf{W}$ of Eq. (3.29) and recalling Eq. (3.32) and (3.33), we have the beamspace MUSIC spectrum, given as

$$\bar{P}(\phi) = \frac{1}{\bar{\mathbf{a}}^{\mathrm{H}}(\phi)\bar{\mathbf{E}}_{\mathrm{N}}\bar{\mathbf{E}}_{\mathrm{N}}^{\mathrm{H}}\bar{\mathbf{a}}(\phi)}, \tag{3.35}$$

where $\bar{\mathbf{a}}(\phi) = \mathbf{W}^{\mathrm{H}}\mathbf{a}(\phi)$ is given in Eq. (3.30) and $\bar{\mathbf{E}}_{\mathrm{N}}$ is the $(2N+1) \times (2N+1-D)$ matrix containing the $2N+1-D$ vectors that span the beamspace noise subspace of $\mathbf{R}_{\bar{x}}$. The denominator of $\bar{P}(\phi)$ can then be represented as a polynomial $f(z)$ evaluated in $z = \mathrm{e}^{\mathrm{j}\phi}$:

$$\begin{aligned}
f(z) &= \mathbf{v}^{\mathrm{H}}(z)\underbrace{\mathbf{J}\bar{\mathbf{E}}_{\mathrm{N}}\bar{\mathbf{E}}_{\mathrm{N}}^{\mathrm{H}}\mathbf{J}}_{\mathbf{B}}\mathbf{v}(z) \\
&= \mathbf{v}^{\mathrm{H}}(z)\mathbf{B}\mathbf{v}(z).
\end{aligned} \tag{3.36}$$

If we are searching for (D) peaks in $\bar{P}(\phi)$, we can search for (D) zeros of $f(z)$ positioned closest to the unit circle. This is possible due to the elements of matrix B being numbers (the variable is z). We note that, when $z = \mathrm{e}^{\mathrm{j}\phi}$, then $z^{\mathrm{H}} = 1/\mathrm{e}^{\mathrm{j}\phi}$ such that we find all zeros of

$$f(z) = \mathbf{v}^{\mathrm{T}}(1/z)\mathbf{B}\mathbf{v}(z), \tag{3.37}$$

and select those D closest to and inside the unit circle to obtain the estimated DoA, as in Algorithm 3. The coefficients of $f(z)$ BABU, 1991 can be calculated with

$$f(z) = \sum_{k=-N+1}^{N-1} c_k z^k, \tag{3.38}$$

where c_k is the summation of the entries of the k-th diagonal of the matrix $\mathbf{B}$ and $k = 0$ corresponds to the main diagonal, $k > 0$ corresponds to diagonals above the main, and $k < 0$ corresponds to the ones below. Since B is symmetric about the main diagonal, it is possible to calculate the coefficient just for $k \geq 0$ or $k \leq 0$ and rearrange them to obtain the other coefficients. Let z_d be one of these zeros; knowing that $z_d = \mathrm{e}^{\mathrm{j}\phi_d}$ when z_d belongs to the unit circle or $|z_d|\mathrm{e}^{\mathrm{j}\phi_d}$ when close to the unit circle, we obtain

$$\phi_d = \mathrm{angle}(z_d). \tag{3.39}$$

In order to depict the comparison between element space and beamspace array manifold vector and the accuracy of the phase modes transform, in Fig. 6-9 we have the 2-D

MUSIC pseudo-spectrum in element space and beamspace, for a 16 sensor UCA (11 phase modes) × zenith for two stochastic uncorrelated narrowband sources: SoI ($\phi_{SoI} = 37.9°$ and $\theta_{SoI} \in \{10°, 90°\}$) and interferer ($\phi_{Int} = 120.5°$ and $\theta_{Int} = 50.7°$) with central frequencies of 6 kHz and 7 kHz. Sample support of 1,000 and with 10 snapshots, $R = \lambda$, SIR of 3 dB, and AWGN with SNR of 10 dB.

Element-Space Spectral MUSIC DoA
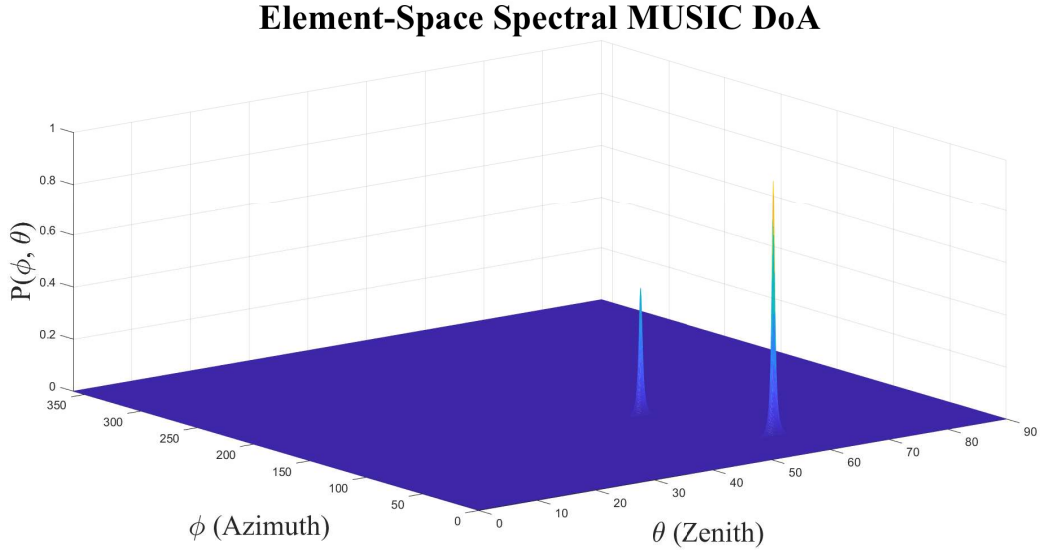
Figure 6 – Element space MUSIC pseudo-spectrum. 16 sensor UCA resolving two narrow-band sources with angular positions: $\phi_{SoI} = 37.9°$, $\theta_{SoI} = 57.7°$, $\phi_{Int} = 120.5°$ and $\theta_{Int} = 50.7°$. SIR of 3 dB, immerse in isotropic AWGN with SNR of 10 dB. Sample support of **1,000 snapshots**.

The pseudo-spectra in element space and beamspace provide very close 2-D DoA solutions, depicting the accuracy of the beamspace transform for large and small sample support.

Beamspace Spectral MUSIC DoA
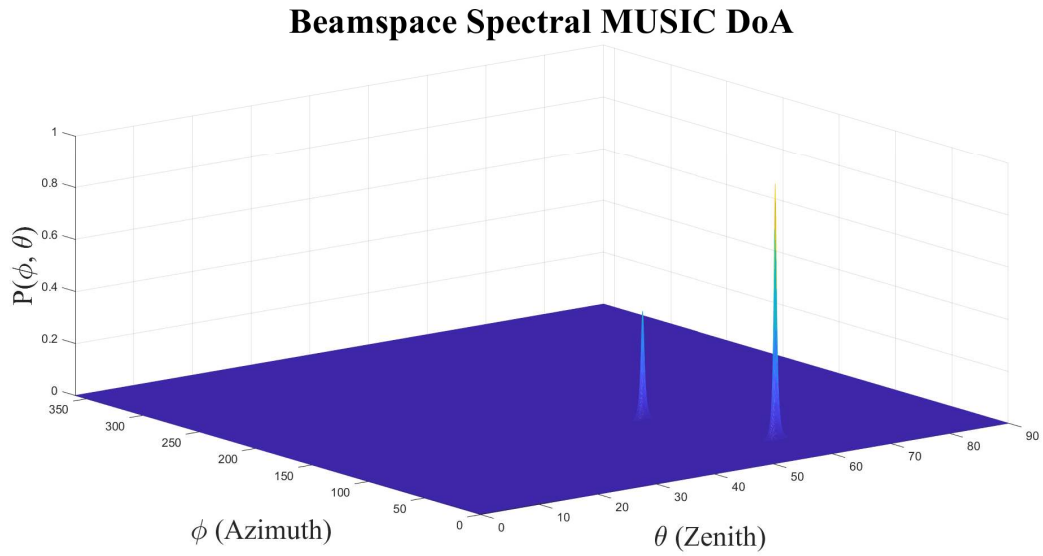
Figure 7 – Beamspace MUSIC pseudo-spectrum. 16 sensor UCA mapped in beamspace by 11 phase modes, resolving two narrowband sources with angular positions: $\phi_{SoI} = 37.9°$, $\theta_{SoI} = 57.7°$, $\phi_{Int} = 120.5°$ and $\theta_{Int} = 50.7°$. SIR of 3dB, immerse in isotropic AWGN with SNR of 10 dB. Sample support of **1,000 snapshots**.

Element-Space Spectral MUSIC DoA
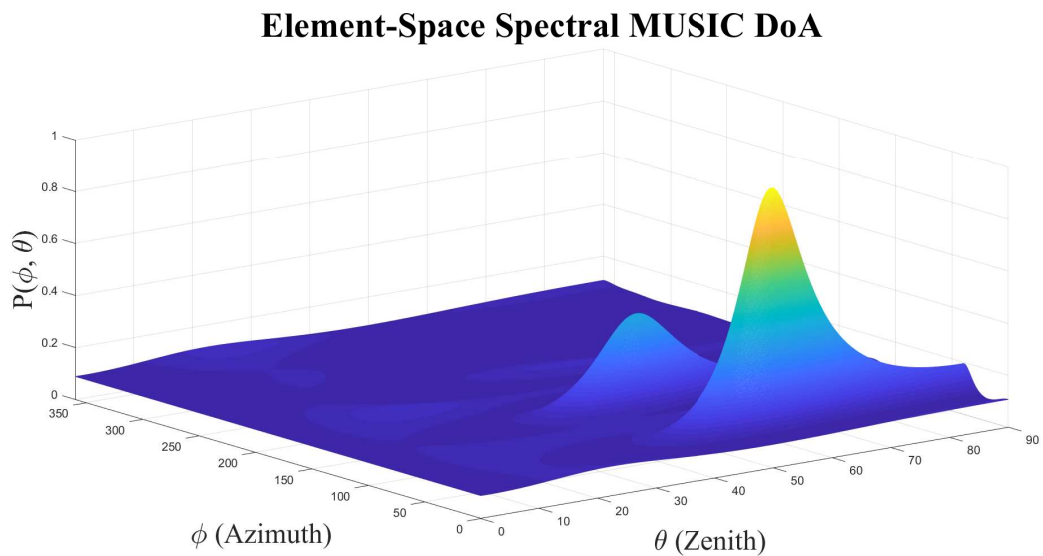
Figure 8 – Element space MUSIC pseudo-spectrum. 16 sensor UCA resolving two narrowband sources with angular positions: $\phi_{SoI} = 37.9°$, $\theta_{SoI} = 57.7°$, $\phi_{Int} = 120.5°$ and $\theta_{Int} = 50.7°$. SIR of 3 dB, immerse in isotropic AWGN with SNR of 10 dB. Small sample support of **10 snapshots**.

Beamspace Spectral MUSIC DoA
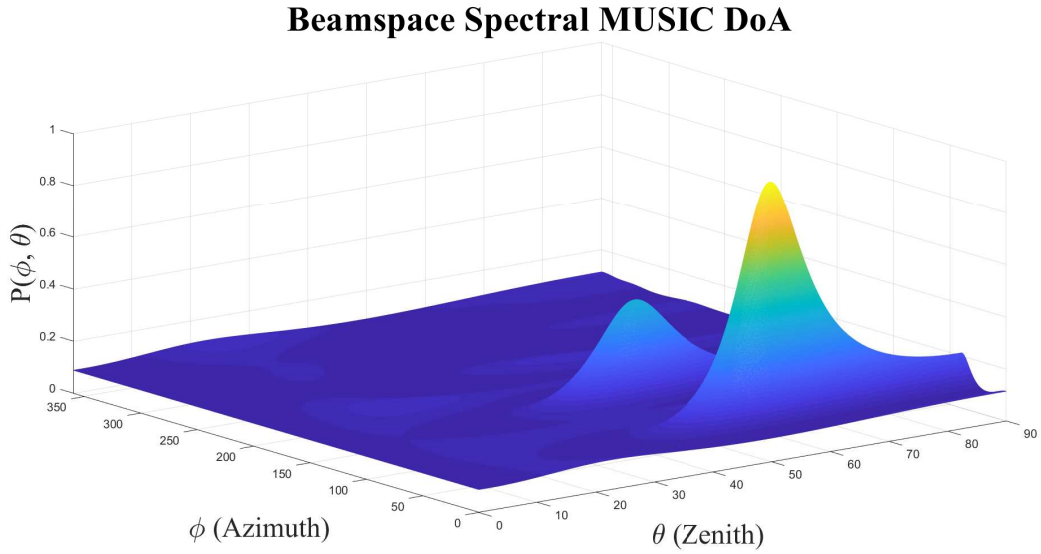
Figure 9 – Beamspace MUSIC pseudo-spectrum. 16 sensor UCA mapped in beamspace
by 11 phase modes, resolving two narrowband sources with angular positions:
$\phi_{SoI} = 37.9°$, $\theta_{SoI} = 57.7°$, $\phi_{Int} = 120.5°$ and $\theta_{Int} = 50.7°$. SIR of 3 dB, immerse
in isotropic AWGN with SNR of 10 dB. Small sample support of **10 snapshots**.

3.4   Decoupled Beamspace Root-MUSIC and Spectral MUSIC DoA Estimation

Beamspace Root-MUSIC algorithms deal with the Vandermonde-structured portion
of the beamspace array manifold. This portion is exclusively azimuth-dependent. The
zenith-dependent portion does not have a Vandermonde structure. Therefore, zenith DoA
estimation can not resort to polynomial rooting. We show a simple two-step scheme for
2-D DoA in Algorithm 4. First, the azimuth DoA is estimated via Root-MUSIC, assuming
an arbitrary θ_{ini}. Second, we perform D 1-D Spectral MUSIC searches through the zenith
angle parameter $\theta \in [0, \pi/2]$.

The initial zenith angle θ_{ini} for each source is considered previously estimated,
chosen arbitrarily or the array and the sources are considered in the same plane (zenith
angle $\theta = 90°$), and the 2-D DoA estimation is not explicitly explored. This scheme benefits
from the aspects of beamspace Root-MUSIC and associated techniques and resolves 2-DoA
with greatly reduced computational effort compared with 2-D Spectral MUSIC.

Fig. 11-14 depict a single trial of our decoupled 2-D DoA estimation in the same
condition of Section 3.2 for $\theta_{ini} = 90°$. In Fig. 11 and 13 we have the azimuth DoA solution
via Root-MUSIC in the z-plane, where the DoAs are the two roots closest to the unit
circle. With these two azimuth solutions, we proceed to a 1-D search (θ-only) spectral
MUSIC solution for the azimuth parameter, as shown in Fig. 12 and 14. These results were
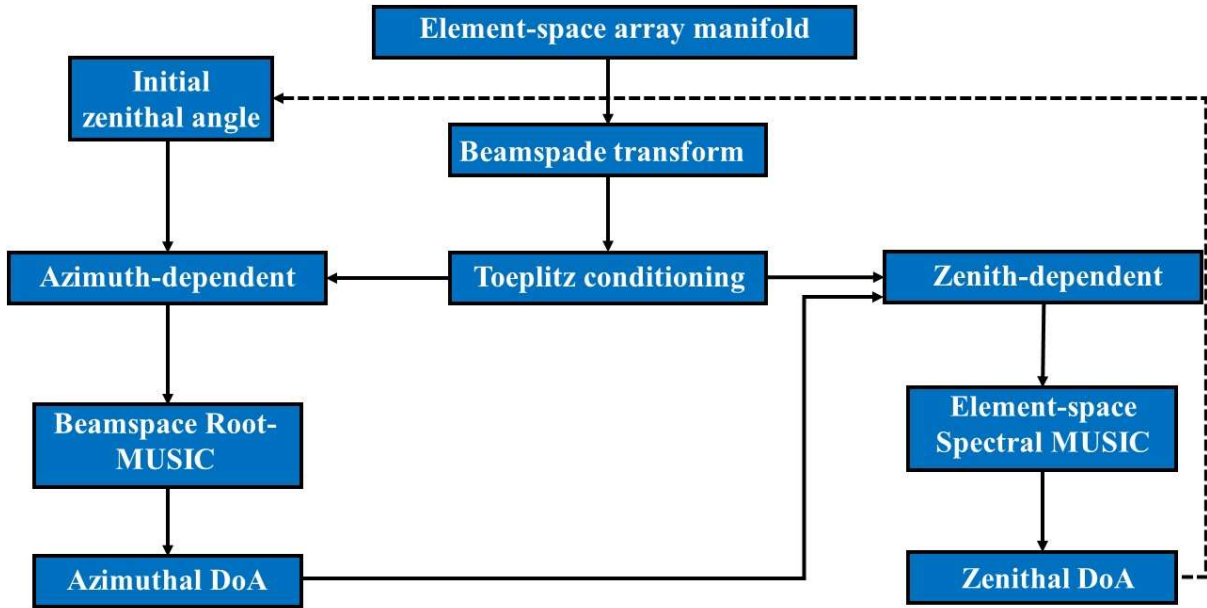
Figure 10 – Our UCA 2-D DoA approach diagram.

obtained from a simulation with the following parameters: Two stochastic and uncorrelated narrowband sources with angular positions: SoI with $\phi_{SoI} = 37.9°$, $\theta_{SoI} = 57.7°$, and Interferer with $\phi_{Int} = 120.5°$, $\theta_{Int} = 50.7°$ with central frequencies of 6 kHz and 7 kHz. SIR of 3 dB, immerse in isotropic AWGN with SNR of 10 dB.

Figure 11 – Z-plane Root-MUSIC azimuth solution. 16 sensor UCA mapped in beamspace by 11 phase modes, resolving two narrowband sources with angular positions $\phi_{SoI} = 37.9°$ and $\phi_{Int} = 120.5°$. SIR of 3 dB and SNR of 10 dB. Sample support of **1,000 snapshots**.

Zenith MUSIC Spectrum
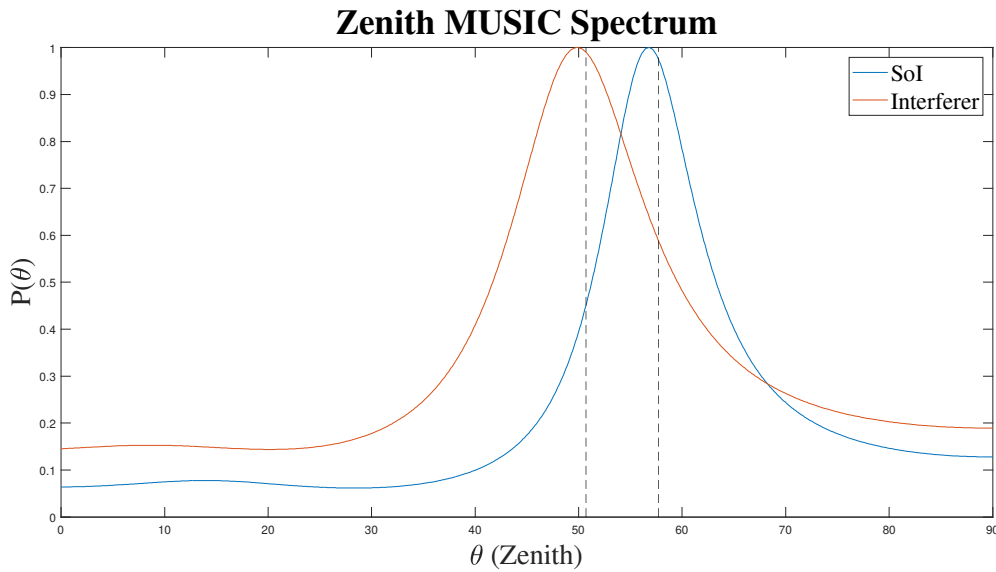
Figure 12 – 1-D search Spectral MUSIC zenith solution. 16 sensor UCA, resolving two narrowband sources with angular positions $\theta_{SoI} = 57.7°$ and $\theta_{Int} = 50.7°$. SIR of 3 dB and SNR of 10 dB. Sample support of **1,000 snapshots**.

Z-Plane Root-MUSIC Solution (Azimuth DoA)
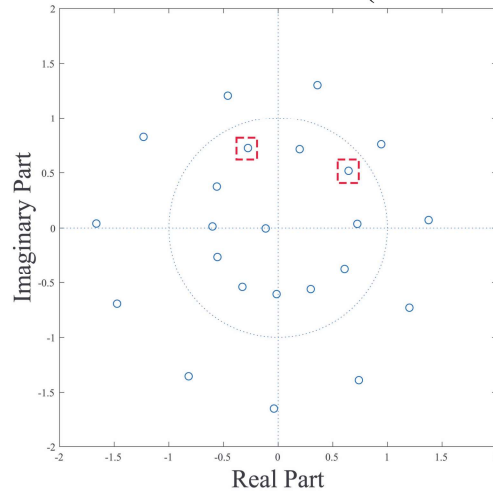
Figure 13 – Z-plane Root-MUSIC azimuth solution. 16 sensor UCA mapped in beamspace by 11 phase modes, resolving two narrowband sources with angular positions $\phi_{SoI} = 37.9°$ and $\phi_{Int} = 120.5°$. SIR of 3 dB and SNR of 10 dB. Small sample support of **10 snapshots**.

This scheme benefits from the aspects of beamspace Root-MUSIC and associated techniques and resolves 2-DoA with greatly reduced computational effort compared with 2-D Spectral MUSIC.

Additionally, the uncoupled DoA estimation with Spectral MUSIC for zenith
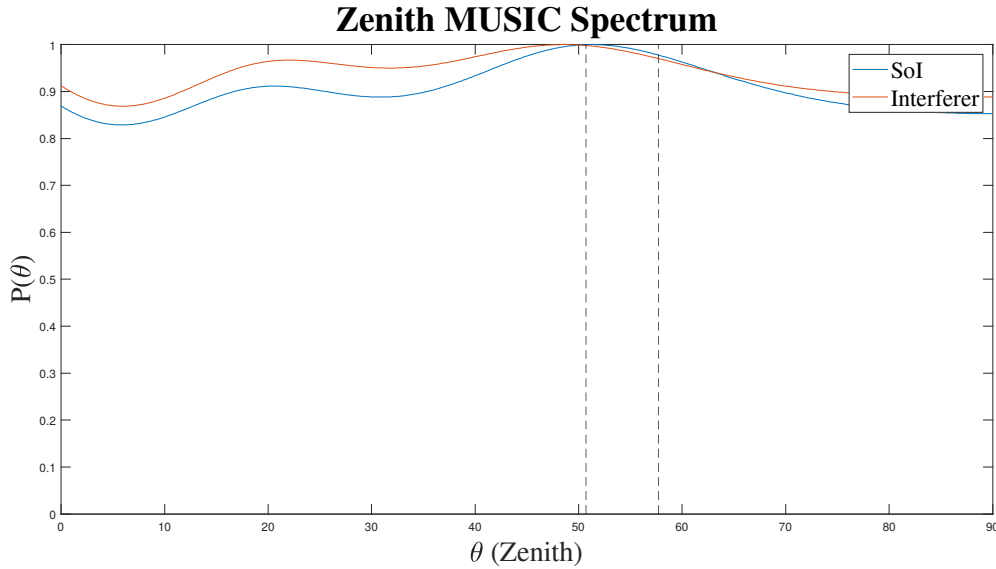
Figure 14 – 1-D search Spectral MUSIC zenith solution. 16 sensor UCA, resolving two narrowband sources with angular positions $\theta_{SoI} = 57.7°$ and $\theta_{Int} = 50.7°$. SIR of 3 dB and SNR of 10 dB. Small sample support of **10 snapshots**.

estimation counts with the beneficial feature that errors in azimuth estimation, up to a certain degree, do not have a sensible effect in zenith estimation, as represented graphically in Figs. 15 and 16. There, we can see that, for an appreciable interval of azimuth angles, their respective Spectral MUSIC zenithal solutions are very similar. This behavior has a pronounced positive impact in the presence of limiting factors (reduced number of sensors and small sample support), as will be addressed in Chapter 4. Limited sampling and mitigation techniques have larger effects on azimuth DoA, as deal mainly with beamspace Root-MUSIC algorithm. Consequently, errors in azimuth estimation do not propagate to zenith estimation directly, as corroborated by the smaller estimation errors in zenith DoA in the results in Sections 5.1 and 5.2.

3.5   Non-Isotropic Zenithal DoA Behavior

The planar geometry of the UCA results in zenithal non-isotropic behavior, which can affect the accuracy of azimuth and zenith DoA estimations. As the zenithal angle of a source progressively approaches the array plane (as it increases), the estimation of zenith DoA improves RUDGE, 1982. At the same time, we have similar behavior with azimuth DoA, where, as the source's zenithal angle approaches the array plane, the azimuth DoA also improves. These effects suggest an optimum zenithal sector of larger zenithal angles (around the array plane) that provides accurate 2-D DoA estimation.

Fig. 17-20 illustrate these effects for the cases of single and double sources, using the
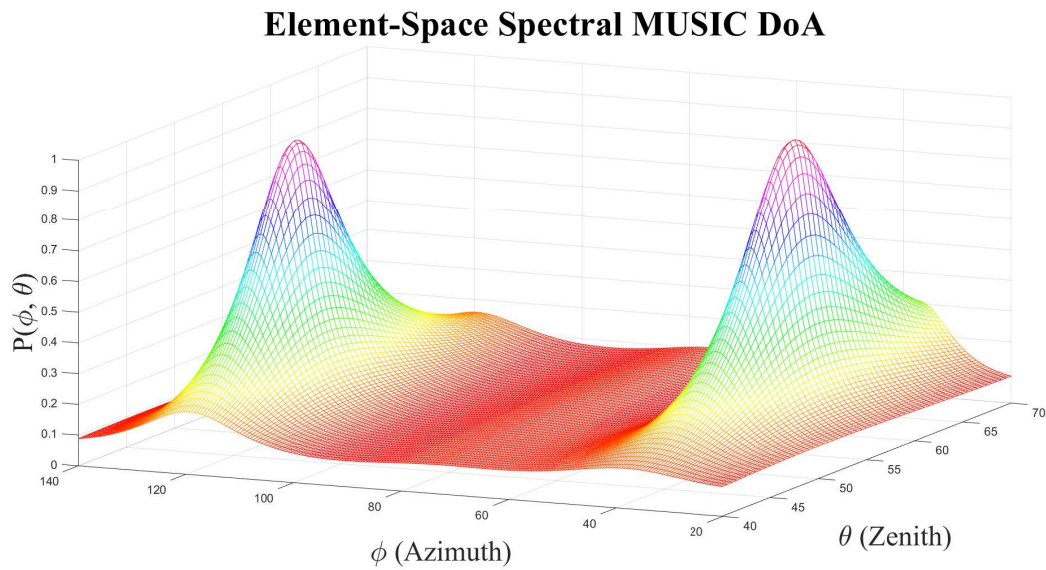
Figure 15 – 3-D representation of an angular portion of element-space 2-D MUSIC pseudo-spectrum. 16 sensor UCA, SIR of 3 dB, and SNR of 10 dB. Resolving two sources with angular positions $\phi_{SoI} = 37.9°$, $\theta_{SoI} = 57.7°$, $\phi_{Int} = 120.5°$ and $\theta_{Int} = 50.7°$. Small sample support of **10 snapshots**.
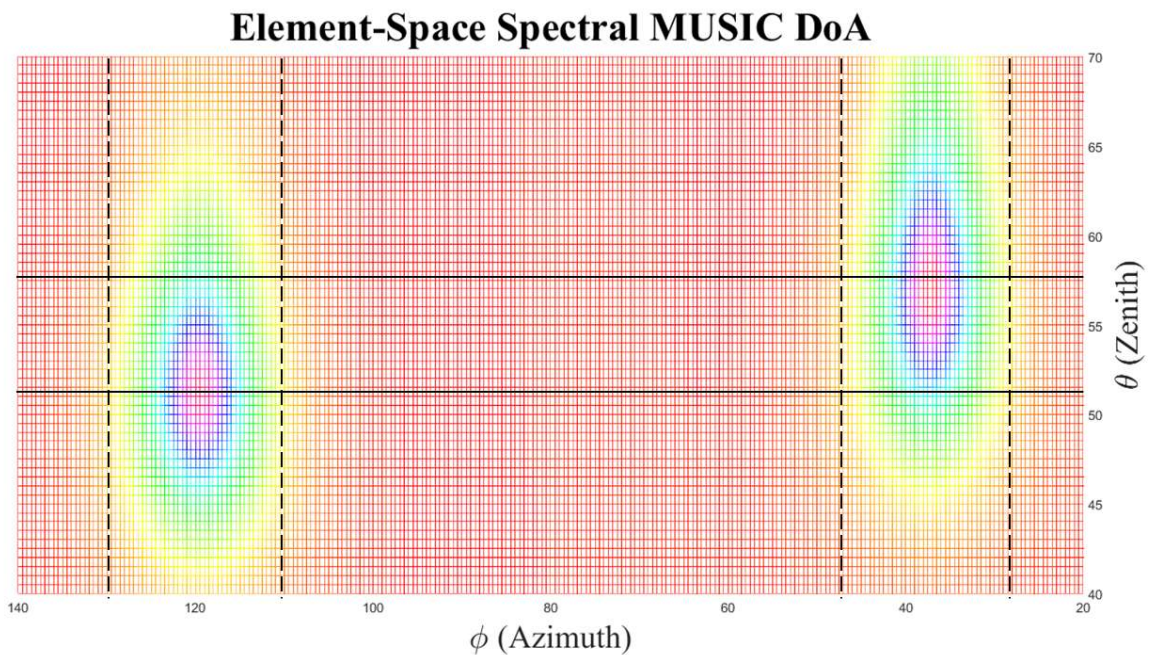
Figure 16 – Visual representation of the effects of azimuth DoA in zenith DoA estimations. Element-space spectral MUSIC 2-D DoA estimation. 16 sensor UCA, SIR of 3 dB, and SNR of 10 dB. Sources simulated angular positions are $\phi_{SoI} = 37.9°$, $\theta_{SoI} = 57.7°$, $\phi_{Int} = 120.5°$ and $\theta_{Int} = 50.7°$ and small sample support of **10 snapshots**. Filled lines indicate zenith DoAs θ_{SoI} and θ_{Int} and dashed lines represent intervals of azimuth DoA errors that have marginal effects on zenith DoA estimation accuracy.

DoA estimation method described in Section 3.4. It shows the results of DoA estimation error of a 16 sensor UCA (11 phase modes) × zenith for one and two sources: SoI ($\phi_{SoI} = 37.9°$ and $\theta_{SoI} \in [10°, 90°]$) and interferer ($\phi_{Int} = 120.5°$ and $\theta_{Int} = 50.7°$). We performed 1,000 independent runs of 1,000 snapshots each, $R = \lambda$, SIR of 3 dB, and AWGN with SNR of 5 dB.

From these figures, we conclude that the absolute DoA error tends to decrease with increasing source zenithal angle. For the two sources simulation, this behavior is altered around the zenith of the Interferer, set to 50.7°, compromising mainly azimuth estimation accuracy.
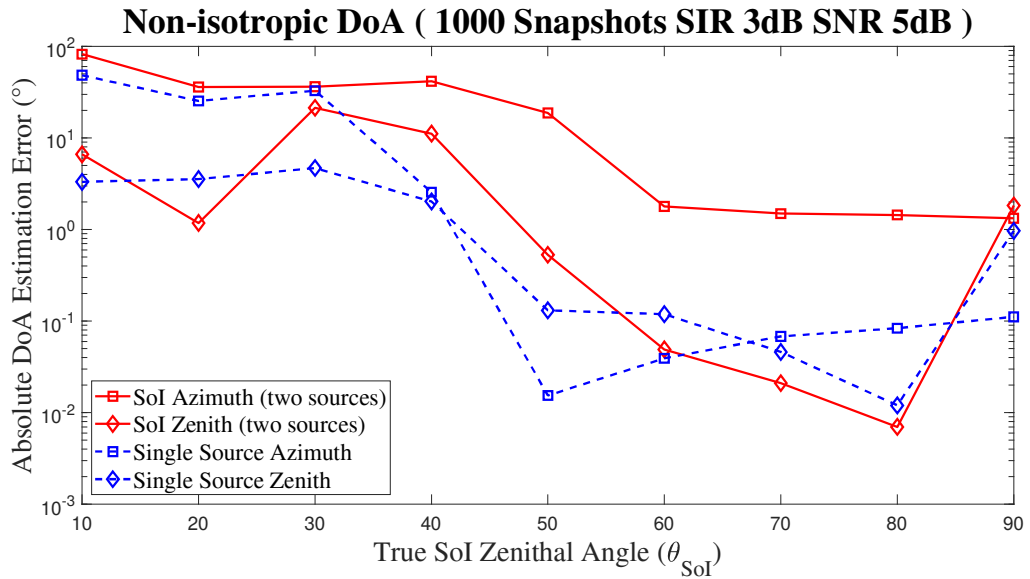
Figure 17 – Non-isotropic zenith-dependant DoA behavior. 16 sensor UCA, mapped in beamspace by 11 phase modes, resolving single and two narrowband sources with angular positions: $\phi_{SoI} = 37.9°$, $\theta_{SoI} \in [10°, 90°]$, $\phi_{Int} = 120.5°$ and $\theta_{Int} = 50.7°$. Note how the zenithal proximity with the Interferer affects azimuth DoA.

In Fig. 19 and 20, small sample support has additional effects on non-isotropic behavior, as well as the mitigating techniques in Section 4.2. As expected, we have less accurate DoA estimations in all cases, where azimuth DoA suffers greater effects. The compromise between zenithal angle and DoA estimation is less severe. The negative impact of the Interferer is also less severe.

RUDGE, 1982; TREES, 2007; WAITE, 2002; MARAGE; MORI, 2013 already indicate the behavior obtained in our simulations. However, it is important to mention as it will influence all other results presented in this work, especially regarding the effects of an SoI and Interferer with small vertical separation, whit both zenithal angles close together.

Non-isotropic DoA (1000 Snapshots SIR 5dB SNR 10dB)
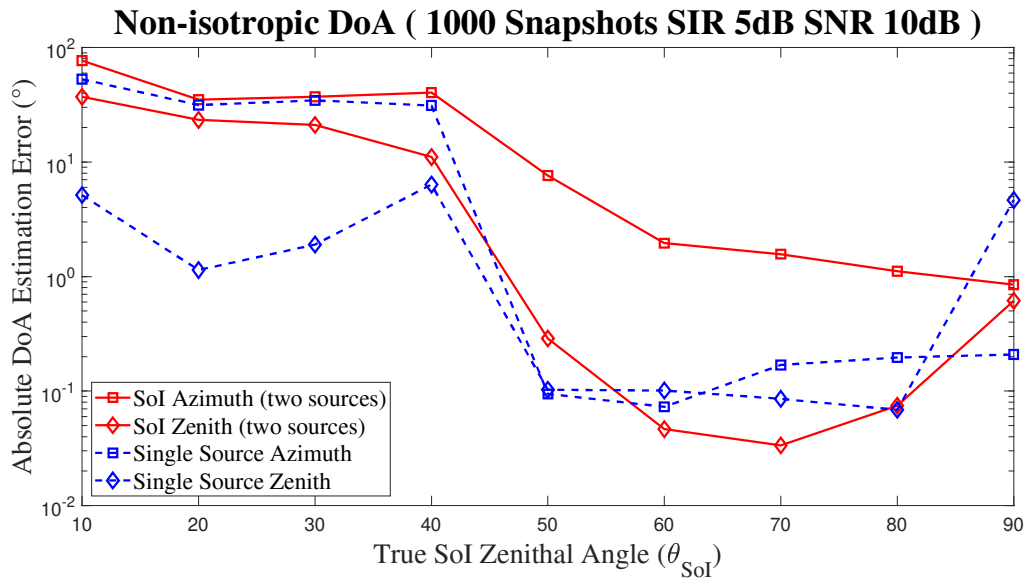
Figure 18 – Non-isotropic zenith-dependant DoA behavior. 16 sensor UCA, mapped in beamspace by 11 phase modes, resolving single and two narrowband sources with angular positions: $\phi_{SoI} = 37.9°$, $\theta_{SoI} \in [10°, 90°]$, $\phi_{Int} = 120.5°$ and $\theta_{Int} = 50.7°$. With better SNR and SIR, the effects of zenithal proximity are more evident.

Non-isotropic DoA (10 Snapshots SIR 3dB SNR 5dB)
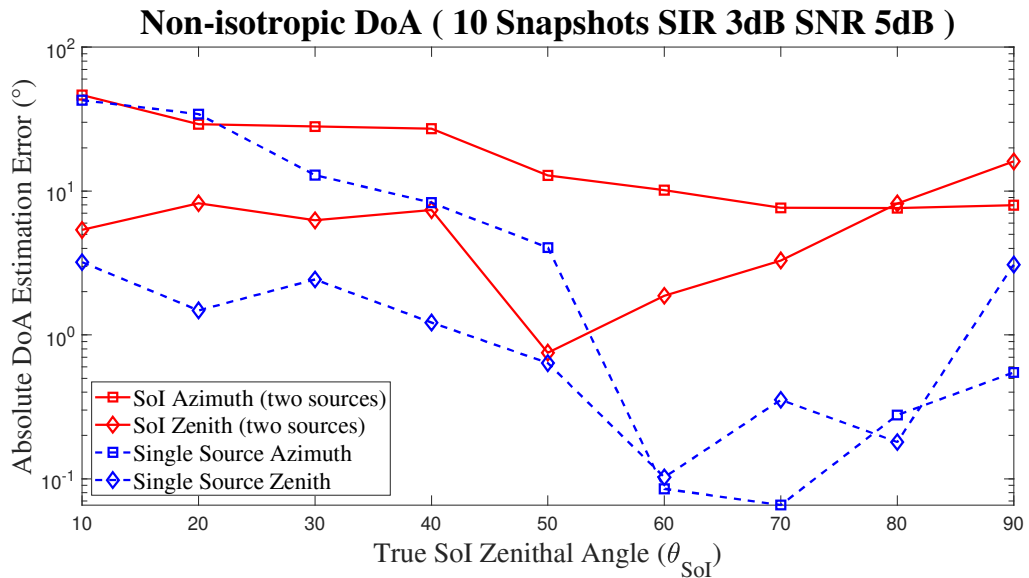
Figure 19 – Small Sample Support, non-isotropic zenith-dependant DoA behavior. 16 sensor UCA, mapped in beamspace by 11 phase modes, resolving single and two narrowband sources with angular positions: $\phi_{SoI} = 37.9°$, $\theta_{SoI} \in [10°, 90°]$, $\phi_{Int} = 120.5°$ and $\theta_{Int} = 50.7°$. Reduced sample support exacerbates the previous behavior.

The next chapter assesses DoA estimation with reduced spatial and temporal sampling. A reduced number of sensors leads to inaccurate beamspace mapping, so we
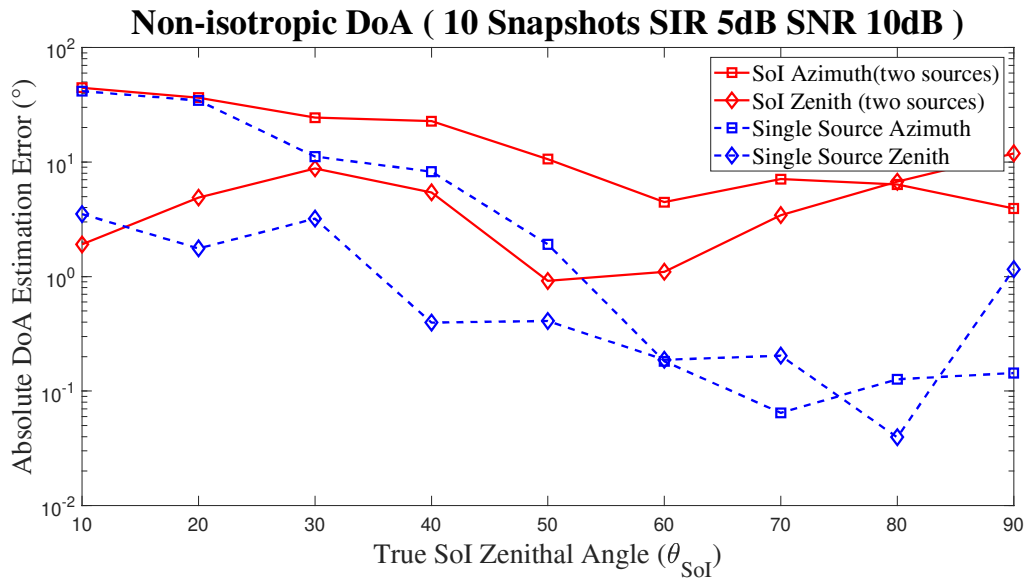
Figure 20 – Small Sample Support, non-isotropic zenith-dependant DoA behavior. 16 sensor UCA, mapped in beamspace by 11 phase modes, resolving single and two narrowband sources with angular positions: $\phi_{SoI} = 37.9°$, $\theta_{SoI} \in [10°, 90°]$, $\phi_{Int} = 120.5°$ and $\theta_{Int} = 50.7°$. Better SNR and SIR slightly made up for negative small sample support effects.

discuss the incorporation of additional phase modes. Small sample support, as well as low SNR correlated signal sources, lead to subspace leakage, so we assess methods of conditioning the covariance matrix to mitigate the negative effects of these limiting factors.

4 REDUCED SPATIAL AND TEMPORAL SAMPLING DOA ESTIMATION

In this chapter, we assess the performance of a Uniform Circular Array featuring a reduced number of sensors and using sample support comprised of only a few snapshots. We begin by analyzing the limitations of the phase-mode transformation in the context of a uniform circular array with a reduced number of sensors. Next, we address the issue of having limited sample support, which generates additional challenges, followed by a summary of the techniques that can be used to mitigate the degradation caused by the two aforementioned problems.

4.1 DoA Estimation With Reduced Quantity of Sensors

As shown in Section 3.2, specifically in Eq. (3.25) and graphically in Fig. 4, the number of phase modes capable of exciting a circular array with sensible amplitude depends on $Y\bar{R}$, which translates into operating frequency, radius, and number of sensors.
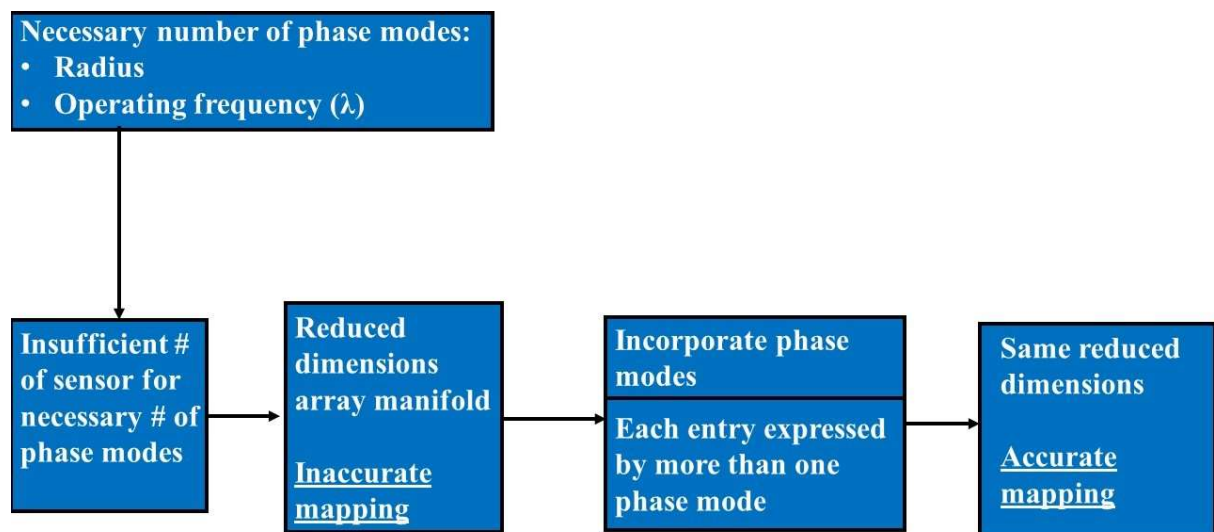
Figure 21 – Spatial aliased DoA estimation: additional phase modes incorporation diagram.

The number of phase modes must allow for precise description of the receiving characteristics of the array in beamspace, otherwise, biased DoA estimations shall occur GOOSSENS; ROGIER; WERBROUCK, 2008. The two criteria of Eq. (3.25) can conflict when there are fewer sensors than required to having sufficient phase modes and unbiased estimations. With sufficient sensors, each phase mode can be precisely expressed by a single Bessel function of the first kind WAX; SHEINVALD, 1994. For an insufficient number of

sensors, which can be considered as a sparse array, indicated by the subscript (sp), Eq. (3.24) does not hold and each phase mode is expressed more closely by Eq. (3.22).

Considering a sparse UCA with only M_{sp} sensors, $M_{sp} < M$, capable of exciting only $n_{sp} = (2N_{sp} + 1)$ phase modes, with $n_{sp} < n$, due to the reduced number of sensors. However, the corresponding circular aperture (defined by the radius and the operating frequency) needs a larger number of sensors to be sampled without aliasing, resulting in the need for $(2N + 1)$ phase modes to express correctly the receiving characteristics in beamspace.

The additional $2N - 2N_{sp}$ phase modes required cannot be incorporated into the reduced-dimension beamspace array manifold $\bar{\mathbf{x}}_{sp}(k)$ unless each entry $\bar{x}_{n_{sp}}(k)$, $n_{sp} \in [-N_{sp}, \ldots, -1, 0, 1, \ldots, N_{sp}]$, is expressed by more than one phase mode GOOSSENS; ROGIER; WERBROUCK, 2008; LI; CHEN, 2016. The array manifold with additional incorporated phase mode is specified by the subscript (ad).

According to Eq. (3.23), it is possible to make $l \neq 0$ and equals an integer that, by expressing each $\bar{x}_{n_{sp}}(k)$ by as many Bessel functions as necessary, fulfills the criteria of Eq. (3.25). In this fashion, $(2N + 1)$ phase modes are incorporated in $\bar{x}_{n_{sp}}(k)$, even when it has only $(2N_{sp} + 1) < (2N + 1)$ entries, with each entry of $\bar{x}_{n_{sp}}(k)$ expressed by

$$
\begin{aligned}
\bar{x}_{n_{sp}}(k) = s(k)\sqrt{M} \Big[&\mathrm{j}^{n_{sp}} J_{n_{sp}}\left(Y\bar{R}\right) \mathrm{e}^{(\mathrm{j}n_{sp}\phi)} \\
&+ \mathrm{j}^{\pm(n_{sp}+lM_{sp})} J_{\pm(n_{sp}+lM_{sp})}\left(Y\bar{R}\right) \mathrm{e}^{(\pm\mathrm{j}(n_{sp}+lM_{sp})\phi)} \Big],
\end{aligned}
\tag{4.1}
$$

with l such that $n_{sp} + lM_{sp} = n$.

Such a technique is implemented by constructing a phase mode incorporation matrix $\mathbf{H}$ in the form

$$
\mathbf{H} = \begin{bmatrix} \mathbf{D}_+ & \vdots & \mathbf{I} & \vdots & \mathbf{D}_- \end{bmatrix},
\tag{4.2}
$$

where $\mathbf{I}$ is the $(2N_{sp} + 1)$ identity matrix. $\mathbf{D}_+$ is a $(2N_{sp} + 1) \times (N - N_{sp})$ matrix of the $(N - N_{sp})$ last columns of $\mathbf{I}$ that incorporate phase modes of the form $\mathrm{j}^{(n_{sp}+lM_{sp})} J_{(n_{sp}+lM_{sp})}\left(Y\bar{R}\right) \mathrm{e}^{(\mathrm{j}(n_{sp}+lM_{sp})\phi)}$; and $\mathbf{D}_-$ is a $(2N_{sp}+1) \times (N - N_{sp})$ matrix of the $(N - N_{sp})$ first columns of $\mathbf{I}$ that incorporate phase modes of the form $\mathrm{j}^{(n_{sp}-lM_{sp})} J_{(n_{sp}-lM_{sp})}\left(Y\bar{R}\right) \mathrm{e}^{(\mathrm{j}(n_{sp}-lM_{sp})\phi)}$ for values of N_{sp} and N according to $3N_{sp} + 1 > N > N_{sp}$.

Also according to GOOSSENS; ROGIER; WERBROUCK, 2008, by incorporating additional identity matrices, the form of matrix $\mathbf{H}$ for any values of N and N_{sp} can be obtained. For example, when $5N_{sp} + 1 > N > 3N_{sp} + 1$,

$$
\mathbf{H} = \begin{bmatrix} \mathbf{D}_+ & \vdots & \mathbf{I} & \vdots & \mathbf{I} & \vdots & \mathbf{I} & \vdots & \mathbf{D}_- \end{bmatrix}.
\tag{4.3}
$$

Next, we devise an example of the method for the particular case of the simulations carried out in Subsection 5.1.1 and with a single source, $D = 1$. The sparse UCA has an aperture that requires $(2N + 1) = 11$ phase modes, but the array possesses only 6 sensors, being capable of exciting only $(2N_{sp} + 1) = 5$ phase modes. Starting with the ideal (theoretical) $(2N + 1)$ candidate array manifold $\bar{\mathbf{a}}(\phi)$ and the $(2N_{sp} + 1) \times 1$ sparse candidate array manifold $\bar{\mathbf{a}}_{sp}(\phi)$, we write

$$\bar{\mathbf{a}}(\phi) = \left[J_{-5}, J_{-4}, \ldots, J_{-1}, J_0, J_1, \ldots, J_4, J_5 \right]^{\mathrm{T}} \quad \text{and} \tag{4.4}$$

$$\bar{\mathbf{a}}_{sp}(\phi) = \left[J_{-2}, J_{-1}, J_0, J_1, J_2 \right]^{\mathrm{T}}, \tag{4.5}$$

where $J_n = \mathrm{j}^n J_n(Y\bar{R})\mathrm{e}^{\mathrm{j}n\phi}$.

The incorporation matrix $\mathbf{H}$ has the form

$$\mathbf{H} = \begin{bmatrix} 0 & 0 & 0 & 1 & 0 & 0 & 0 & 0 & 1 & 0 & 0 \\ 0 & 0 & 0 & 0 & 1 & 0 & 0 & 0 & 0 & 1 & 0 \\ 1 & 0 & 0 & 0 & 0 & 1 & 0 & 0 & 0 & 0 & 1 \\ 0 & 1 & 0 & 0 & 0 & 0 & 1 & 0 & 0 & 0 & 0 \\ 0 & 0 & 1 & 0 & 0 & 0 & 0 & 1 & 0 & 0 & 0 \end{bmatrix}. \tag{4.6}$$

The $(2N_{sp} + 1) \times 1$ array manifold with additional phase modes incorporated, $\bar{\mathbf{a}}_{ad}(\phi)$, is obtained by

$$\begin{aligned} \bar{\mathbf{a}}_{ad}(\phi) &= \mathbf{H}\bar{\mathbf{a}}_{sp}(\phi) \\ &= \left[(J_{-2} + J_3), (J_{-1} + J_4), (J_{-5} + J_0 + J_5), (J_1 + J_{-4}), (J_2 + J_{-3}) \right]^{\mathrm{T}}. \end{aligned} \tag{4.7}$$

We can see that $\bar{\mathbf{a}}_{ad}(\phi)$, despite having the same dimensions $(2N_{sp} + 1) = 5$, is expressed by $(2N + 1) = 11$ phase modes, in comparison with $\bar{\mathbf{a}}_{sp}(\phi)$, which is expressed by only $(2N_{sp} + 1) = 5$ phase modes. In this manner, $\bar{\mathbf{a}}_{ad}$ replaces $\bar{\mathbf{a}}_{sd}$ as the $(2N_{sp} + 1) = 5$ array manifold vector.

According to Eq. (3.22) and (3.25), $\bar{\mathbf{a}}_{ad}$ will map the array manifold in beamspace with improved accuracy, minimizing the effects of insufficient spatial sampling. Finally, $\bar{\mathbf{a}}_{ad}$ can be used to calculate the coefficients of Root-MUSIC as in Section 3.3, improving estimations.

4.2 DoA Estimation With Small Sample Support

Phase modes-based beamformer and root-MUSIC allow more computationally efficient and less time-consuming DoA estimation. In this way, the detection and sampling processes can be reduced as well, which translates into a reduced quantity of snapshots for estimation. A less costly technique, such as root-MUSIC, can be paired with reduced sample support for each DoA solution.

In practical situations, we are unable to obtain the true covariance matrix, due to the finite quantity of input data. Consequently, only data-dependent estimations are attainable HACKER; YANG, 2010, the sample covariance matrices, represented in this Section onward by the superscript (ˆ).

To deal with this problem, several methods emulate the effects of the temporal averaging of the estimation with a large number of snapshots REDDY; REDDY, 1999; LI; SU; WU, 2019. By presuming a suitable structure of the covariance matrix (according to array and signal models), it is possible to condition the sample covariance matrix to this suitable structure. Such conditioning goes through distinct methods for estimating the covariance matrix in order to minimize the undesired effects of an insufficient quantity of snapshots.
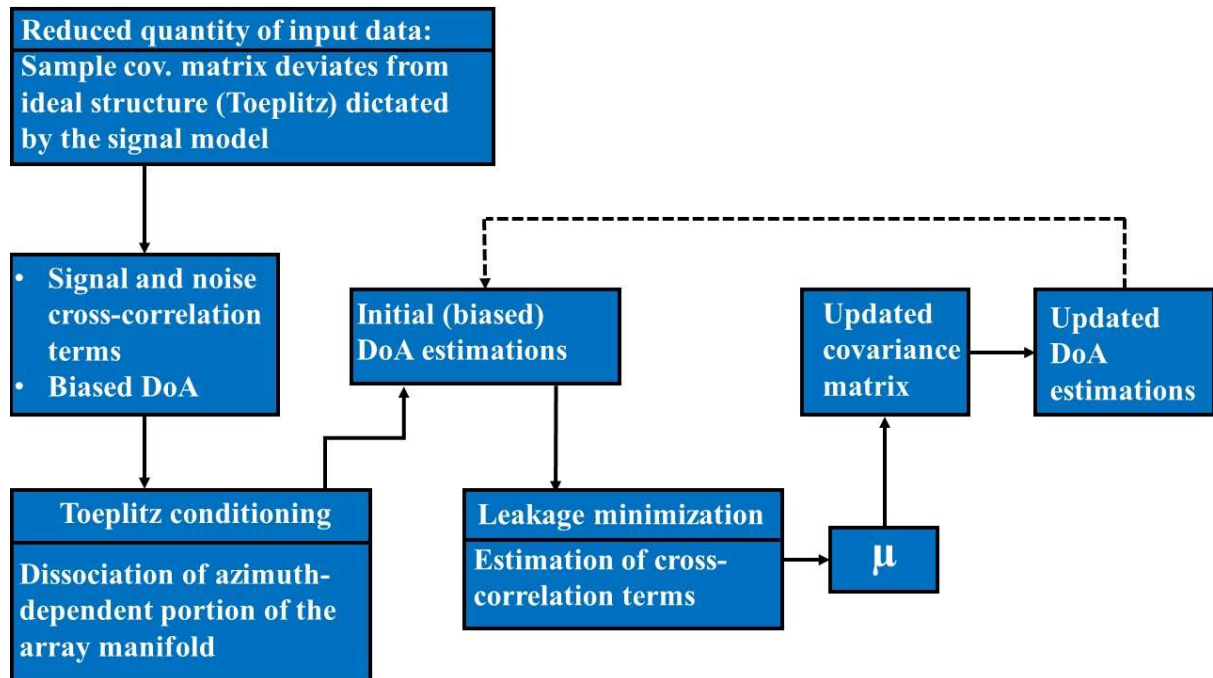
Figure 22 – Small sample support DoA estimation diagram.

4.2.1 Leakage Minimization: Covariance matrix revision via cross-correlation estimation

For DoA estimation and, particularly subspace-based methods, the fidelity of the sample covariance matrix with respect to the covariance matrix is critical. In cases of low SNR or a small quantity of input data, the true and sample covariance matrices may diverge considerably. A reduced number of snapshots can introduce a bias to the solution. Residual components of cross-correlation between signal and noise samples, that would fade with an increasing number of snapshots and, eventually, become negligible, will remain significant for the reduced sample support case SHAGHAGHI; VOROBYOV, 2015; XINGXING et al., 2016; WEN; WANG, 2017 and the sample covariance matrix would diverge from the covariance matrix.

The undesired residual components of cross-correlation can result in the signal and noise subspaces of the covariance matrix not being perfectly orthogonal, with an overlap (subspace leakage). This can considerably degrade the estimation of any subspace-based methods. We can reduce this divergence by estimating the residual components and revising the sample covariance matrix, utilizing initial DoA (containing errors) via a least squares problem to estimate the residual and remove them, as shown in Algorithm 5.

Starting with Eq. (3.33), where the number of snapshots $K \to \infty$. For a finite number of snapshots, we have the estimated beamspace sample covariance matrix $\hat{\mathbf{R}}_{\bar{x}}$ given as

$$
\begin{aligned}
\hat{\mathbf{R}}_{\bar{x}} &= \frac{1}{K} \sum_{k=1}^{K} \hat{\mathbf{x}}(k)\hat{\mathbf{x}}^{\mathrm{H}}(k) \\
&= \frac{1}{K} \sum_{k=1}^{K} \left(\mathbf{W}^{\mathrm{H}}\mathbf{A}(\phi)\hat{\mathbf{s}}(k) + \hat{\mathbf{n}}(k) \right) \left(\mathbf{W}^{\mathrm{H}}\mathbf{A}(\phi)\hat{\mathbf{s}}(k) + \hat{\mathbf{n}}(k) \right)^{\mathrm{H}}.
\end{aligned}
\tag{4.8}
$$

Expanding the summation of outer products above yields

$$
\begin{aligned}
\hat{\mathbf{R}}_{\bar{x}} =& \frac{1}{K} \sum_{k=1}^{K} \left(\mathbf{W}^{\mathrm{H}}\mathbf{A}(\phi)\hat{\mathbf{s}}(k) + \hat{\mathbf{n}}(k) \right) \left(\mathbf{W}^{\mathrm{H}}\mathbf{A}(\phi)\hat{\mathbf{s}}(k) + \hat{\mathbf{n}}(k) \right)^{\mathrm{H}} \\
=& \mathbf{W}^{\mathrm{H}}\mathbf{A}(\phi)\hat{\mathbf{R}}_s\mathbf{A}^{\mathrm{H}}(\phi)\mathbf{W} + \mathbf{W}^{\mathrm{H}}\hat{\mathbf{R}}_n\mathbf{W} \\
&+ \mathbf{W}^{\mathrm{H}}\mathbf{A}(\phi) \left[\frac{1}{K} \sum_{k=1}^{K} \hat{\mathbf{s}}(k)\hat{\mathbf{n}}^{\mathrm{H}}(k) \right] \\
&+ \left[\frac{1}{K} \sum_{k=1}^{K} \hat{\mathbf{n}}(k)\hat{\mathbf{s}}^{\mathrm{H}}(k) \right] \mathbf{A}(\phi)^{\mathrm{H}}\mathbf{W},
\end{aligned}
\tag{4.9}
$$

where $\hat{\mathbf{R}}_s = \frac{1}{K} \sum_{k=1}^{K} \hat{\mathbf{s}}(k)\hat{\mathbf{s}}^{\mathrm{H}}(k)$ and $\hat{\mathbf{R}}_n = \frac{1}{K} \sum_{k=1}^{K} \hat{\mathbf{n}}(k)\hat{\mathbf{n}}^{\mathrm{H}}(k)$ are element-space sample covariance matrices of the reference signal in the center of the array and the noise process, respectively.

The first two terms os Eq. (4.9) are a good estimate of $\hat{\mathbf{R}}_{\bar{x}}$ in the sense that $\hat{\mathbf{R}}_{\bar{x}} \approx \mathbf{W}^{\mathrm{H}}\mathbf{A}(\phi)\hat{\mathbf{R}}_s\mathbf{A}^{\mathrm{H}}(\phi)\mathbf{W} + \mathbf{W}^{\mathrm{H}}\hat{\mathbf{R}}_n\mathbf{W}$ and that $\hat{\mathbf{R}}_{\bar{x}}$ converges to $\mathbf{R}_{\bar{x}}$ when $K \to \infty$ The

last two terms, the residual cross-correlation terms in Eq. (4.9) due to subspace leakage SHAGHAGHI; VOROBYOV, 2015 are

$$
\hat{\mathbf{T}} = \mathbf{W}^{\mathrm{H}}\mathbf{A}(\phi) \left[\frac{1}{K}\sum_{k=1}^{K}\hat{\mathbf{s}}(k)\hat{\mathbf{n}}^{\mathrm{H}}(k)\right] \quad \text{and}
$$
$$
\hat{\mathbf{T}}^{\mathrm{H}} = \left[\frac{1}{K}\sum_{k=1}^{K}\hat{\mathbf{n}}(k)\hat{\mathbf{s}}^{\mathrm{H}}(k)\right] \mathbf{W}\mathbf{A}(\phi)^{\mathrm{H}}. \tag{4.10}
$$

With sufficient sample support, the first two terms of Eq. (4.9) would be dominant and the residuals of Eq. (4.10) would tend to zero. In other words, $\hat{\mathbf{R}}_{\bar{x}}$ tends to $\mathbf{R}_{\bar{x}}$ with growing number of samples.

Initially, we utilize the reduced sample support beamspace covariance matrix $\hat{\mathbf{R}}_{\bar{x}}$ and Root-MUSIC to obtain initial coarse DoA estimations $\{\phi'_1 \ldots \phi'_D\}$. These initial DoAs are used to obtain a new revised beamspace array manifold $\mathbf{W}^{\mathrm{H}}\mathbf{A}(\phi')$. The revised beamspace array manifold will be used to revise $\hat{\mathbf{R}}_{\bar{x}}$ SHAGHAGHI; VOROBYOV, 2015. To achieve the revision, we rewrite the residual in terms of $\mathbf{W}^{\mathrm{H}}\mathbf{A}(\phi')$.

Starting by estimating the beamspace noise vector as $\hat{\mathbf{n}}(k) = \hat{\mathbf{x}}(k) - \mathbf{A}(\phi')\hat{\mathbf{s}}(k)$ and substituting in Eq. (3.32), we can estimate the signal $\hat{\mathbf{s}}(k)$ in the center of the array in terms of $\mathbf{W}^{\mathrm{H}}\mathbf{A}(\phi')$ in a least square sense by minimizing the cost function

$$
\hat{\mathbf{s}}(k) = \arg\min \left\|\mathbf{x}(k) - \mathbf{W}^{\mathrm{H}}\mathbf{A}(\phi')\mathbf{s}\right\|, \tag{4.11}
$$

and we obtain the least squares estimation TREFETHEN; BAU, 1997 for $\hat{\mathbf{s}}(k)$ in function of $\mathbf{W}^{\mathrm{H}}\mathbf{A}(\phi')$ as

$$
\hat{\mathbf{s}}(k) = \left(\mathbf{A}^{\mathrm{H}}(\phi')\mathbf{W}\mathbf{W}^{\mathrm{H}}\mathbf{A}(\phi')\right)^{-1}\mathbf{A}^{\mathrm{H}}(\phi')\mathbf{W}\bar{\mathbf{x}}(k). \tag{4.12}
$$

Following, we substitute $\hat{\mathbf{s}}(k)$ of Eq. (4.12) in the expression for the residuals of Eq. (4.10). We only develop formulations for $\hat{\mathbf{T}}$ and the expression for the other residual term is easily obtainable.

$$
\hat{\mathbf{T}} = \mathbf{W}^{\mathrm{H}}\mathbf{A}(\phi') \left[\frac{1}{K}\sum_{k=1}^{K}\hat{\mathbf{s}}(k)\hat{\mathbf{n}}^{\mathrm{H}}(k)\right]
$$

$$
= \mathbf{W}^{\mathrm{H}}\mathbf{A}(\phi')\frac{1}{K}\sum_{k=1}^{K}\overbrace{\left[\left(\mathbf{A}^{\mathrm{H}}(\phi')\mathbf{W}\mathbf{W}^{\mathrm{H}}\mathbf{A}(\phi')\right)^{-1}\hat{\mathbf{A}}^{\mathrm{H}}(\phi')\mathbf{W}\bar{\mathbf{x}}(k)\right]}^{\hat{\mathbf{s}}(k)} \tag{4.13}
$$

$$
\underbrace{\left[\bar{\mathbf{x}}^{\mathrm{H}}(k) - \bar{\mathbf{x}}^{\mathrm{H}}(k)\mathbf{W}^{\mathrm{H}}\mathbf{A}(\phi')\left(\mathbf{A}^{\mathrm{H}}(\phi')\mathbf{W}\mathbf{W}^{\mathrm{H}}\mathbf{A}(\phi')\right)^{-1}\mathbf{A}^{\mathrm{H}}(\phi')\mathbf{W}\right]}_{\hat{\mathbf{n}}^{\mathrm{H}}(k) = (\hat{\mathbf{x}}(k) - \mathbf{W}^{\mathrm{H}}\mathbf{A}(\phi')\hat{\mathbf{s}}(k))^{\mathrm{H}}}.
$$

By taking the terms independent of k out of the summation and rearranging the ones inside, we obtain

$$\hat{\mathbf{T}} = \mathbf{P} \left[\frac{1}{K} \sum_{k=1}^{K} \hat{\mathbf{x}}(k)\hat{\mathbf{x}}^{\mathrm{H}}(k) \left(\mathbf{I}_{(2N+1)} - \mathbf{P} \right) \right]$$

$$= \mathbf{P}\hat{\mathbf{R}}_{\bar{x}} \left(\mathbf{I}_{(2N+1)} - \mathbf{P} \right),$$

(4.14)

where $\mathbf{P} = \mathbf{W}^{\mathrm{H}}\mathbf{A}(\phi') \left(\mathbf{A}^{\mathrm{H}}(\phi')\mathbf{W}\mathbf{W}^{\mathrm{H}}\mathbf{A}(\phi') \right)^{-1} \mathbf{A}^{\mathrm{H}}(\phi')\mathbf{W}$ is the estimated signal subspace projector and $\mathbf{I}_{(2N+1)} - \mathbf{P}$ is the respective orthogonal projector.

Calculating initial error estimates based on initial DoAs, we can write $\hat{\mathbf{R}}'_{\bar{x}}$ as the revised beamspace covariance matrix $\hat{\mathbf{R}}_{\bar{x}}$.

$$\hat{\mathbf{R}}'_{\bar{x}} = \hat{\mathbf{R}}_{\bar{x}} - \mu \left(\hat{\mathbf{T}} + \hat{\mathbf{T}}^{\mathrm{H}} \right), \ \mu \in [0,1] .$$

(4.15)

According to Eq. (4.9), $\mu = 1$; however, the beamformer and the least-squares solution of $\hat{s}(k)$ retain a systematic error and the residual terms of Eq. (4.10) cannot be exactly estimated. In order to select the optimum value μ, we calculate the updated DoAs $\{\phi''_1 \ldots \phi''_D\}$ (a second iteration of DoA estimation) for each discrete increment of μ JIANG; MAO; LIU, 2016 and choose the optimum μ whose set of refined DoAs minimizes the element-space MUSIC spectrum

$$\mu = \arg \min \left\| \sum_{d-1}^{D} \mathbf{a}(\mu, \phi''_d)\mathbf{E}_N\mathbf{E}_N^{\mathrm{H}}\mathbf{a}^{\mathrm{H}}(\mu, \phi''_d) \right\|,$$

(4.16)

and the new DoAs are the ones calculated with the optimum μ.

4.2.2 Toeplitz Conditioning

Several techniques for reduced sample support estimated covariance matrix revision are based on the expected Toeplitz form of the true covariance matrix and in ways to approximate the estimated sample covariance matrix of this ideal Toeplitz structure XIAOFEI et al., 2007; LI; CHEN, 2016; DEGEN, 2017; WEN; WANG, 2017. However, this ideal structure corresponds to the true covariance matrix of a ULA under several assumptions.

Initially, considering a ULA and assuming all its sensors are identical (with identical receiving characteristics) and the absence of mutual coupling, its array manifold will have a Vandermonde structure. Moreover, the correlation of two sensors separated by the same Euclidean distance $\|\mathbf{p}_i - \mathbf{p}_j\|$ will have the same statistics. Consequently, the correlation $R_x(x_{m_i}, x_{m_j})$ of the output signal of two sensors m_i and m_j will be a function of only $\|\mathbf{p}_i - \mathbf{p}_j\|$, independent of the individual positions $\mathbf{p}_i$ and $\mathbf{p}_j$. In this manner, the true covariance matrix will have a Toeplitz structure.

However, the estimated sample covariance matrix, especially with reduced sample support, can deviate considerably from the Toeplitz matrix, and methods of estimation and conditioning such as spatial smoothing, in which the results are averaged in space (instead of averaging in time, in case of sufficient sample support) REDDY; REDDY, 1999 , and reducing the effects of few temporal snapshots.

When considering UCAs, the element-space array manifold $\mathbf{a}(\phi, \theta)$ of Eq. (3.10) does not have Vandermonde structure and the covariance matrix $\mathbf{R}_x$ of Eq. (3.11) is not Toeplitz because $R_x(x_{m_i}, x_{m_j}) = R_x(\mathbf{p}_i, \mathbf{p}_j)$ is no longer a function of $\|\mathbf{p}_i - \mathbf{p}_j\|$.

The phase mode transform maps the array manifold in beamspace and a portion of the beamspace array manifold in Eq. (3.30) has a center-symmetric Vandermonde structure, as a function of the azimuth angle θ, as in Eq. (3.31). By utilizing only the azimuth-dependant portion of $\bar{\mathbf{a}}(\phi)$, we have a Vandermonde array manifold and corresponding Toeplitz covariance matrix.

$$\mathbf{L}\bar{\mathbf{a}}(\phi) \cong \mathbf{v}(\mathrm{e}^{\mathrm{j}\phi}) = \left[z^{-N} \dots z^{-1}, 1, z \dots z^N \right]^{\mathrm{T}}, \tag{4.17}$$

with $z = \mathrm{e}^{\mathrm{j}\phi}$ and the matrix $\mathbf{L} = \mathrm{diag}[(\sqrt{M}\mathrm{j}^n J_n(K\bar{R}))^{-1}]$.

Additionally, we can employ spatial smoothing to $\hat{\mathbf{R}}_{\bar{x}}$ to minimize the effects of reduced sample support and condition it to a Toeplitz form to obtain suitable azimuth DoA estimations. The expression for the spatially-smoothed sample covariance matrix $\hat{\mathbf{R}}_{\bar{x}_{ss}}$ is

$$\hat{\mathbf{R}}_{\bar{x}_{ss}} = \frac{1}{2} \left(\hat{\mathbf{R}}_{\bar{x}} + \mathbf{G}_{(2N+1)} \hat{\mathbf{R}}_{\bar{x}}^* \mathbf{G}_{(2N+1)} \right), \tag{4.18}$$

where $\mathbf{G}_{(2N+1)}$ is an anti-diagonal identity matrix and $(^*)$ denotes complex conjugate entries. Alternatively, the spatially-smoothed sample covariance matrix, as in DEGEN, 2017 and MARPLE, 2019, can be estimated by

$$\hat{\mathbf{R}}_{\bar{x}_{ss}} = \frac{1}{M} \left(\mathbf{X}_{\mathrm{T}}^{\mathrm{H}} \mathbf{X}_{\mathrm{T}} \right), \tag{4.19}$$

where $\mathbf{X}_{\mathrm{T}}$ is a Toeplitz matrix constructed with the entries of each beamspace signal output $\bar{\mathbf{x}}(k)$ according to

$$\mathbf{X}_{\mathrm{T}} = \begin{bmatrix} \bar{x}_1(k) & 0 & \dots & 0 \\ \bar{x}_2(k) & \bar{x}_1(k) & \ddots & \vdots \\ \vdots & \bar{x}_2(k) & \ddots & \vdots \\ \bar{x}_M(k) & \vdots & \ddots & \bar{x}_1(k) \\ 0 & \bar{x}_M(k) & \ddots & \bar{x}_2(k) \\ \vdots & \vdots & \ddots & \vdots \\ 0 & 0 & \ddots & \bar{x}_M(k) \end{bmatrix}. \tag{4.20}$$

The spatial smoothed, reduced sample support, beamspace sample covariance matrix $\hat{\mathbf{R}}_{\bar{x}_{ss}}$ was estimated through space averaging, instead of time averaging, reducing the undesirable effects of the insufficient number of snapshots.

In the next chapter, we present thorough evaluations of the aspects of reduced spatial and temporal sampling 2-D DoA estimation, both with isolated and simultaneous limiting factors in several simulations. In the end, we consolidate our results with a simulated underwater environment.

5 EXPERIMENTAL RESULTS

This section addresses the 2-D DoA estimation of simulated and real-life underwater acoustic signals obtained from a UCA. We show the effects of limiting factors and the benefits of employing mitigating techniques. We also assess these behaviors in a simulated shallow underwater environment that includes multipath propagation (due to surface and bottom reflections) and the interaction between the non-isotropic characteristics inherent to UCA and the effects of limiting parameters MURMEL et al., 2022.

The standard parameters for both single multivariate and maritime environment simulations are: UCA with radius $R = \lambda$, two stochastic, uncorrelated narrowband sources with slight zenithal separation, SoI and Interferer, with central frequencies of 6 kHz and 7 kHz, respectively, immersed in isotropic AWGN. All results correspond to an average of 1,000 independent runs.

5.1 Simple Multivariate Evaluations

This subsection describes several UCA 2-D DoA scenarios by altering individual limiting parameters (SNR, number of sensors, and quantity of snapshots). In all simulations, the source's angular positions are: SoI with $\phi_{SoI} = 37.9°$, $\theta_{SoI} = 57.7°$, and Interferer with $\phi_{Int} = 120.5°$, $\theta_{Int} = 50.7°$.

5.1.1 Reduced Quantity of Sensors

For the case of a limited number of sensors, we defined sample support of 1,000 snapshots. The UCA has six sensors with an element spacing of 1.047λ, which results in spatial sampling below the Nyquist rate and, consequently, spatial aliasing. Regarding the beamspace transformation, it is able to map the array with only 5 phase modes ($N = 2$), again, resulting in spatial aliasing. However, as shown in Figs. 23 and 24, incorporating additional phase modes—up to 13—considerably improve the estimations. It is interesting to notice that the absolute DoA estimation error does not behave linearly with an increasing number of incorporated phase modes. In Figs. 23 and 24, we can see that incorporating 2 additional phase modes, bringing the total to 7, yields worst results than the original 5, as the beamspace mapping with 7 phase modes is less accurate, despite having additional incorporated phase modes.

According to the results in Figs. 23 and 24, the number of 11 phase modes was selected for the next simulations. The results in Figs. 25-27 depict the comparison of the estimation for the sparse UCA, mapped with only 5 phase modes and with a total of
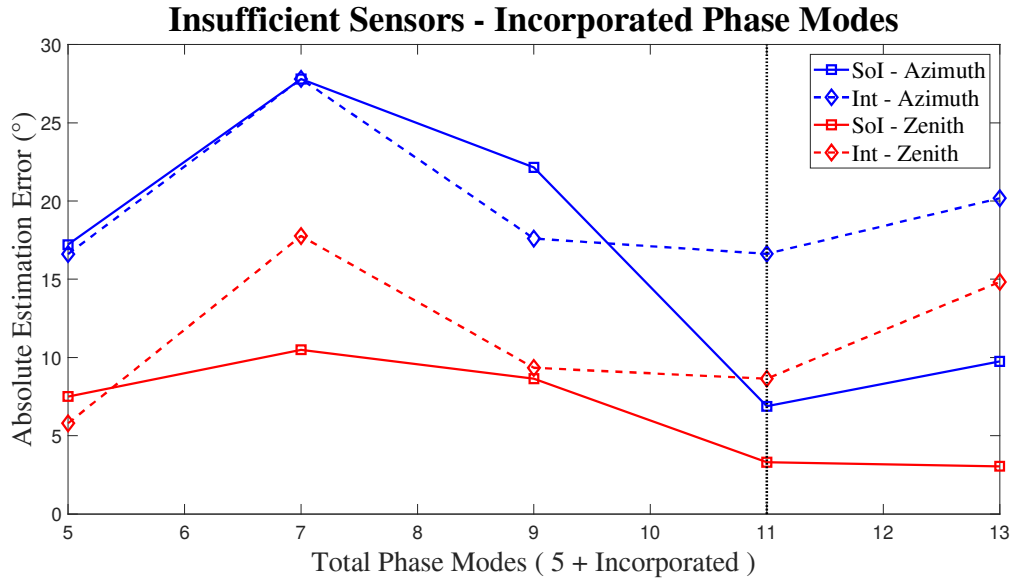
Figure 23 – Incorporated phase modes in 2-D DoA estimation. UCA having **six sensors** with spacing of 1.047λ, resolving **two** narrowband sources with angular positions $\phi_{SoI} = 37.9°$, $\theta_{SoI} = 57.7°$, $\phi_{Int} = 120.5°$ and $\theta_{Int} = 50.7°$. SIR of 3 dB and SNR of 10 dB. Sample support of 1,000 snapshots. Additional phase modes are incorporated (from an initial 5 up to a total of 13). The vertical dotted line indicates the optimum number of phase modes.

11 (5 + 6 incorporated) phase modes, as a function of the SNR, ranging from 3 dB to 15 dB. As expected, the accuracy of the estimations increases with increasing the SNR, but this effect appears to be slight for the two sources case and more prominent for the single-source case. Additionally, it is clear the expressive improvements in DoA solutions when additional phase modes are incorporated.
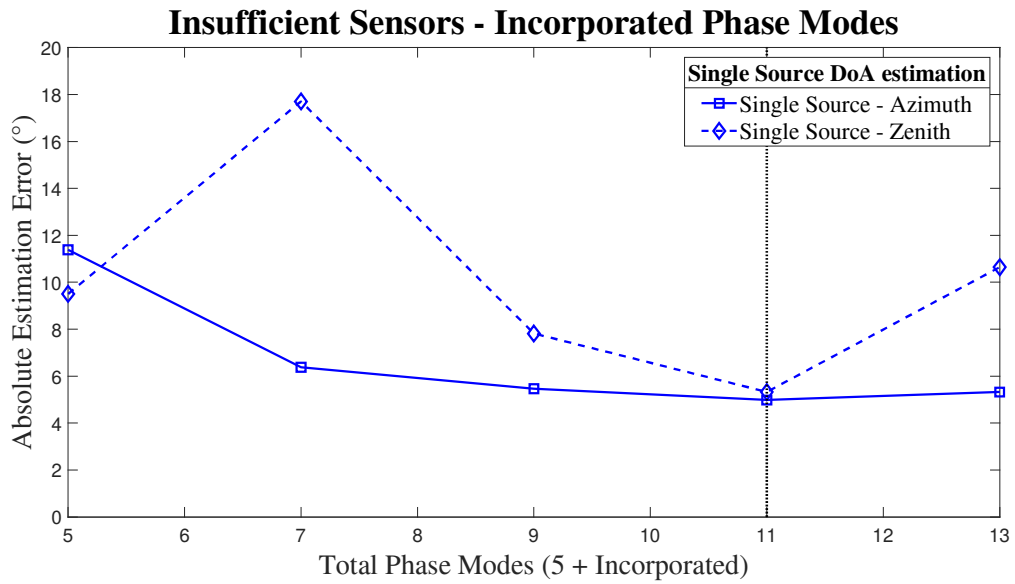
Figure 24 – Incorporated phase modes in 2-D DoA estimation. UCA having **six sensors** with spacing of 1.047λ, resolving **a single** narrowband source with angular positions $\phi_{SoI} = 37.9°$ and $\theta_{SoI} = 57.7°$. SNR of 10 dB and sample support of 1,000 snapshots. Additional phase modes are incorporated (from an initial 5 up to a total of 13). The vertical dotted line indicates the optimum number of phase modes.
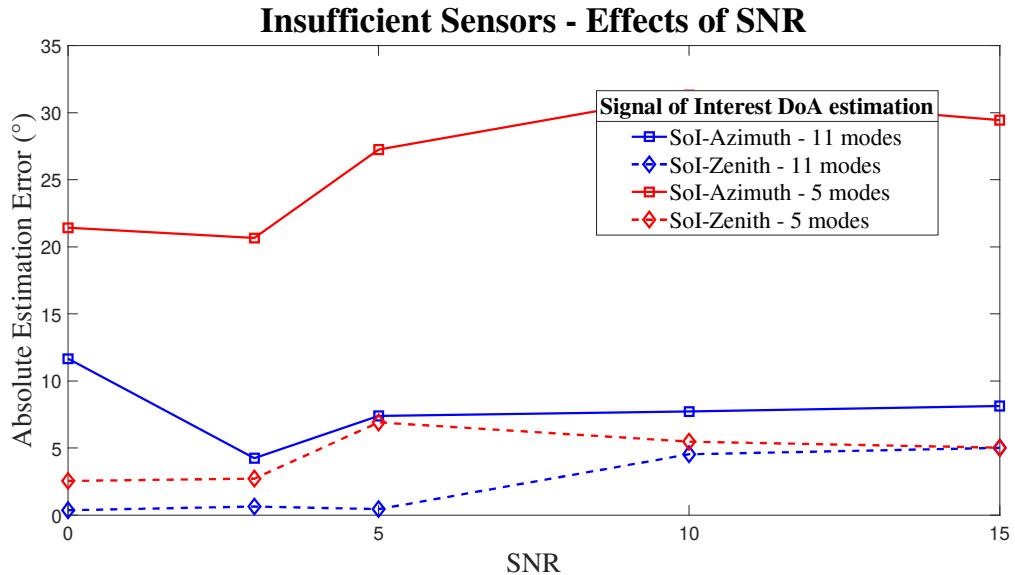
Figure 25 – Absolute 2-D DoA estimation error of the **SoI** source. UCA having **six sensors** with spacing of 1.047λ, resolving **two** narrowband sources with angular positions $\phi_{SoI} = 37.9°$, $\theta_{SoI} = 57.7°$, $\phi_{Int} = 120.5°$ and $\theta_{Int} = 50.7°$. SIR of 3 dB and SNR of 10 dB. Sample support of 1,000 snapshots. UCA mapped in beamspace with 5 and 11 (5+6 incorporated) phase modes.
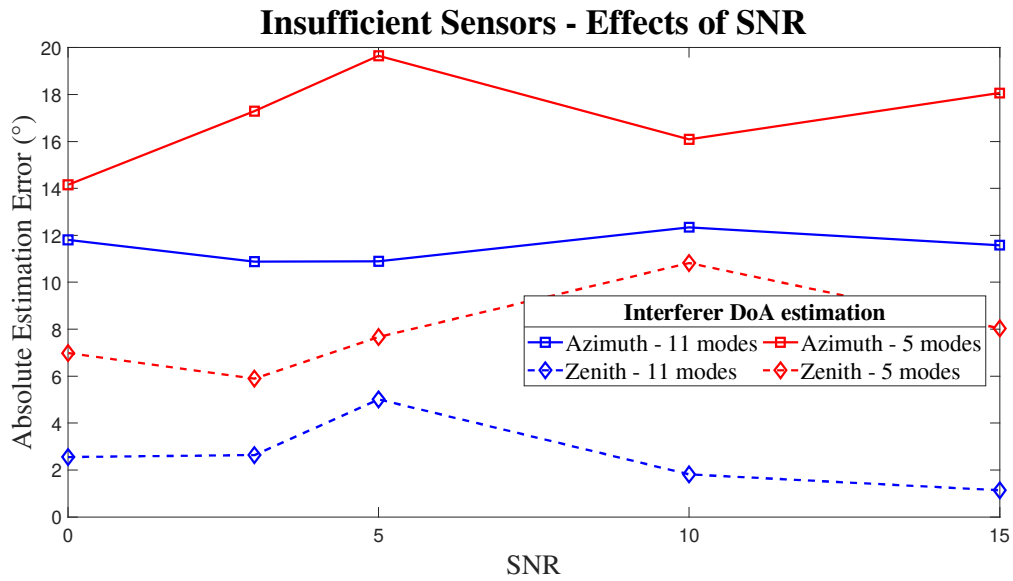
Figure 26 – Absolute 2-D DoA estimation error of the **Interferer** source. UCA having **six sensors** with spacing of 1.047λ, resolving **two** narrowband sources with angular positions $\phi_{SoI} = 37.9°$, $\theta_{SoI} = 57.7°$, $\phi_{Int} = 120.5°$ and $\theta_{Int} = 50.7°$. SIR of 3 dB and SNR of 10 dB. Sample support of 1,000 snapshots. UCA mapped in beamspace with 5 and 11 (5+6 incorporated) phase modes.
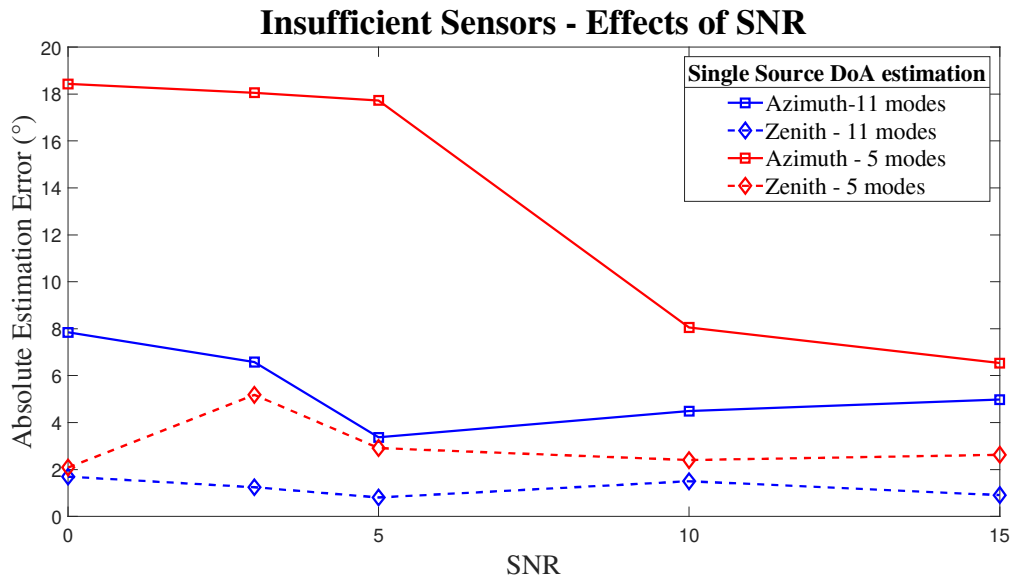
Figure 27 – Absolute 2-D DoA estimation error of a **single source**. UCA having **six sensors** with spacing of 1.047λ, resolving **two** narrowband sources with angular positions $\phi_{SoI} = 37.9°$, $\theta_{SoI} = 57.7°$, $\phi_{Int} = 120.5°$ and $\theta_{Int} = 50.7°$. SIR of 3 dB and SNR of 10 dB. Sample support of 1,000 snapshots. UCA mapped in beamspace with 5 and 11 (5+6 incorporated) phase modes.

5.1.2 Small Sample Support

For the case of small sample support, the UCA has 16 sensors, mapped in beamspace by 11 phase modes ($N = 5$) and with element spacing of 0.393λ. Sample support ranges from 1,000 down to a single snapshot. Figs. 28-33 depicts the influence of decreasing sample support, where the plots with SSS indicate the use of small sample support mitigation (utilizing Toeplitz Conditioning and Leakage Minimization with $\mu = 0.9$.) for two and a single source cases and with individual results for both sources (Signal of Interest and Interferer).

We can observe that the absolute error increases with the reduction of snapshots for both SSS and non-SSS solutions. As seen in Figs. 28-33, small sample support techniques can improve solutions and even extend the lower limits of sample support where both DoAs can be accurately estimated. Additionally, we can see that the results obtained in single source DoA estimation are better and less affected by the reduction in sample support.

Subspace leakage results in an unclear definition of signal and noise eigenvectors and difficulties to sort signal eigenvectors by magnitude. Leakage Minimization addresses this problem and is dependent of the factor μ in order to estimate and reduce cross-correlation components, mitigating subspace leakage. In Figs. 34-36 we can see the effects of the factor μ in the mitigation of small sample support problem and the selection of the value utilized in previous results. Note how the μ factor has a larger effect in the Interferer DoA estimation. With sufficient sample support, the SoI is satisfactorily resolved independent of μ. For small sample support, leakage minimization improves both SoI and Interferer solutions.
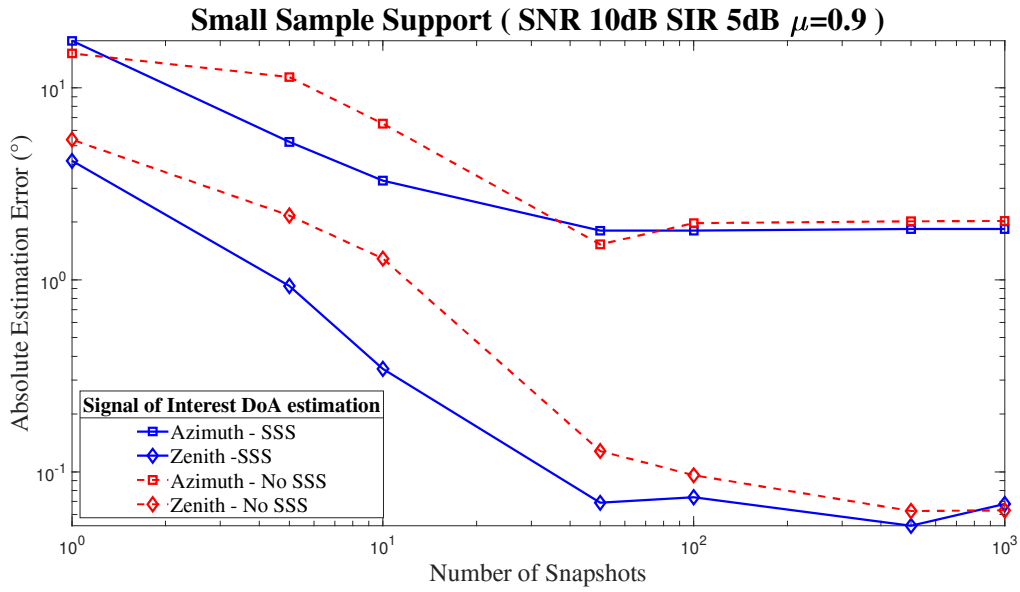
Figure 28 – Decreasing sample support in UCA 2-D DoA estimation. Depicting **SoI** source estimation errors as a function of the number of snapshots, both in the presence (SSS) and absence (no SSS) of small sample support mitigation. UCA with 16 sensors mapped by 11 phase modes. Resolving **two** narrowband sources with angular positions $\phi_{SoI} = 37.9°$, $\theta_{SoI} = 57.7°$, $\phi_{Int} = 120.5°$ and $\theta_{Int} = 50.7°$. **SIR of 5 dB and SNR of 10 dB**. μ of 0.9.
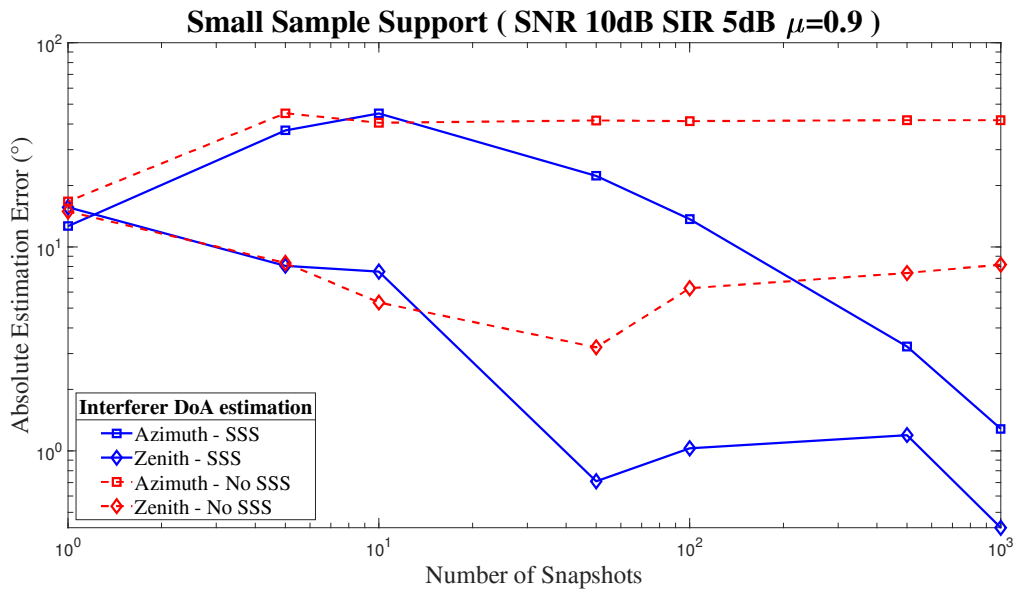
Figure 29 – Decreasing sample support in UCA 2-D DoA estimation. Depicting **Interferer** source estimation errors as a function of the number of snapshots, both in the presence (SSS) and absence (no SSS) of small sample support mitigation. UCA with 16 sensors mapped by 11 phase modes. Resolving **two** narrowband sources with angular positions $\phi_{SoI} = 37.9°$, $\theta_{SoI} = 57.7°$, $\phi_{Int} = 120.5°$ and $\theta_{Int} = 50.7°$. **SIR of 5 dB and SNR of 10 dB**. μ of 0.9.
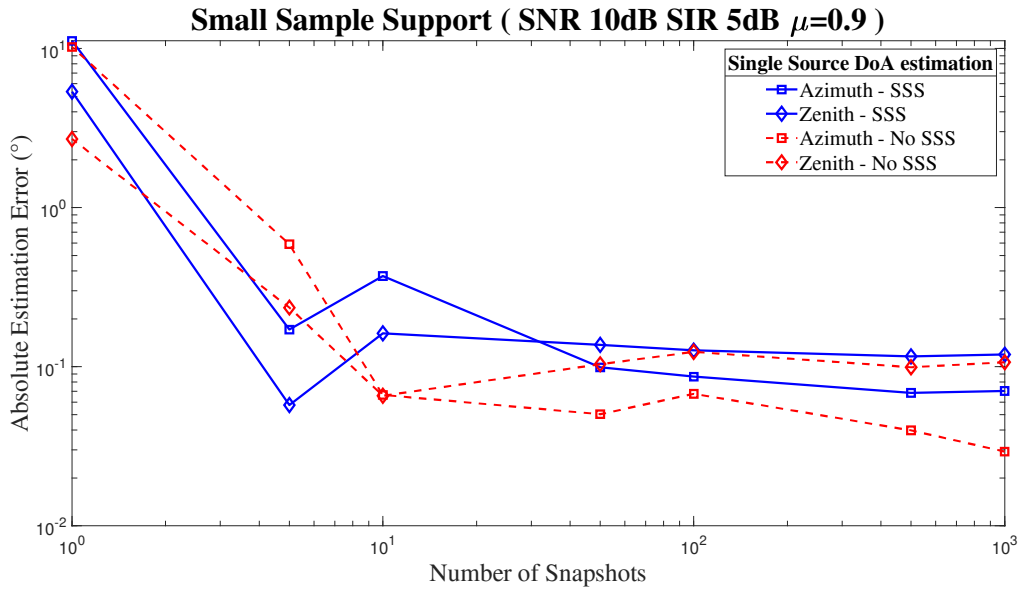
Figure 30 – Decreasing sample support in UCA 2-D DoA estimation. Depicting **single** source estimation errors as a function of the number of snapshots, both in the presence (SSS) and absence (no SSS) of small sample support mitigation. UCA with 16 sensors mapped by 11 phase modes. Narrowband source with angular positions $\phi_{SoI} = 37.9°$, $\theta_{SoI} = 57.7°$. **SIR of 5 dB and SNR of 10 dB**. μ of 0.9.
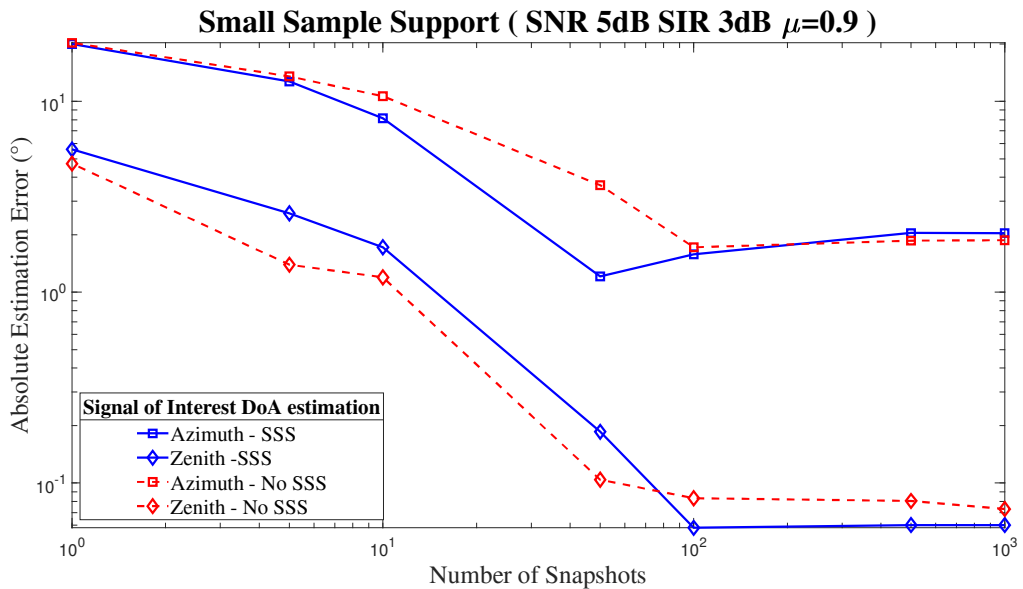
Figure 31 – Decreasing sample support in UCA 2-D DoA estimation. Depicting **SoI** source estimation errors as a function of the number of snapshots, both in the presence (SSS) and absence (no SSS) of small sample support mitigation. UCA with 16 sensors mapped by 11 phase modes. Resolving **two** narrowband sources with angular positions $\phi_{SoI} = 37.9°$, $\theta_{SoI} = 57.7°$, $\phi_{Int} = 120.5°$ and $\theta_{Int} = 50.7°$. **SIR of 3 dB and SNR of 5 dB**. μ of 0.9.
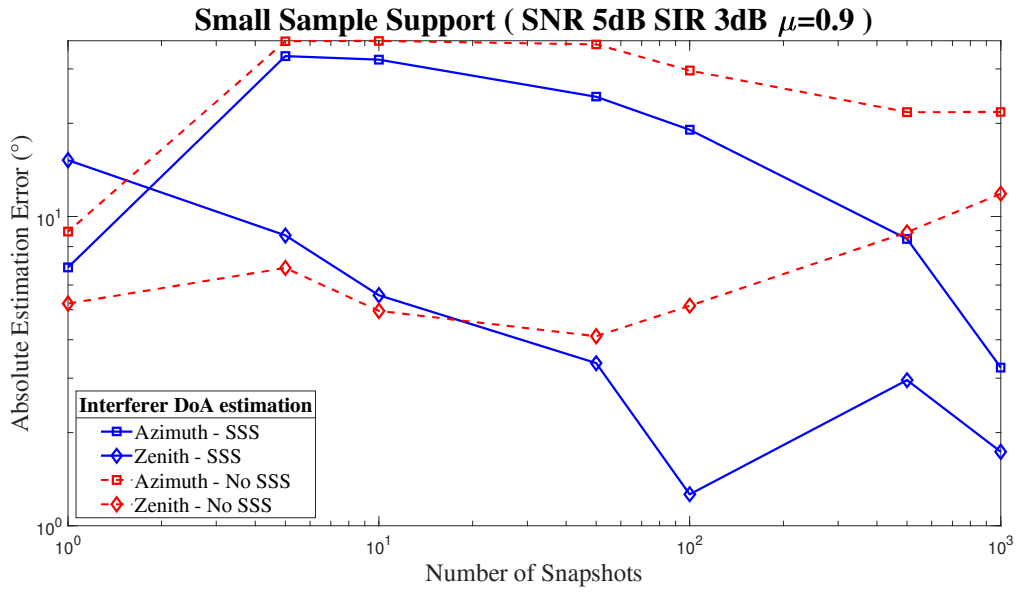
Figure 32 – Decreasing sample support in UCA 2-D DoA estimation. Depicting **Interferer** source estimation errors as a function of the number of snapshots, both in the presence (SSS) and absence (no SSS) of small sample support mitigation. UCA with 16 sensors mapped by 11 phase modes. Resolving **two** narrowband sources with angular positions $\phi_{SoI} = 37.9°$, $\theta_{SoI} = 57.7°$, $\phi_{Int} = 120.5°$ and $\theta_{Int} = 50.7°$.**SIR of 3 dB and SNR of 5 dB**. μ of 0.9.
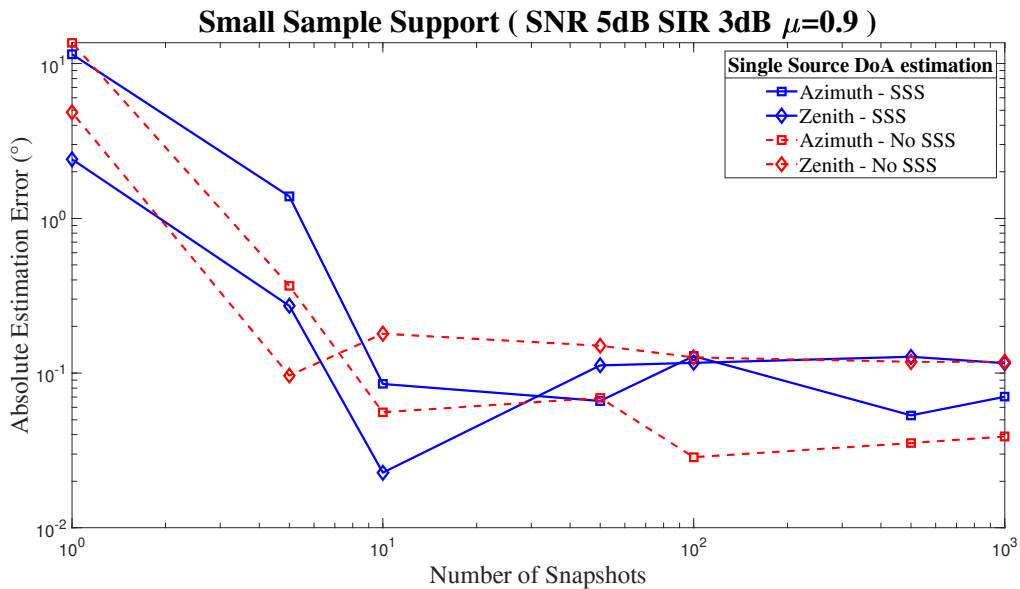
Figure 33 – Decreasing sample support in UCA 2-D DoA estimation. Depicting **single** source estimation errors as a function of the number of snapshots, both in the presence (SSS) and absence (no SSS) of small sample support mitigation. UCA with 16 sensors mapped by 11 phase modes. Narrowband source with angular positions $\phi_{SoI} = 37.9°$, $\theta_{SoI} = 57.7°$. **SIR of 3 dB and SNR of 5 dB**. μ of 0.9.
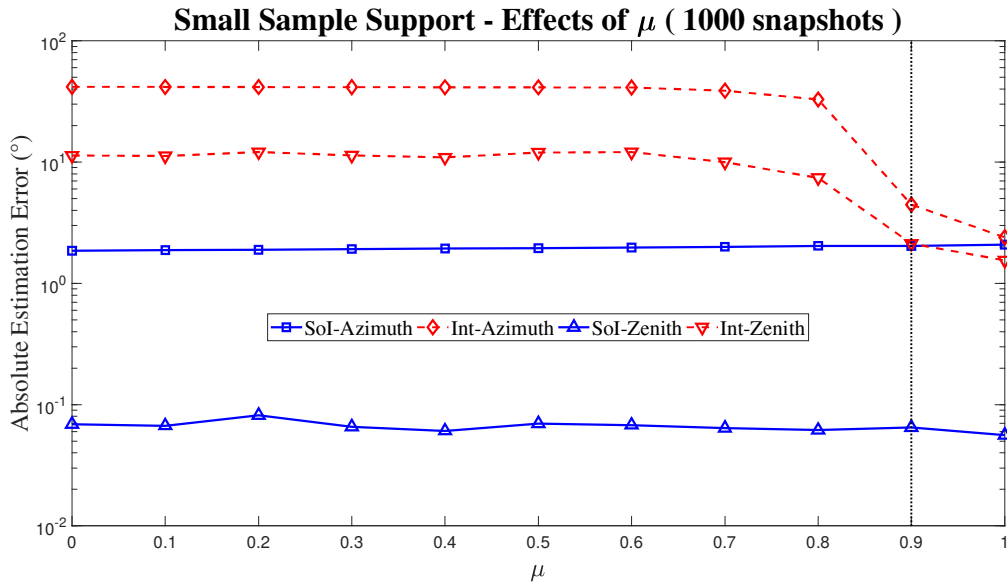
Figure 34 – Effects of factor μ in small sample support UCA 2-D DoA estimation. 16 sensor UCA mapped in beamspace by 11 phase modes. Resolving two narrowband sources with angular positions $\phi_{SoI} = 37.9°$, $\theta_{SoI} = 57.7°$, $\phi_{Int} = 120.5°$ and $\theta_{Int} = 50.7°$. SNR 10 dB and SIR 3 dB. Sample support **1,000 snapshots**.
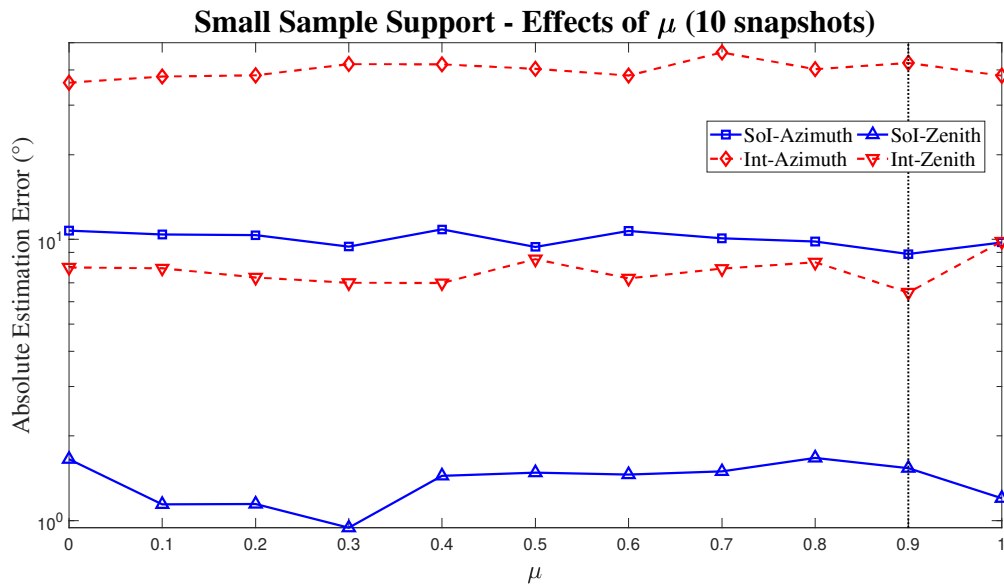
Figure 35 – Effects of factor μ in small sample support UCA 2-D DoA estimation. 16 sensor UCA mapped in beamspace by 11 phase modes. Resolving two narrowband sources with angular positions $\phi_{SoI} = 37.9°$, $\theta_{SoI} = 57.7°$, $\phi_{Int} = 120.5°$ and $\theta_{Int} = 50.7°$. SNR 10 dB and SIR 3 dB. Small sample support of **10 snapshots**.
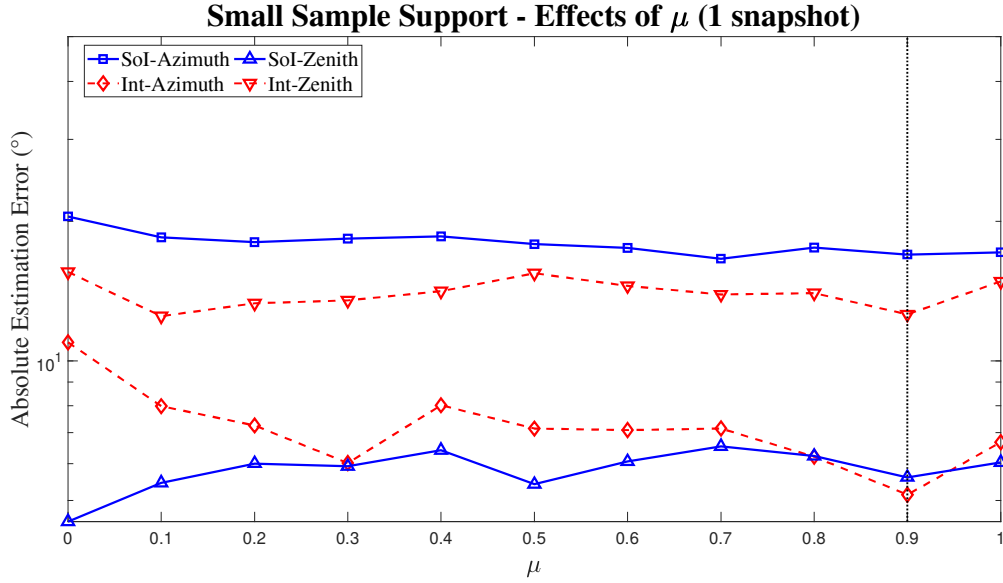
Figure 36 – Effects of factor μ in small sample support UCA 2-D DoA estimation. 16 sensor UCA mapped in beamspace by 11 phase modes. Resolving two narrowband sources with angular positions $\phi_{SoI} = 37.9°$, $\theta_{SoI} = 57.7°$, $\phi_{Int} = 120.5°$ and $\theta_{Int} = 50.7°$. SNR 10 dB and SIR 3 dB. Small sample support of a **single snapshot**.

5.2   Simultaneous Spatial And Temporal Evaluations

In this section, we address the problems of reduced spatial and temporal sampling simultaneously. Employing combined phase mode incorporation and Leakage Minimization techniques, we evaluate their joint behavior similarly to the isolated multivariate simulations. Toeplitz Conditioning was not applied due to the particular form of each entry of the beamspace array manifold with incorporated phase modes, each expressed by more than one phase mode. In this manner, the disassociation of azimuth and zenith-dependent portions of the array manifold is not readily possible.

The specific parameters for these simulations are: an ensemble of 1.000 independent runs, sources with a SIR of 3 dB, and AWGN with an SNR of 10 dB. Six sensors UCA mapped in beamspace by 5, and up to 13, phase modes. Leakage Minimization μ factor of 0.8 and sample support ranging from 1.000 to 5 snapshots. Angular positions are the same as in Section 5.1.

Starting with a more detailed analysis of the number of phase modes for beamspace mapping, we show the effects of incorporating phase modes to a small sample support 2-D DoA estimation, both in the presence and absence of Leakage Minimization. Figs. 37 and 38 depict increasing incorporated phase modes solution errors for estimations with only 10 snapshots.
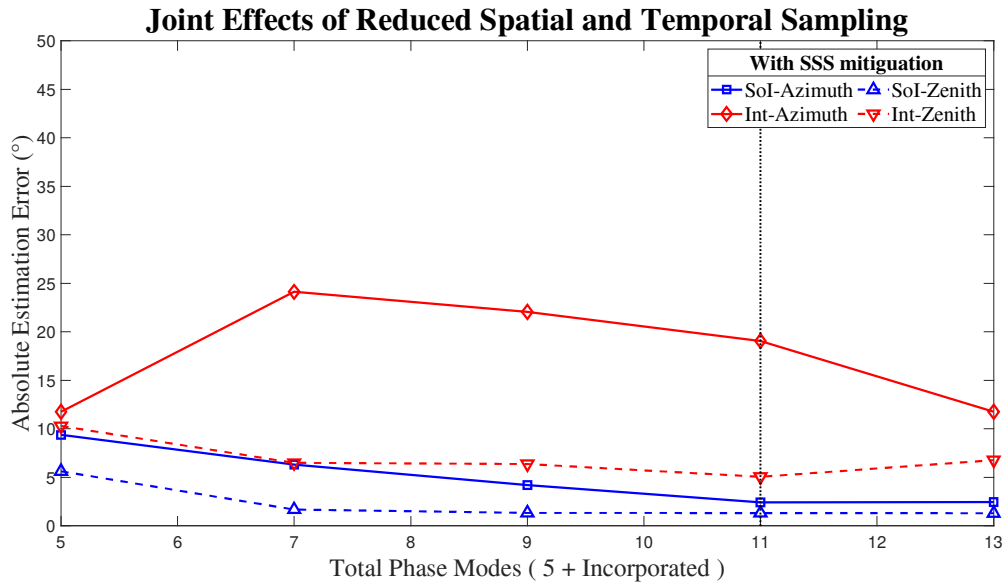
Figure 37 – Combined effects of incorporating phase modes in small sample support 2-D DoA estimation **employing Leakage Minimization** (SSS). UCA having **six sensors** with spacing of 1.047λ, resolving **two** narrowband sources with angular positions $\phi_{SoI} = 37.9°$, $\theta_{SoI} = 57.7°$, $\phi_{Int} = 120.5°$ and $\theta_{Int} = 50.7°$. SIR of 3 dB, SNR of 10 dB and small sample support of **10 snapshots**. Additional **phase modes are incorporated** (from an initial 5 up to a total of 13).
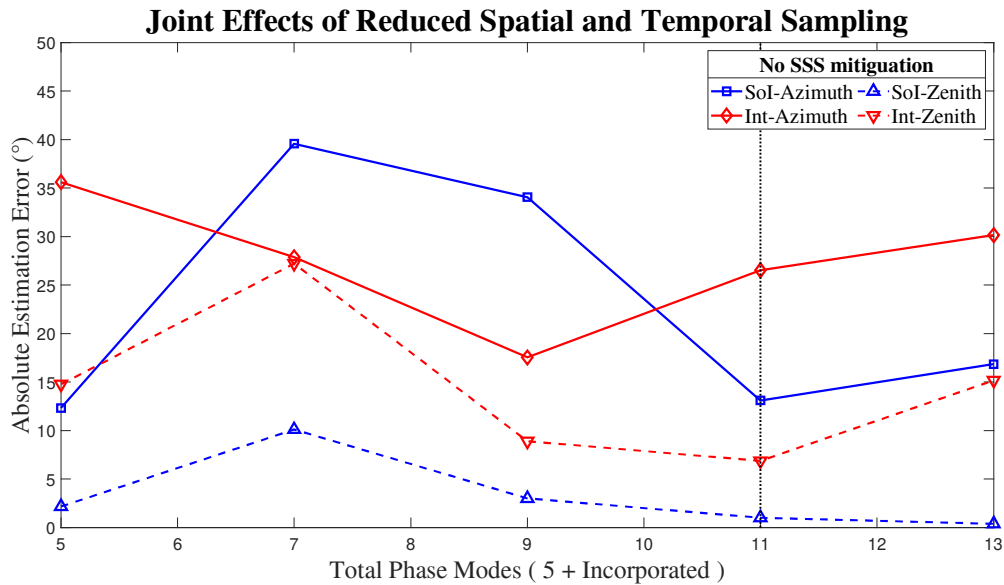
Figure 38 – Combined effects of incorporating phase modes in small sample support 2-D DoA estimation **without Leakage Minimization** (no SSS). UCA having **six sensors** with spacing of 1.047λ, resolving **two** narrowband sources with angular positions $\phi_{SoI} = 37.9°$, $\theta_{SoI} = 57.7°$, $\phi_{Int} = 120.5°$ and $\theta_{Int} = 50.7°$. SIR of 3 dB, SNR of 10 dB and small sample support of **10 snapshots**. Additional **phase modes are incorporated** (from an initial 5 up to a total of 13).

Continuing, with a greater focus on small sample support, Figs. 39-42 depict the combined behavior of beamspace mapping, by 5 and 11 phase modes, and Leakage Minimization for decreasing sample support. The optimum value of additional phase modes utilized in these simulations was obtained by the results of Figs. 37 and 38.
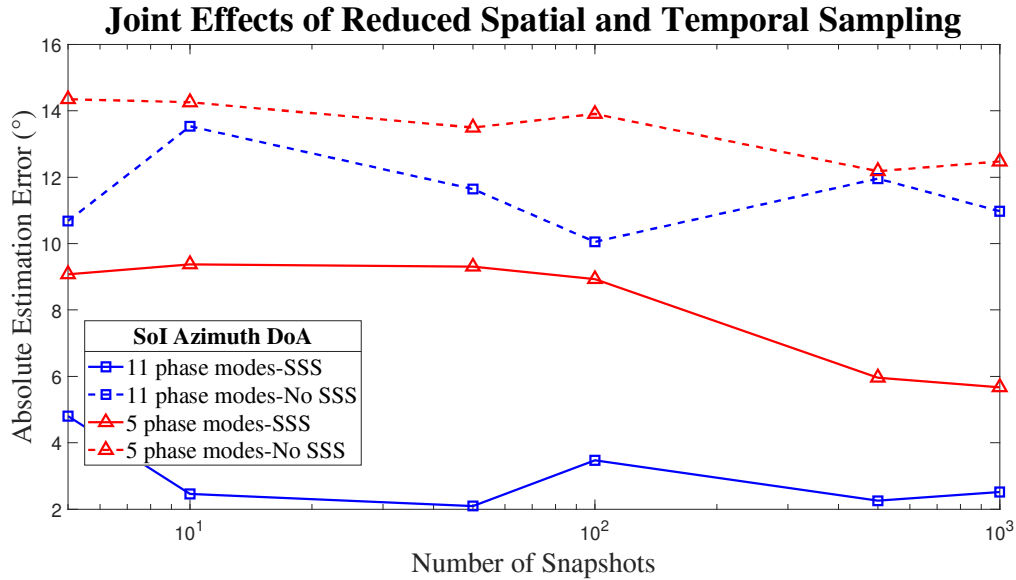
Figure 39 – Combined behavior of beamspace mapping and Leakage Minimization with decreasing sample support for **SoI azimuth DoA**. UCA having **six sensors** with a spacing of 1.047λ and beamspace mapping with 5 and 11 (5+6 incorporated) phase modes. Resolving **two** narrowband sources with angular positions $\phi_{SoI} = 37.9°$, $\theta_{SoI} = 57.7°$, $\phi_{Int} = 120.5°$ and $\theta_{Int} = 50.7°$. SIR of 3 dB and SNR of 10 dB.

The combined results tend to behave similarly to the individual mitigating techniques results in Section 5.1, where additional phase modes yield better results in spatially aliased solutions and minimized leakage solutions yield better results than small sample support solutions. This predictable behavior is depicted in Figs. 39 and 40.

However, we can observe that, for the combined limiting factors scenario, leakage minimization contributions for the overall improvements are somewhat more pronounced, especially for the Interferer DoA solutions. This behavior can be seen in Figs. 41 and 42, where the spatially aliased, minimized leakage solutions can be better than solutions with incorporated phase modes but without leakage minimization. These observations also point to mutual interference of the two mitigating techniques (phase modes incorporation and leakage minimization), as these techniques are based on different principles to improve DoA estimation.
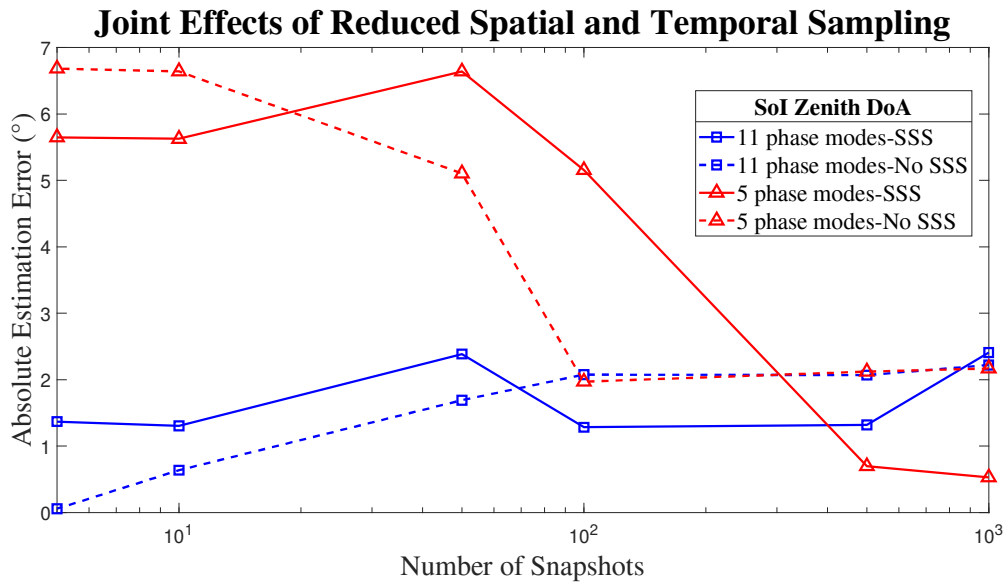
Figure 40 – Combined behavior of beamspace mapping and Leakage Minimization with decreasing sample support for **SoI zenith DoA**. UCA having **six sensors** with a spacing of 1.047λ and beamspace mapping with 5 and 11 (5+6 incorporated) phase modes. Resolving **two** narrowband sources with angular positions $\phi_{SoI} = 37.9°$, $\theta_{SoI} = 57.7°$, $\phi_{Int} = 120.5°$ and $\theta_{Int} = 50.7°$. SIR of 3 dB and SNR of 10 dB.
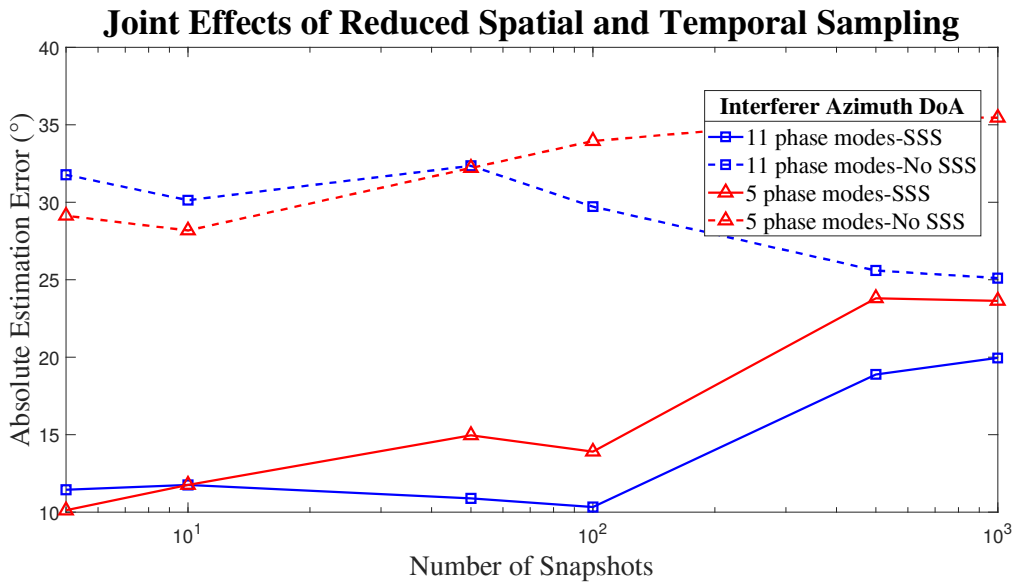
Figure 41 – Combined behavior of beamspace mapping and Leakage Minimization with decreasing sample support for **Interferer azimuth DoA**. UCA having **six sensors** with a spacing of 1.047λ and beamspace mapping with 5 and 11 (5+6 incorporated) phase modes. Resolving **two** narrowband sources with angular positions $\phi_{SoI} = 37.9°$, $\theta_{SoI} = 57.7°$, $\phi_{Int} = 120.5°$ and $\theta_{Int} = 50.7°$. SIR of 3 dB and SNR of 10 dB.

Joint Effects of Reduced Spatial and Temporal Sampling
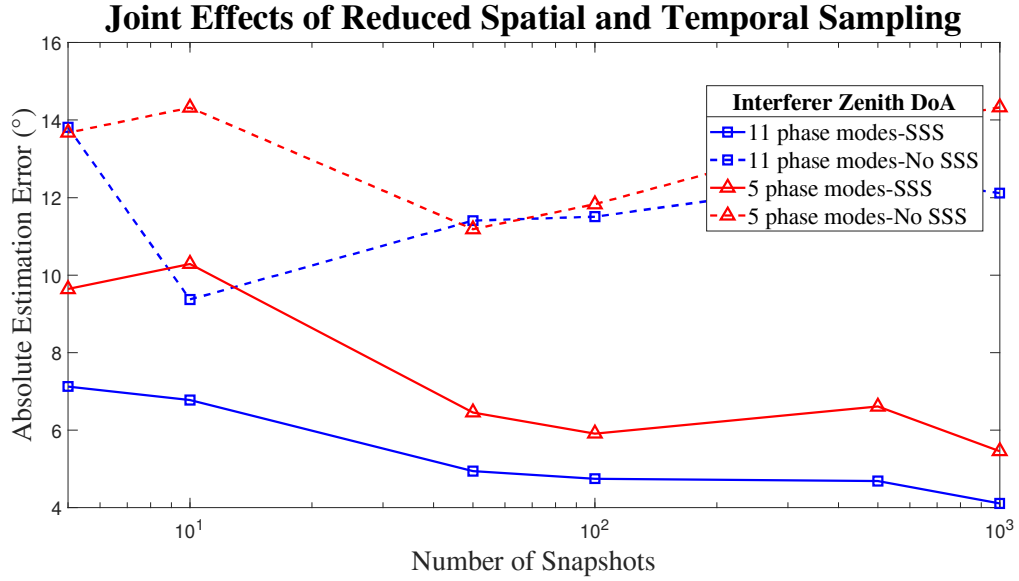
Figure 42 – Combined behavior of beamspace mapping and Leakage Minimization with decreasing sample support for **Interferer zenith DoA**. UCA having **six sensors** with spacing of 1.047λ and beamspace mapping with 5 and 11 (5+6 incorporated) phase modes. Resolving **two** narrowband sources with angular positions $\phi_{SoI} = 37.9°$, $\theta_{SoI} = 57.7°$, $\phi_{Int} = 120.5°$ and $\theta_{Int} = 50.7°$. SIR of 3 dB and SNR of 10 dB.

5.3 Underwater Environment Simulation

This subsection employs the methods described herein in conditions similar to a real shallow underwater scenario. We utilize real-life signals from the ShipsEar database, available in <http://atlanttic.uvigo.es/underwaternoise/>. We assume two uncorrelated surface sources, namely a cruise ship and a motorboat, immersed in isotropic AWGN with SNR of 15dB and simulate the effects of surface and bottom reflections, resulting in multipath propagation.

This propagation phenomenon was simulated by adding two others sources to our incoming signal, each one representing a surface reflection of the direct path sources. Different time shifts were applied to each original direct path signal, accounting for different propagation paths. These time-shifted signals were used as spurious sources, resulting from multipath propagation. The angular positions of said spurious multipath sources were set with a substantially different zenithal angle, again, for representation of surface reflection and, on top of that, a slight variation in azimuthal angle, simulating possible horizontal refraction. By this approach, we manage to simulate two pairs of sources, representing direct path and multipath propagation of both SoI (cruise ship) and Interferer (motorboat), all based in real-life signals.

The submerged UCA has 32 sensors mapped by 15 phase modes ($N = 7$) and $R = \lambda$. It receives direct and reflected planewaves from both sources, with a central frequency

set to 1 kHz. Both small sample support techniques (Toeplitz conditioning and leakage minimization) are used and factor μ was set to 0.8, based on the results depicted in Fig. 45. The angular position of the two uncorrelated sources are: cruise ship (SoI) $\phi_{CS} = 23.1°$, $\theta_{CS} = 48.5°$ and motorboat (Interferer) with $\phi_{MB} = 142°$, $\theta_{MB} = 34.7°$. Sources with SIR of 5 dB and immerse in AWGN with SNR 15 dB. Their respective multipath spurious signals are hitting the array from $\phi_{CSmulti} = 26°$, $\theta_{CSmulti} = 19.3°$, and $\phi_{MBmulti} = 143.9°$, $\theta_{MBmulti} = 11.5°$. These spurious multipath DoAs represent surface reflections and slight azimuthal refraction. Spurious multipath sources have an attenuation of 15 dB.
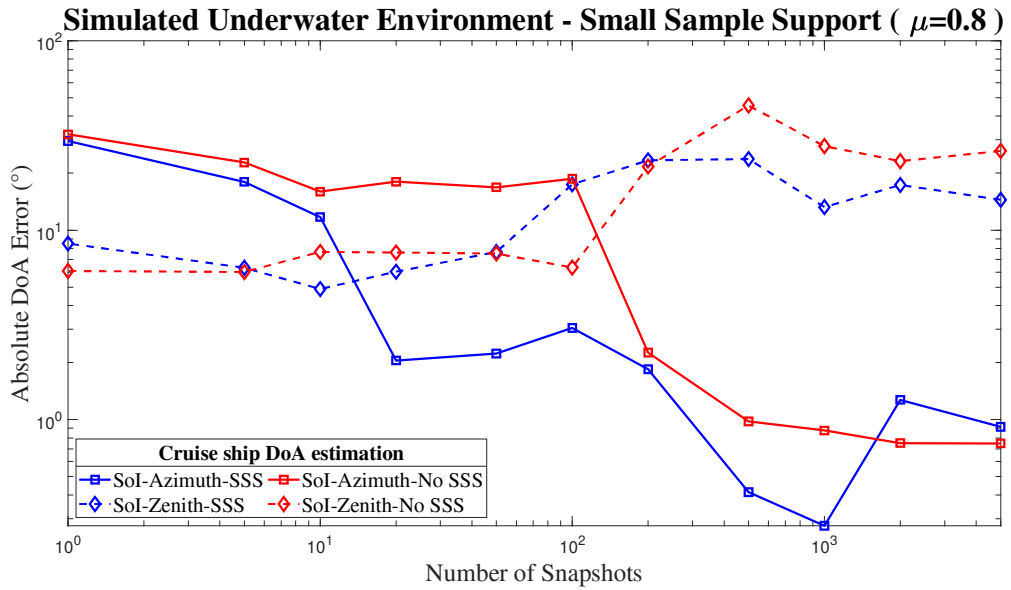
Figure 43 – Decreasing sample support in simulated underwater 2-D DoA estimation. 32 sensor UCA mapped by 15 phase modes. Resolving two narrowband sources (real signals) with angular positions $\phi_{CS} = 23.1°$, $\theta_{CS} = 48.5°$, $\phi_{MB} = 142°$ and $\theta_{MB} = 34.7°$ with multipath propagation. Depicting the **Cruise ship (SoI)** DoA estimation errors in function of sample support. SNR 15 dB, SIR 5 dB, and multipath attenuation of 15 dB.

In this work, we did not address directly the problem of correlated signals arising from direct and multipath propagation of the planewave from a particular source, as it is not the scope of his work. Despite this unattended issue, results depicted in Figs. 43 and 44 show that the small sample support techniques, indicated by the suffix SSS in the legend, produced improved results, mainly in Root-MUSIC azimuth estimation, when compared with results in the absence of the mitigating techniques. Also, using a single value of μ for a wide range of sample support may have different and even contradictory effects. In our experiments, while utilizing leakage minimization with a particular μ factor value may work well for smaller sample support, it can present small or negligible improvements for larger sample support.
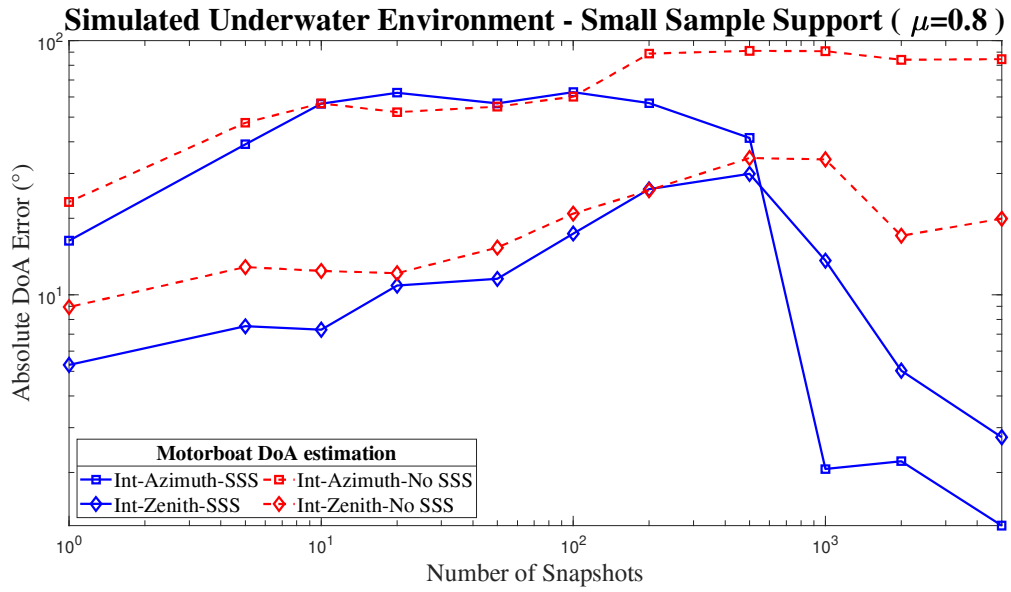
Figure 44 – Decreasing sample support in simulated underwater 2-D DoA estimation. 32 sensor UCA mapped by 15 phase modes. Resolving two narrowband sources (real signals) with angular positions $\phi_{CS} = 23.1°$, $\theta_{CS} = 48.5°$, $\phi_{MB} = 142°$ and $\theta_{MB} = 34.7°$ with multipath propagation. Depicting the **Motorboat (Interferer)** DoA estimation errors in function of sample support. SNR 15 dB, SIR 5 dB, and multipath attenuation of 15 dB.
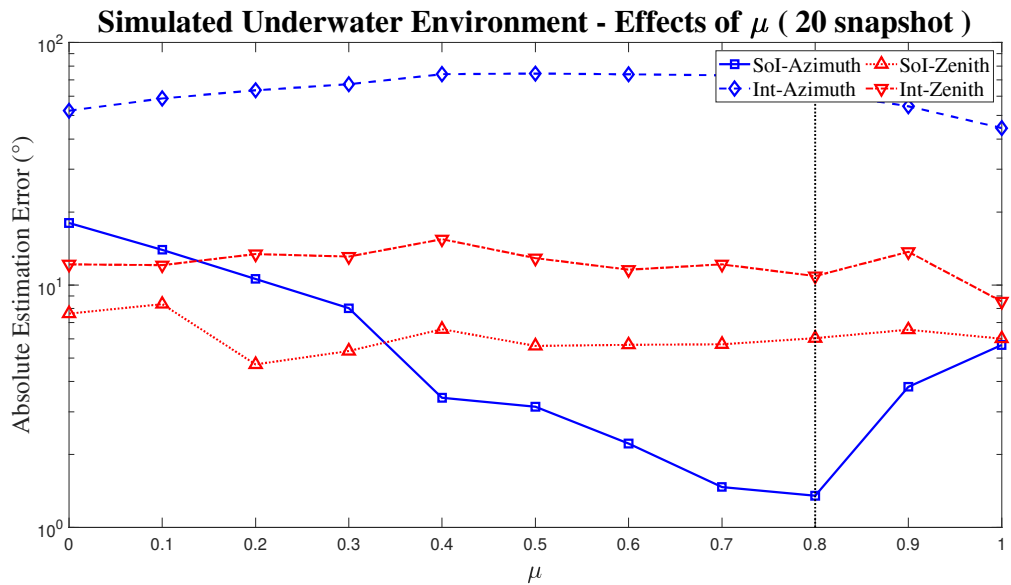
Figure 45 – Effects of factor μ in simulated underwater 2-D DoA estimation and small sample support. Resolving two narrowband sources (real signals) with angular positions $\phi_{CS} = 23.1°$, $\theta_{CS} = 48.5°$, $\phi_{MB} = 142°$ and $\theta_{MB} = 34.7°$ with multipath propagation. Small sample support of **20 snapshots**, SNR 15 dB, SIR 5 dB, and multipath propagation attenuation of 15 dB.

6 CONCLUSION

Uniform Circular Array is an important geometry for planar arrays with some unique characteristics that result in a very particular signal model and array manifold vector, not suited for all classical array signal processing methods and optimization techniques. This problem can be circumvented, up to a substantial degree, by beamspace mapping via Fourier analysis of the excitation function (or the receiving signal along the circular aperture).

The approach to 2-D DoA estimation explored herein employs two versions of the MUSIC algorithm, each behaving differently in the presence of limiting parameters and responding also differently to the combined application of mitigation techniques. Most of the methods presented are directed to beamspace Root-MUSIC approach and, consequently, present greater improvements when mitigation techniques are applied.

Mitigation techniques addressed herein were used with correlated signals produced by direct and multipath propagation of planewaves from each source. Although not within the scope of this work, when applied to correlated sources in reduced spatial or temporal input data situations, we obtained favorable results, not suffering greatly from the correlation between direct and multipath propagation signals.

We see in this work that reduced spatial sampling and inaccurate beamspace mapping effects can be satisfactorily mitigated by incorporating additional phase modes. Incorporating a number of additional phase modes, up to an optimum value determined by the criteria of Eq. (3.25), improves considerably the accuracy of the DoA estimation. In our simulations, we found empirically that the optimum beamspace mapping was through 11 phase modes, as shown in Figs. 23-24.

In Figs. 25-27, we can observe more clearly the improvements in DoA accuracy due to phase modes incorporation when compared with spatially-aliased solutions. Also, the effects of incorporation of phase modes are more visible for the azimuth parameter, which is estimated via Root-MUSIC, while the zenithal DoA, estimated by 1-D Spectral MUSIC search seems to be more resistant to spatial aliasing.

Regarding the effects of SNR in spatially aliased DoA estimations, we observed that azimuth DoA is more responsive to increasing SNR. Azimuth DoA is estimated via beamspace Root-MUSIC and, by the incorporation of additional phase modes, the better array description leads to better estimations. Zenithal DoA, estimated via Spectral MUSIC, is less susceptible to SNR.

For the Small Sample Support limitation, we aim to access the conditioning of the sample covariance matrix. Due to reduced input data, the sample covariance matrix

deviates considerably from the statistical covariance matrix provided by the array signal model due to subspace leakage.

The subspace division of a signal covariance matrix is carried out based on sorting the eigenvalues and respective eigenvectors. Signal subspace eigenvectors should have conspicuous values and each source is related to a signal eigenvector. With small sample support, the eigenvalues are much closer together and an eigenvalue corresponding to a noise eigenvector can be larger than the eigenvalue of a signal eigenvector, leading to an intersection between subspaces. Subspace leakage can also happen in low SNR situations where, again, eigenvalues tend to be close due to difficulties in separating signal sources from background noise.

We observed that matrix conditioning could mitigate biased covariance matrices, allowing even a single snapshot DoA estimation. We utilized $\mu = 0.9$ as the optimum value for our simulations of Toeplitz Conditioning and Leakage Minimization. This high value corroborates our good estimation of cross-correlation components and their minimization in the first iteration. However, factor μ presents an additional complexity and, as a predetermined value calculated for small sample support, can yield disappointing results for larger amounts of temporal data; this is shown in the larger sample support regions of Figs. 30, 31 and 33.

Assessing simultaneous reduced temporal and spatial sampling, Toeplitz Conditioning cannot be used concomitantly with sparse UCA due to the need to express the phase mode of the entries of the beamspace array manifold as a single Bessel function and complex exponential in order to dissociate azimuth and zenith-dependent portions of the beampace array manifold. In a sparse UCA, in order to incorporate additional phase modes, each one is expressed by more than one Bessel function and complex exponential, so Toeplitz Conditioning cannot be readily applied.

In Figs. 37-41 we conclude that the joint behavior of incorporating phase modes and Leakage Minimization follows partially the behaviours of isolated mitigating techniques. Leakage Minimization presents more pronounced effects on overall behavior than incorporating phase modes. Fig. 41 suggests mutual adverse effects between the two mitigating techniques, where 2-D DoA absolute error behavior with simultaneous mitigating techniques diverges from the isolated techniques.

In the underwater environment simulation, the effects of multipath propagation, akin to correlated sources, are present. Although not addressed directly, Toeplitz Conditioning and Leakage Minimization end up yielding favorable results in this additionally limiting condition, on top of small sample support.

We show in Figs. 43 and 44 the improved results in 2-D DoA estimating when applying Small Sample Support mitigation techniques. For its good results, the 20 snapshots

sample support was utilized to evaluate the effects of factor μ. The criterion for optimum value was the SoI azimuth DoA ϕ_{cs}. Fig. 45 depicts that $\mu = 0.8$ yields the best results for our criterion. Also, this high value of μ shows that our Leakage Minimization process was successful, as cross-correlation terms were precisely estimated. Low values of μ would indicate poor cross-correlation estimation and the necessity of additional iterations of the Leakage Minimization process.

6.1 Suggestions for Future Works

The suggested continuity for this work is to extend the knowledge and results beyond DoA estimation with uniform circular arrays, maintaining the limiting factors of a reduced number of sensors and small sample support. Our future studies would comprehend three consecutive initiatives. Initially, we intend to evaluate the use of phase modes-based beamspace transform with suitable volumetric array geometries including cylindrical arrays, to improve zenith DoA estimation, and spherical arrays, aiming at obtaining isotropic 2-D DoA. The next initiative would be the extension of beamspace 2-D DoA with a reduced number of sensors and small sample support mitigating techniques to volumetric arrays. Finally, we would be able to address the application of beamspace 2-D DoA in passive ranging estimation with a multistatic arrangement via Vertical Direct Passive Ranging (VDPR) and Horizontal Direct Passive Ranging (HDPR) WAITE, 2002; MARAGE; MORI, 2013 under reduced spatial and temporal sampling.

The circular symmetry in cylindrical and spherical arrays should allow beamspace transform for 1-D or 2-D DoA estimation with improved zenithal resolution when compared with UCA. With a satisfactory volumetric phase modes transform, it should be possible to extend reduced spatial and temporal sampling beamspace techniques to these array geometries. Regarding passive ranging, HDPR is a well-known geometric method of passive ranging for submarine sonars. As HDPR relies only on azimuth DoAs, our work on UCA under reduced sampling can be readily applied. VDPR, however, utilizes only zenith DoAs, so a volumetric array should be preferable, as it should have a better zenithal resolution. VDPR also relies on multipath propagation, so the indirect favorable effects of leakage minimization on correlated sources should be beneficial for passive ranging.

BIBLIOGRAPHY

TREES, H. V. *Optimum Array Processing*. 2. ed. 605 Third Avenue, New York, NY 10158-0012: John Wiley and Sons, Ltd, 2007. (Detection, Estimation and Modulation Theory, Vol IV). ISBN 0-471-09390-4.

SWINDLEHURST, A.; KAILATH, T. Azimuth/elevation direction finding using regular array geometries. *IEEE Transactions on Aerospace and Electronic Systems*, v. 29, n. 1, p. 145–156, 1993.

WAITE, A. D. *Sonar for Practising Engineers*. Chichester: Wiley, 2002. ISBN 0471497509.

MARAGE, J.; MORI, Y. *Sonar and Underwater Acoustics*. [S.l.]: Wiley, 2013. (ISTE). ISBN 9781118600658.

MURMEL, G. F.; APOLINÁRIO, J. A.; CAMPOS, M. L. R. D.; RAMOS, A. L. L. DoA estimation performance of UCAs with reduced number of sensors using phase-mode transformation and small sample support. In: *2022 IEEE 12th Sensor Array and Multichannel Signal Processing Workshop (SAM)*. [S.l.: s.n.], 2022. p. 1–5.

KRIM, H.; VIBERG, M. Two decades of array signal processing research: the parametric approach. *IEEE Signal Processing Magazine*, v. 13, n. 4, p. 67–94, 1996.

HICKMAN, C. E.; NEFF, H. P.; TILLMAN, J. D. The theory of a single-ring circular antenna array. *Transactions of the American Institute of Electrical Engineers, Part I: Communication and Electronics*, v. 80, n. 2, p. 110–115, 1961.

OPPENHEIM, A. V.; SCHAFER, R. W. *Discrete-Time Signal Processing*. 3rd. ed. USA: Prentice Hall Press, 2009. ISBN 0131988425.

DINIZ, P. S.; SILVA, E. A. D.; NETTO, S. L. *Digital Signal Processing: System Analysis and Design*. [S.l.]: Cambridge University Press, 2010.

KRISHNAVENI, V.; KESAVAMURTHY, T.; APARNA, B. Beamforming for direction-of-arrival (DOA) estimation-a survey. In: . [S.l.: s.n.], 2013. v. 61, p. 4–11.

SCHMIDT, R. Multiple emitter location and signal parameter estimation. *IEEE Transactions on Antennas and Propagation*, v. 34, n. 3, p. 276–280, 1986.

ZOLTOWSKI, M.; KAUTZ, G.; SILVERSTEIN, S. Beamspace Root-MUSIC. *IEEE Transactions on Signal Processing*, v. 41, n. 1, p. 344–, 1993.

ROY, R.; KAILATH, T. Esprit-estimation of signal parameters via rotational invariance techniques. *IEEE Transactions on Acoustics, Speech, and Signal Processing*, v. 37, n. 7, p. 984–995, 1989.

BARABELL, A. Improving the resolution performance of eigenstructure-based direction-finding algorithms. In: *ICASSP 83. IEEE International Conference on Acoustics, Speech, and Signal Processing*. [S.l.: s.n.], 1983. v. 8, p. 336–339.

LONGSTAFF, I.; CHOW, P.; DAVIES, D. Directional properties of circular arrays. In: . [S.l.: s.n.], 1967.

AKIYAMA, T.; YAMAOKA, T.; HAMADA, N. 2-D angle estimation using the constrained music with circular array. In: *ISSPA 99. Proceedings of the Fifth International Symposium on Signal Processing and its Applications (IEEE Cat. No.99EX359).* [S.l.: s.n.], 1999. v. 2, p. 877–880 vol.2.

ABRAMOWITZ, M.; STEGUN, I. A. *Handbook of Mathematical Functions.* New York: Dover Publications, 1964. ISBN 0-486-61272-4.

MATHEWS, C.; ZOLTOWSKI, M. Eigenstructure techniques for 2-D angle estimation with uniform circular arrays. *IEEE Transactions on Signal Processing*, v. 42, n. 9, p. 2395–2407, 1994.

WAX, M.; SHEINVALD, J. Direction finding of coherent signals via spatial smoothing for uniform circular arrays. *IEEE Transactions on Antennas and Propagation*, v. 42, n. 5, p. 613–620, 1994.

HONG, W.; TEWFIK, A. On the application of uniform linear array bearing estimation techniques to uniform circular array. In: *Antennas and Propagation Society Symposium 1991 Digest.* [S.l.: s.n.], 1991. p. 372–375 vol.1.

GOOSSENS, R.; ROGIER, H.; WERBROUCK, S. UCA Root-MUSIC with sparse uniform circular arrays. *IEEE Transactions on Signal Processing*, v. 56, n. 8, p. 4095–4099, 2008.

BABU, K. A fast algorithm for adaptive estimation of Root-MUSIC polynomial coefficients. In: *ICASSP 91. IEEE International Conference on Acoustics, Speech, and Signal Processing.* [S.l.: s.n.], 1991. p. 2229–2232 vol.3.

RUDGE, A. W. *The Handbook of Antenna Design.* London: P. Peregrinus on behalf of the Institution of Electrical Engineers, 1982. ISBN 9780906048825.

LI, S.; CHEN, H. A novel method of DOA estimation on sparse uniform circular array. In: *CIE International Conference on Radar (RADAR).* [S.l.: s.n.], 2016. p. 1–4.

HACKER, P.; YANG, B. Single snapshot DOA estimation. *Advances in Radio Science*, Copernicus Publications, v. 8, p. 251–256, 2010. ISSN 1684-9965.

REDDY, K. M.; REDDY, V. Analysis of spatial smoothing with uniform circular arrays. *IEEE Transactions on Signal Processing*, v. 47, n. 6, p. 1726–1730, 1999.

LI, Q.; SU, T.; WU, K. Accurate DOA estimation for large-scale uniform circular array using a single snapshot. *IEEE Communications Letters*, v. 23, n. 2, p. 302–305, 2019.

SHAGHAGHI, M.; VOROBYOV, S. A. Subspace leakage analysis and improved DOA estimation with small sample size. *IEEE Transactions on Signal Processing*, v. 63, n. 12, p. 3251–3265, 2015.

XINGXING, L.; DANGWEI, W.; MA, X.; CHANG, Z. Robust adaptive beamforming algorithm in the situation of small sample size. In: *CIE International Conference on Radar (RADAR).* [S.l.: s.n.], 2016. p. 1–4.

WEN, F.; WANG, Z. An efficient two-step direction finding method in sample-starved environments. In: *20th International Conference on Information Fusion (Fusion)*. [S.l.: s.n.], 2017. p. 1–5.

TREFETHEN, L.; BAU, D. *Numerical Linear Algebra*. 3600 Market Street, Floor 6, Philadelphia, PA 19104: Society for Industrial and Applied Mathematics (SIAM), 1997. ISBN 9780898719574.

JIANG, G.; MAO, X.; LIU, Y. Direction-of-arrival estimation for uniform circular arrays under small sample size. *Journal of Systems Engineering and Electronics*, v. 27, n. 6, p. 1142–1150, 2016.

XIAOFEI, Z.; WEN, L.; YING, S.; RUINA, Z.; DAZHUAN, X. A novel DOA estimation algorithm based on eigen space. In: *International Symposium on Microwave, Antenna, Propagation and EMC Technologies for Wireless Communications*. [S.l.: s.n.], 2007. p. 551–554.

DEGEN, C. On single snapshot direction-of-arrival estimation. In: *IEEE International Conference on Wireless for Space and Extreme Environments (WiSEE)*. [S.l.: s.n.], 2017. p. 92–97.

MARPLE, S. *Digital Spectral Analysis: Second Edition*. [S.l.]: Dover Publications, 2019. (Dover Books on Electrical Engineering). ISBN 9780486780528.

LEON-GARCIA, A. *Probability, Statistics, and Random Processes For Electrical Engineering*. [S.l.]: Pearson Education, 2011. ISBN 9780133002577.

YADRENKO, M. I. *Spectral Theory of Random Fields*. New York: Optimization Software, INC.,Publications Division, 1983. ISBN 0387908234.

APPENDIX A – ALGORITHMS

Algorithm 1 Phase Modes-based Beamspace transform

$M \leftarrow$ Number of sensors
$N \leftarrow$ Highest-order Phase Mode
$n \leftarrow 2N + 1$
$\lambda \leftarrow$ Wavelength
$K \leftarrow 2\pi/\lambda$
$R \leftarrow$ Radius (in wavelengths)
$\phi = 0 : 0.1 : 360$ $\triangleright$ 2-D DoA grid
$\theta = 0 : 0.1 : 90$
$D \leftarrow$ Number of sources $\triangleright$ Previously established
$size \leftarrow$ Number os snapshots
$w \leftarrow \exp\left(j\frac{2\pi}{M}\right)$
for $i = 1 : n$ **do**
    for $j = 1 : M$ **do**
        $\mathbf{F}(i,j) = \frac{1}{M}w^{(j-1)(-n-1+i)}$
    end for
end for
$\mathbf{W}^{\mathrm{H}} \leftarrow \mathbf{F}$ $\triangleright$ Beamforming matrix
for $k = 1 : size$ **do**
    $\mathbf{R}_x = \mathbf{R}_x + \mathbf{x}(k)\mathbf{x}(k)^{\mathrm{H}}$
    $\bar{\mathbf{x}}(k) = \mathbf{W}^{\mathrm{H}}\mathbf{x}(k)$
    $\mathbf{R}_{\bar{x}} = \mathbf{R}_{\bar{x}} + \bar{\mathbf{x}}(k)\bar{\mathbf{x}}(k)^{\mathrm{H}}$
end for
$\mathbf{R}_x = \mathbf{R}_x/size$ $\triangleright$ Element-space sample covariance matrix
$\mathbf{R}_{\bar{x}} = \mathbf{R}_{\bar{x}}/size$ $\triangleright$ Beamspace sample covariance matrix

---

Algorithm 2 Element-space and Beamspace Spectral MUSIC

$\mathbf{R}_x = \mathbf{E}\mathbf{\Lambda}\mathbf{E}^{\mathrm{H}}$ ⊳ EVD Element-space sample covariance matrix
$\bar{\mathbf{R}}_x = \bar{\mathbf{E}}\bar{\mathbf{\Lambda}}\bar{\mathbf{E}}^{\mathrm{H}}$ ⊳ EVD Beamspace sample covariance matrix
$\mathbf{E}_s = \mathbf{E}(:, 1:D)$
$\mathbf{E}_n = \mathbf{E}(:, D+1:M)$
$\bar{\mathbf{E}}_s = \bar{\mathbf{E}}(:, 1:D)$
$\bar{\mathbf{E}}_n = \bar{\mathbf{E}}(:, D+1:n)$
for $\phi = 0:360°$ **do**
    for $\theta = 0:90°$ **do**
        for $m = 1:M$ **do**
            $\mathbf{a}(m,1) = \exp[(j(KR)\sin(\theta)\cos((2\pi(m-1)/M) - \phi)]$
        end for
        $\mathbf{P}_{MUSIC}(\theta, \phi) = 1/(\mathbf{a}^{\mathrm{H}}\mathbf{E}_n\mathbf{E}_n^{\mathrm{H}}\mathbf{a})$ ⊳ 2-D grid search
    end for
end for
$\mathbf{P}_{MUSIC} = \mathbf{P}_{MUSIC}/|\mathbf{P}_{MUSIC}|$ ⊳ Normalization
for $\phi = 0:360°$ **do**
    for $\theta = 0:90°$ **do**
        for $q = 1:n$ **do**
            $\bar{\mathbf{a}}(q,1) = \exp(-N-1+q)J_{(-N-1+q)}[KR\sin(\theta)]\exp[j(-N-1+q)(\phi)]$
        end for
        $\bar{\mathbf{P}}_{MUSIC}\theta, \phi) = 1/(\bar{\mathbf{a}}^{\mathrm{H}}\bar{\mathbf{E}}_n\bar{\mathbf{E}}_n^{\mathrm{H}}\bar{\mathbf{a}})$ ⊳ 2-D grid search
    end for
end for
$\bar{\mathbf{P}}_{MUSIC} = \bar{\mathbf{P}}_{MUSIC}/|\bar{\mathbf{P}}_{MUSIC}|$ ⊳ Normalization

---

Algorithm 3 Beamspace Root-MUSIC

---

for $q = 1 : n$ **do**
  $\mathbf{d}(q,1) = \exp(-N - 1 + q)J_{(-N-1+q)}(KR\sin(\theta))$
end for
$\mathbf{D} = \mathrm{diag}(\mathbf{d});$
$\mathbf{RTS} = \mathbf{D}^{\mathrm{H}}\bar{\mathbf{E}}_n\bar{\mathbf{E}}_n^{\mathrm{H}}\mathbf{D}$
for $i = 1 : n - 1$ **do**
  $\mathbf{coef}_{sup}(i) = \sum(\mathrm{diag}(\mathbf{RTS}, i))$
end for
for $i = 1 : n - 1$ **do**
  $\mathbf{coef}_{inf}(i) = \sum(\mathrm{diag}(\mathbf{RTS}, -i))$
end for
$\mathbf{coef}_{Total} = [\mathrm{fliplr}(\mathbf{coef}_{inf}) \vdots \sum(\mathrm{diag}(\mathbf{RTS})) \vdots (\mathbf{coef}_{sup})]$
$\mathbf{coef}_{Total} = \mathrm{fliplr}(\mathbf{coef}_{Total})$ $\triangleright$ Coefficients of the Root-MUSIC polynomial
$\mathbf{root}_{MUSIC} = roots(\mathbf{coef}_{Total})$
for $i = 1 : n - 1$ **do** $\triangleright$ Polynomial Rooting Algorithm
  $doa_\phi(i) = \mathrm{angle}(root_{MUSIC}(i))$ $\triangleright$ Angle of the root
  $mag(i) = |root_{MUSIC}(i)|$ $\triangleright$ Magnitude of the root
end for
sort roots by magnitude

$\mathbf{ROOTS} = [\mathbf{mag} \vdots \mathbf{doa}_\phi]$
$doa\phi_{SoI} = \mathrm{angle}(\text{First root closest to the unit circle})$ $\triangleright$ Azimuth DoA of SoI
$doa\phi_{Int} = \mathrm{angle}(\text{Second root closest to the unit circle})$ $\triangleright$ Azimuth DoA of Interferer

---

Algorithm 4 Two-step 2-D DoA with Root-MUSIC and Spectral MUSIC

$\theta \leftarrow 90\,°$ $\triangleright$ Initial presumed zenith angle $\theta = 90°$
Execute Beamspace Root-MUSIC Algorithm and obtain $doa\phi_{SoI}, doa\phi_{Int}$

Zenith DoA obtained via Spectral MUSIC
for $\theta = 0 : 90°$ **do**
  for $m = 1 : M$ **do**
    $\mathbf{a}(m,1) = \exp[(j(KR)\sin(\theta)$
    $\cos((2\pi(m-1)/M) - doa\phi)]$
  end for
  $\mathbf{P}_{MUSIC}(\theta) = 1/(\mathbf{a}^{\mathrm{H}}\mathbf{E}_n\mathbf{E}_n^{\mathrm{H}}\mathbf{a})$ $\triangleright$ 1-D grid search in the direction of the Azimuth DoA
end for
$\mathbf{P}_{MUSIC} = \mathbf{P}_{MUSIC}/|\mathbf{P}_{MUSIC}|$ $\triangleright$ Normalization

$\theta_{SoI} = \mathrm{argmax}_\theta(\mathbf{P}_{MUSIC}(\phi_{SoI}))$
$\theta_{Int} = \mathrm{argmax}_\theta(\mathbf{P}_{MUSIC}(\phi_{Int}))$

Algorithm 5 Leakage Minimization: cross-correlation estimation and revision of Beamspace sample covariance matrix

---

$\theta \leftarrow 90°$ $\triangleright$ For the first step, presume zenith angle θ

$\mu \leftarrow 0.8$ $\triangleright$ $0 < \mu < 1$

Obtain biased initial DoA estimations ϕ_{SoI}, ϕ_{Int} from Beamspace Root-MUSIC algorithm

for m=1:M **do**

     $\mathbf{a}_{ini1}(m) = \exp(j(KR)\sin(\theta)\cos(-(2\pi(m-1)/M) + (\phi_{SoI})))$

     $\mathbf{a}_{ini2}(m) = \exp(j(KR)\sin(\theta)\cos(-(2\pi(m-1)/M) + (\phi_{Int})))$

end for

$\mathbf{A}_{ini} = [\mathbf{a}_{ini1} \;\; \mathbf{a}_{ini2}]$ $\triangleright$ Beamspace array manifold matrix of initial DoAs for SoI and Interferer sources

$\mathbf{P} = \mathbf{W}^{\mathrm{H}}\mathbf{A}_{ini}(\mathbf{A}_{ini}^{\mathrm{H}}\mathbf{W}\mathbf{W}^{\mathrm{H}}\mathbf{A}_{ini})^{-1}(\mathbf{A}_{ini}^{\mathrm{H}}\mathbf{W})$

$\mathbf{T} = \mathbf{P}\mathbf{R}_{\bar{x}}(\mathbf{I}_{(n)} - \mathbf{P})$ $\triangleright$ Residual cross-correlation

$\mathbf{R}_{\bar{x}}up = \mathbf{R}_{\bar{x}} - \mu(\mathbf{T} + \mathbf{T}^{\mathrm{H}})$ $\triangleright$ Revised Beamspace Sample Covariance Matrix

Utilize $\mathbf{R}_{\bar{x}}up$ in Beampace Root-MUSIC for revised azimuth DoA and in Spectral MUSIC for zenith DoA

APPENDIX B – BEAMSPACE TRANSFORM OF BACKGROUND NOISE

Chapter 3 addressed the beamspace transform based on phase modes excitation of the UCA array manifold. In Eq. (3.32) we have the beamspace noise vector $\bar{\mathbf{n}}(k)$ Now, we show the effects of applying phase mode transformation to a noise process $\mathbf{n}(k)$, particularly to an isotropic and homogeneous one, in order to obtain $\bar{\mathbf{n}}(k)$. The noise-only process is akin to a random field HONG; TEWFIK, 1991. A random field $\epsilon(\mathbf{p}_1 \ldots \mathbf{p}_m)$ is defined by a random function $f(\mathbf{p})$ in $\mathbb{R}^m$. Considering a UCA immersed in background noise only (akin to an Euclidean-dimensioned random field), the sensors sample this random field at the points $\mathbf{p}_m = R \left[\cos((m-1)\frac{2\pi}{M}) \quad \sin((m-1)\frac{2\pi}{M}) \quad 0 \right]^{\mathrm{T}}$. The covariance value of the noise-only output of the sensors is given by $R_x(\mathbf{p}_i, \mathbf{p}_j) = \mathrm{E}\left[x(\mathbf{p}_i)x^*(\mathbf{p}_j)\right]$, and the corresponding covariance matrix $\mathbf{R}_x$.

A random process in classified as stationary LEON-GARCIA, 2011 (in our case, spatially stationary) when the mean or mathematical expectation $m_x(\mathbf{p}_i) = \mathrm{E}\left[x(\mathbf{p}_i)\right]$ and the variance $\mathrm{VAR}\left[x(\mathbf{p}_i)\right] = \mathrm{E}\left[(x(\mathbf{p}_i) - m_x(\mathbf{p}_i))^2\right]$ are constants (spatially invariant), and the autocovariance $R_x(\mathbf{p}_i, \mathbf{p}_j)$ is a function of $\mathbf{p}_i - \mathbf{p}_j$ only. Whide-sense stationary is a more encompassing classification where the criteria of constant mean and autocovariance as function of $\mathbf{p}_i - \mathbf{p}_j$ hold, where i and j are indexes of two sensors and $\mathbf{p}_i$ and $\mathbf{p}_j$ are the position vectors of these sensors.

In general, the noise field will not be spatially stationary (stationary in variable m, spatial samples), consequently, the covariance will not be a function of $\mathbf{p}_i - \mathbf{p}_j$. However, if the random process is isotropic YADRENKO, 1983, it consequently will be spatially stationary. Isotropy can be defined both for stationary processes if it is also true that $R_x(\mathbf{p}_i, \mathbf{p}_j)$ is a function of the Euclidean distance $\|\mathbf{p}_i - \mathbf{p}_j\|$ only, then we say that ϵ is also isotropic. For the particular special case of a spatially white and homogeneous random field, the corresponding covariance is $R_x(\mathbf{p}_i, \mathbf{p}_j) = \sigma^2 \delta(i - j)$.

Regarding the phase modes-based beamforming, we define $R_{\bar{x}}(t, u)$ the beamspace covariance for the transformed noise-only process and $\mathbf{R}_{\bar{x}}$ as the transformed covariance matrix, where t and u are indexes of two phase-modes. It is possible to relate the covariance matrices of noise processes in element-space and beamspace according to the similarity transformation of Eq. (3.33). Moreover, for the assumed isotropic background noise process, the covariance matrix in element-space $\mathbf{R}_x$ is circulant, and consequently, diagonalized by the $M \times M$ DFT matrix $\mathbf{W}$, in the form

$$W_{(o,p)} = \frac{1}{\sqrt{M}} \exp\left(\mathrm{j}\frac{2\pi op}{M}\right). \tag{B.1}$$

In this manner, $\mathbf{R}_{\bar{x}}$ is a diagonal matrix, and we can conclude that an isotropic background process in element-space is mapped into a possibly nonstationary white noise process. Specifically, and according to the Perseval's Theorem, a spatially white background noise in element space is mapped in a stationary noise processes with variance σ^2/M and with covariance matrix $\mathbf{R}_{\bar{x}} = \frac{\sigma^2}{M}\mathbf{I}_M$, $\mathbf{I}_M$ being the $M \times M$ identity matrix.

For this formulation of phase-modes transformation for background noise, $\mathbf{W}$ is a square matrix (due to the similarity transformation in Eq. (3.33)) that represents the particular transformation of an element-space odd M sensor UCA into a beamspace $(2N + 1 = M)$-sensor array.